CASE FILE COPY

EFFECT OF NOZZLE LATERAL SPACING ON AFTERBODY DRAG AND PERFORMANCE OF TWIN-JET AFTERBODY MODELS WITH CONVERGENT-DIVERGENT NOZZLES AT MACH NUMBERS UP TO 2.2

by Odis C. Pendergraft, Jr., and James W. Schmeer

Langley Research Center
Hampton, Va. 23365

1. Report No. NASA TM X-2601	2. Government Accession No.	3. Recipient's Catalog No.
4. Title and Subtitle EFFECT OF NOZZLE LATERAL SPACING ON AFTERBODY DRAG AND PERFORMANCE OF TWIN-JET AFTERBODY MODELS WITH CONVERGENT-DIVERGENT NOZZLES AT MACH NUMBERS UP TO 2.2		5. Report Date October 1972
		6. Performing Organization Code
7. Author(s) Odis C. Pendergraft, Jr., and James W. Schmeer		8. Performing Organization Report No. L-8338
9. Performing Organization Name and Address NASA Langley Research Center Hampton, Va. 23365		10. Work Unit No. 501-24-06-01
		11. Contract or Grant No.
12. Sponsoring Agency Name and Address National Aeronautics and Space Administration Washington, D.C. 20546		13. Type of Report and Period Covered Technical Memorandum
		14. Sponsoring Agency Code

15. Supplementary Notes

16. Abstract

   Twin-jet afterbody models were investigated by using two balances to measure the thrust-minus-total drag and the afterbody drag, separately, at static conditions and at Mach numbers up to 2.2 for an angle of attack of 0°. Hinged-flap convergent-divergent nozzles were tested at subsonic-cruise- and maximum-afterburning-power settings with a high-pressure air system used to provide jet-total-pressure ratios up to 20. Two nozzle lateral spacings were studied, using afterbodies with similar interfairing shapes but with different longitudinal cross-sectional area distributions. Alternate, blunter, interfairings with different shapes for the two spacings, which produced afterbodies having identical cross-sectional area progressions corresponding to an axisymmetric minimum wave-drag configuration, were also tested. The results indicate that the wide-spaced configurations improved the flow field around the nozzles, thereby reducing drag on the cruise nozzles; however, the increased surface and projected cross-sectional areas caused an increase in afterbody drag. Except for a slight advantage with cruise nozzles at subsonic speeds, the wide-spaced configurations had the higher total drag at all other test conditions.

17. Key Words (Suggested by Author(s)) Jet effects Twin-jet afterbody models Afterbody and nozzle drag	18. Distribution Statement Unclassified — Unlimited

19. Security Classif. (of this report) Unclassified	20. Security Classif. (of this page) Unclassified	21. No. of Pages 123	22. Price* $3.00

EFFECT OF NOZZLE LATERAL SPACING ON AFTERBODY DRAG

AND PERFORMANCE OF TWIN-JET AFTERBODY MODELS

WITH CONVERGENT-DIVERGENT NOZZLES

AT MACH NUMBERS UP TO 2.2

By Odis C. Pendergraft, Jr., and James W. Schmeer
Langley Research Center

SUMMARY

An investigation has been conducted to determine the effect of nozzle lateral spacing on the drag and performance of twin-engine-afterbody configurations with hinged-flap convergent-divergent nozzles at static conditions and at Mach numbers ranging from 0.6 to 2.2. Two lateral spacings of the nozzle exits were studied, with similar interfairing shapes and fineness ratios maintained as the spacing was varied. An alternate interfairing shape was also studied that had different interfairing shapes for the close- and wide-spaced afterbodies. Both afterbodies then had the same longitudinal cross-sectional area distribution. These interfairings were blunter than the basic shapes and yielded an area progression corresponding to an axisymmetric minimum wave-drag configuration. Two nozzle configurations were used. The dry-power configuration had a conical boattail nozzle and corresponded to minimum throat area. The maximum-augmented-power configuration had a cylindrical boattail and corresponded to maximum throat area. The jet-total-pressure ratio was varied from 1.0 (jet off) to approximately 20, depending on Mach number.

The results of the investigation indicate that spacing the engines apart produced cleaner flow around the nozzles, with a corresponding decrease in nozzle drag; but, the resultant increase in wetted afterbody surface area, and greater projected cross-sectional area of the interfairing, produced drag increases on the afterbody that nearly offset the better nozzle performance at subsonic Mach numbers and produced a net decrease in performance at supersonic Mach numbers. The alternate-interfairing configurations produced better performance only for the close-spaced afterbody at subsonic Mach numbers.

INTRODUCTION

Past experience gained in research by both NASA and industry on the performance of fuselage-installed, twin-engine nozzles has shown that this type of afterbody-nozzle

arrangement can be quite sensitive to mutual nozzle-airframe interactions (ref. 1). This knowledge has stimulated further work on generalized twin-nozzle-afterbody configurations in an effort to provide information useful in the design of airplane-afterbody-nozzle configurations with good installed performance.

As part of a continuing program on engine-nozzle—aircraft-afterbody integration, the Langley Research Center is evaluating the performance of various twin-jet nozzles installed near the rear of model fuselages. Reference 2, wherein the effects of axial location of jet exits along the body were examined, reports the results of the initial investigation utilizing the air-powered, strut-supported model on which the twin-jet configurations are mounted. The model is designed to make separate measurements of the combined exhaust thrust minus drag and the external afterbody drag. Subsequent investigations have studied the effects of afterbody shape and type, lateral spacing of the nozzle exits, and different fairings between and outboard of the nozzles (refs. 3 to 5).

Reference 4 presents the results of an investigation on the effects of nozzle lateral spacing within a 25.4-cm-wide envelope for hinged-flap convergent nozzles; whereas the present investigation using the same width constraint (permitting a maximum-nozzle-spacing ratio of 1.48) shows the effect of lateral spacing for exposed-hinged-flap convergent-divergent nozzles with close- and wide-spaced afterbodies having similar interfairing shapes. Configurations with alternate blunter interfairings having different shapes were also investigated; these alternate interfairings made the cross-sectional area distributions and fineness ratios of the close- and wide-spaced afterbodies identical.

The investigation was conducted in the Langley 16-foot transonic tunnel at static conditions and at Mach numbers from 0.6 to 1.3 with nozzle throat areas corresponding to dry power (minimum throat area and conical 18.3° boattails) and maximum augmented power (maximum throat area and cylindrical boattails) and in the Langley 4- by 4-foot supersonic pressure tunnel at Mach number 2.2 with only the maximum-augmented-power nozzles. Jet-total-pressure ratio was varied from 1.0 (jet off) to approximately 8 in the transonic facility and to approximately 20 in the supersonic tunnel. All configurations were tested at zero degrees angle of attack.

SYMBOLS

Aerodynamic coefficients are based on $q_\infty A_{max}$.

A   cross-sectional area, m^2

A_e exit area of one nozzle (model station 142.39 for cruise nozzle; model station 142.62 for afterburning nozzle), m^2

A_{eng} maximum cross-sectional area of one nozzle, m^2

A_{max} maximum cross-sectional area of afterbody, m^2

A_s open area of one nozzle clearance hole in afterbody at model station 134.62, m^2

A_{seal} cross-sectional area enclosed by seal strip, m^2

A_t throat area of one nozzle, m^2

A_β projected cross-sectional area of one nozzle boattail, m^2

$C_{A,a}$ axial-force (drag) coefficient of afterbody including force on afterbody-nozzle annuli, positive downstream

$C_{A,\beta}$ axial-force coefficient of both nozzle boattails integrated from boattail pressure measurements, positive downstream

$C_{Af,a}$ afterbody skin-friction axial-force coefficient, positive downstream

$C_{Af,n}$ skin-friction axial-force coefficient of both nozzles, positive downstream

$C_{D,wave}$ supersonic wave-drag coefficient, positive downstream

C_p local-pressure coefficient, $\dfrac{p_l - p_\infty}{q_\infty}$

$C_{p,base}$ nozzle-base pressure coefficient

$C_{p,if}$ afterbody-interfairing static-pressure coefficient

$C_{p,\beta}$ nozzle-boattail pressure coefficient, $\dfrac{p_\beta - p_\infty}{q_\infty}$

$C_{T,i}$ aerodynamic ideal-thrust coefficient, $F_i / q_\infty A_{max}$

d_{eng} nozzle maximum diameter (at model station 134.62), m

d_s internal diameter of afterbody-nozzle openings, m

d_t nozzle-throat diameter, m

3

$F_{A,a}$ axial force on afterbody including force on afterbody-nozzle clearance annuli, N

$F_{A,\beta}$ axial force on both nozzle boattails, integrated boattail pressure measurements (does not include base force), N

$F_{A,base}$ axial force on both nozzle bases, integrated base pressure measurements, N

$F_{A,f}$ skin-friction axial force of both nozzles, positive downstream, N

$F_{A,n}$ external axial force (drag) on both nozzles, N

$F_{A,t}$ total axial force (drag) of afterbody plus nozzles, N

$F_{bal,a}$ force measured by afterbody drag balance, positive downstream, N

$F_{bal,j}$ force measured by thrust-minus-drag balance, positive upstream, N

F_i ideal gross thrust for isentropic expansion of measured total mass-flow rate

to free-stream static pressure, $\dot{m}_j \sqrt{\dfrac{2\gamma}{\gamma - 1} RT_{t,j} \left[1 - \left(\dfrac{p_\infty}{p_{t,j}} \right)^{\frac{\gamma-1}{\gamma}} \right]}$, N

F_j gross thrust of both nozzles, positive upstream, N

l model length from nose to the end of the afterburning nozzles, 1.4262 m

L   nozzle length from throat to exit, m

M   free-stream Mach number

$\dot{m}_j$ measured total mass-flow rate, kg/s

p_a ambient pressure, N/m^2

p_{an} static pressure in afterbody-nozzle clearance annuli (fig. 3), N/m^2

p_β static pressure on nozzle boattail (fig. 3), N/m^2

p_{base} static pressure on nozzle base (fig. 3), N/m^2

4

p_{es} static pressure near metric gap, external to seal (fig. 3), N/m^2

p_i internal static pressure of afterbody (fig. 3), N/m^2

p_l local static pressure, N/m^2

$p_{t,j}$ jet total pressure (fig. 3), N/m^2

p_∞ free-stream or ambient static pressure, N/m^2

q_∞ free-stream dynamic pressure, N/m^2

R gas constant ($\gamma = 1.4$), 287.3 N-m/kg-K

R_e Reynolds number based on model length

r radius, m

S lateral distance between afterbody radii center lines (fig. 4), m

S_{eng} lateral distance between nozzle center lines (fig. 4), m

S_w total wetted area of afterbody plus nozzles, m^2

$T_{t,j}$ jet stagnation temperature (fig. 3), K

x axial distance from model nose, m

z_1 height of basic-interfairing surface above afterbody center line (fig. 4), m

z_2 height of alternate-interfairing surface above afterbody center line (fig. 4), m

β boattail angle, deg

γ ratio of specific heats

θ meridian angle about nozzle axis, deg

A bar over a symbol denotes an average value.

APPARATUS AND PROCEDURE

Wind Tunnels and Tests

Tests were conducted in the Langley 16-foot transonic tunnel and the Langley 4- by 4-foot supersonic pressure tunnel. Both are single-return, continuous-flow tunnels.

The 16-foot transonic tunnel operates at atmospheric pressure and has an octagonal test section measuring 4.8 meters diametrically to midflat center line. With the aid of a compressor system drawing air out through slots in the test section for $M > 1.05$ the 16-foot tunnel has a continuously variable speed range from $M = 0.20$ to 1.30.

The Langley 4- by 4-foot supersonic pressure tunnel has a stagnation-pressure range of 27.58 kN/m^2 to 206.84 kN/m^2 and a stagnation temperature range of 310.9 K to 322.2 K. By mechanically deflecting the tunnel floor and ceiling between fixed side walls 1.37 m apart, to form a divergent nozzle, the Mach number can be varied from 1.25 to 2.20.

Data on the twin-jet afterbody models were taken at static conditions and at Mach numbers from 0.60 to 1.30 in the 16-foot tunnel, where the average Reynolds number per meter ranged from 10.3×10^6 at $M = 0.60$ to 14.0×10^6 at $M = 1.30$. In the 4- by 4-foot supersonic pressure tunnel, data were recorded at $M = 2.20$ only. The stagnation pressure was approximately 121 kN/m^2, the stagnation temperature was 316 K, and the Reynolds number per meter was 11.8×10^6. The model angle of attack was zero degrees in both facilities, and the jet total-to-free-stream static-pressure ratio was varied from approximately 1 (at jet-off conditions) to 20, depending on Mach number and model-nozzle configuration. Configurations with cruise-power nozzles (minimum throat area) were investigated at Mach numbers from 0.60 to 0.95 only, and those with augmented-power nozzles (maximum throat area) were investigated over the entire speed range.

Model and Support System

A sketch of the strut-supported model with the twin-jet engine simulator used in the investigation is presented in figure 1, and a photograph of a typical model configuration installed in the 16-foot transonic tunnel is shown in figure 2.

The afterbody shell of the model began 83.82 cm from the nose and was attached to a drag balance which, in turn, was attached in tandem to a thrust-minus-drag balance as shown in figure 3. An annular clearance gap between the afterbody and nozzles was required to prevent fouling of the afterbody drag balance. A teflon strip inserted into grooves machined into the forward edge of the afterbody shell and the rear edge of the forebody shell (see fig. 3) was used as a seal to prevent internal flow in the model. The teflon strip, because of its low coefficient of friction, minimized restraint between the

6

two balances. A 0.25-cm-wide transition strip of No. 100 carborundum grit was fixed 2.54 cm from the nose of the model.

High pressure air was used to simulate the exhaust of a twin-jet configuration. Compressed air was supplied to the model through pipes in the strut and passed through eight orifice nozzles into a low-pressure plenum chamber (see fig. 1). The orifice nozzles were located perpendicular to the longitudinal axis of the model to eliminate transfer of axial momentum. From the plenum chamber the air was passed through the tailpipe-nozzle system.

Sketches giving the dimensions of the four afterbody configurations and orifice locations used in this investigation are presented in figure 4. Two lateral spacings between engine-nozzle center lines were selected. The close-spaced configuration shown in figure 4(a) was determined by the minimum practical clearance between parallel tailpipes; in terms of a nondimensional spacing ratio based on maximum engine-nozzle diameter, this spacing ratio was 1.14. The wide-spaced configuration shown in figure 4(b) represented the maximum available spread between the nozzles limited to the confines of the maximum width of an existing forebody model (spacing ratio 1.48). Figure 5(a) is a photograph of the various afterbody and nozzle parts, and figures 5(b) and 5(c) are photographs of the regions around the interfairing-nacelle juncture of the close- and wide-spaced afterbodies, respectively, showing the orifice locations relative to the interfairing contours.

Sketches giving the dimensions and orifice locations of the two nozzle configurations used in this investigation are presented in figure 6. The afterburning nozzles, shown in figure 6(a), were designed to represent a variable flap convergent-divergent nozzle with a cylindrical boattail and an ejector length of about 1 throat diameter. The cruise nozzles, shown in figure 6(b), represent the same nozzle design but with the throat closed down to dry-power cruise position and with the exit closed down so there is just enough divergence to maintain the throat in the proper position (in this case, 1.79 diameters upstream of the nozzle exit). Photographs of the two nozzle configurations installed in the basic, close-spaced afterbody are presented in figure 7.

Afterbody-nozzle geometric ratios are given in table I for all configurations, with spacing ratios in terms of maximum nozzle diameter and nozzle throat diameter. A general description of each configuration is given in table II. The basic close-spaced and wide-spaced afterbody geometries were represented by configurations 1 and 5, respectively, with cruise-power nozzles and by configurations 2 and 6, respectively, with afterburning-power nozzles. All four basic configurations had similar interfairing shapes but different cross-sectional area distributions. The alternate close-spaced and wide-spaced afterbody geometries were represented by configurations 3 and 7, respectively, with cruise-power nozzles and by configurations 4 and 8, respectively, with afterburning-power nozzles. With the addition of add-on pieces over the basic afterbody

interfairings, all four alternate configurations had blunter and different interfairing shapes, but the same cross-sectional area distributions. The area distributions of afterbody configurations 3 and 7 (shown in fig. 8) between $x/l = 0.60$ and $x/l = 0.94$ were calculated by a computer program for axisymmetric bodies adapted from reference 6. They are representative of a minimum wave-drag body with nozzles in the cruise position at a Mach number of 1.000001 with the restraint of a given forebody area distribution, afterbody length, base area, and an infinite cylindrical exhaust plume equal to the base area in cross section. Since the minimum wave-drag area distribution was computed for an axisymmetric shape, this may not represent the minimum wave-drag shape when applied to twin-engine-nacelle configurations such as the ones used in this investigation.

Instrumentation

External static-pressure orifices were located on the afterbodies as indicated in figure 4 and on the nozzles as indicated in figure 6. Pressure distributions were obtained, on both afterbodies, along axial rows on the top and bottom model center lines, along the top of one nacelle, and along the outside of the same nacelle. Pressures were also measured radially near the end of the interfairing on the inside of one nacelle. (See figs. 5(b) and 5(c).) The pressure orifices on the afterbodies were intended to indicate the flow characteristics over the afterbody model and to aid in interpreting the force-measurement results; but the distribution of orifices was not complete enough to determine afterbody pressure drag. Pressures measured on the nozzles were used to determine nozzle pressure drag by an area-weighted numerical summation. Internal pressures were measured in the afterbody cavity at six locations and around each nozzle annulus at four locations manifolded together to get one average value for each nacelle. Eight external static pressures were measured at orifices located on both sides of the seal gap between the forebody and afterbody (see fig. 3). These pressure measurements were used for axial-force corrections. The total pressure and stagnation temperature of the jet flow were measured in each tailpipe at locations indicated in figure 1.

Forces and moments on the parts of the model under consideration (see fig. 3) were measured by two strain-gage balances. A five-component main balance was used to measure thrust minus afterbody and nozzle drag. Forces and moments on the afterbody shell were measured with a tandem-mounted two-component auxiliary balance in the Langley 16-foot transonic tunnel and, similarly, with a six-component balance in the 4- by 4-foot supersonic pressure tunnel. An electronic turbine flowmeter was used to measure the air-mass-flow rate to the nozzles.

Data obtained in the Langley 16-foot transonic tunnel were recorded simultaneously on magnetic tape and were reduced to coefficient form by use of a computer. Approximately five frames of data were taken over a period of 1 second for each data point and the average value was used for computations. Data obtained in the Langley 4- by 4-foot

8

supersonic pressure tunnel were transmitted to self-balancing potentiometers, digitized, and punched into computer cards. Also, in the 4- by 4-foot supersonic tunnel an electrically actuated scanning valve was used for measuring and recording the internal and external afterbody pressures.

Data Reduction

The recorded data were used to compute standard force and pressure coefficients. The external-seal and internal pressure forces on the afterbodies were obtained by multiplying the difference between the average pressure (external seal, internal cavity, or annuli) and free-stream static pressure by the affected projected area normal to the model axis.

The gross thrust minus the afterbody and nozzle axial force was obtained directly by the thrust-minus-drag balance (see fig. 3). This performance term was computed as follows:

$$F_j - F_{A,t} = F_{bal,j} + \left(\bar{p}_{es} - p_\infty\right)\left(A_{max} - A_{seal}\right) + \left(\bar{p}_i - p_\infty\right)\left(A_{seal} - 2A_s\right)$$

$$+ 2\left(\bar{p}_i - p_\infty\right)A_{eng} + 2\left(\bar{p}_{an} - p_\infty\right)\left(A_s - A_{eng}\right) \tag{1}$$

The forces sensed by the balance and included in the term $F_{bal,j}$ are nozzle thrust, afterbody external and internal axial forces transferred to the thrust-minus-drag balance through the tandem-mounted drag balance, and internal and external axial forces on the nozzle system.

Afterbody axial force was obtained directly from the tandem-mounted drag balance (see fig. 3). Included in the afterbody-axial-force term $F_{A,a}$ is the force acting on the physical-afterbody-base area, and a force not felt by the drag balance on the area of the annulus between the inside of the afterbody and the nozzle (see fig. 3). Since the teflon sealing strip did not give a perfect seal and there was a chance internal flow might create slightly lower static pressures around the restricted annuli passages, separate measurements were made at these locations. During the test runs it was determined that the internal cavity and annuli static pressures agreed closely $\left(p_i \approx p_{an}\right)$, but separate pressure measurements were still used throughout the investigation to calculate the two forces. The afterbody axial force was computed from the following equation:

$$F_{A,a} = F_{bal,a} - \left(\bar{p}_{es} - p_\infty\right)\left(A_{max} - A_{seal}\right) - \left(\bar{p}_i - p_\infty\right)\left(A_{seal} - 2A_s\right)$$

$$- 2\left(\bar{p}_{an} - p_\infty\right)\left(A_s - A_{eng}\right) \tag{2}$$

The internal-pressure correction terms used in the force equations can be large, as was reported in reference 2. The magnitude of this correction can be equal to the drag-balance reading.

The gross thrust minus nozzle axial force was obtained by adding the afterbody axial force, from equation (2), to the gross thrust minus total afterbody and nozzle drag from equation (1) in the following manner:

$$F_j - F_{A,n} = \left(F_j - F_{A,t} \right) + F_{A,a} \tag{3}$$

The external pressure force on the nozzle boattails was obtained by a numerical summation of the local nozzle static pressure minus free-stream static pressure multiplied by a projected cross-sectional area assigned to each orifice as follows:

$$F_{A,\beta} = \sum_{i=1}^{n} 2\left(p_{\beta,i} - p_{\infty} \right) A_{\beta,i} \tag{4}$$

Gross thrust was then obtained by adding gross thrust minus nozzle axial force (eq. (3)), nozzle-boattail pressure drag (eq. (4)), nozzle-base pressure drag, and nozzle skin-friction drag (calculated by using the Frankl and Voishel equation for compressible, turbulent flow on a flat plate (see ref. 7)) in the following manner:

$$F_j = \left(F_j - F_{A,n} \right) + F_{A,\beta} + F_{A,base} + F_{A,f} \tag{5}$$

A total-pressure rake was used to survey the jet-total-pressure distribution at the throat of the convergent-divergent nozzles, and the integrated value of the jet total pressure at the throat was used to correct the jet-total-pressure-probe value. The mean value of the jet total pressure at the throat was used to calculate the ideal thrust for complete isentropic expansion of the jet flow from the nozzles.

Afterbody and nozzle external skin-friction drag (used for theoretical wave-drag comparisons) was calculated by using the Sommer and Short T' Method given in appendix B of reference 8.

RESULTS

The results of the investigation are presented in the following figures:

<div align="center">DISCUSSION</div>

<div align="center">Afterbody Pressure and Force Measurements</div>

Pressure distributions.- Figure 10 presents typical pressure distributions around
the afterbodies for configurations 3 to 6 at Mach numbers of 0.80 and 1.30 for the cruise-
nozzle (odd-numbered) configurations and Mach numbers of 0.80, 1.30, and 2.20 for the
afterburning-nozzle (even-numbered) configurations. Data are shown at jet-off conditions
and with jets operating near the scheduled values of jet-total-pressure ratio $\left(p_{t,j}/p_\infty\right)$
shown in figure 9. Configurations 3 (fig. 10(a)) and 4 (figs. 10(b) and 10(c)) represent the
close-spaced-afterbody configurations with the alternate (blunter) interfairing shape,
while configurations 5 (fig. 10(d)) and 6 (figs. 10(e) and 10(f)) represent the wide-spaced-
afterbody configurations with the basic interfairing shape. Jet operation generally had a
slightly favorable effect on the pressures near the end of the afterbody at M = 0.80 and
practically no effect at either supersonic Mach number. Changing from the cruise nozzles

to the afterburning nozzles (equivalent to a change from maximum dry-power position to maximum afterburning-power position on a variable primary and secondary flap convergent-divergent nozzle) produced a marked increase in the afterbody pressures near the end of the afterbody (compare configuration 3 with 4, and 5 with 6).

Figures 11 and 12 present the effects of jet operation on the interfairing pressure distributions (row 1 only) for the close-spaced and wide-spaced afterbody configurations, respectively, for Mach numbers from 0.60 to 1.30 and for $p_{t,j}/p_\infty$ ranging from 1.0 (jet off) up to approximately 8.0, depending on Mach number. Figure 13 presents the same effects for the afterburning-nozzle configurations at $M = 2.20$ and $p_{t,j}/p_\infty$ ranging from 1.0 to about 20.

By comparing the upper half of each part of figures 11 and 12 to the lower half, the differences in the basic and alternate interfairing pressure distributions can also be seen at each Mach number; and by comparing the left half of each figure part to the right half, the effect of changing from the cruise nozzles to the afterburning nozzles can be determined. Comparing like parts of figures 11 and 12 shows the effect on the interfairing pressure distributions of changing from the close-spaced afterbody to the wide-spaced afterbody. The same effect can be seen in figure 13 for $M = 2.20$ and the afterburning nozzles by comparing the upper part of the figure to the lower part.

At all subsonic Mach numbers, the lowest recorded $p_{t,j}/p_\infty$ yielded the most favorable effect on the interfairing pressures, and further increases in $p_{t,j}/p_\infty$ generally tended to decrease the interfairing pressures. For $M = 1.20$ and 1.30 the same effects were evident; but at the higher values of $p_{t,j}/p_\infty$ tested at supersonic Mach numbers, the interfairing pressures increased again, sometimes to values above those recorded for the lowest values of $p_{t,j}/p_\infty$. Comparing the pressure distributions of the basic and alternate interfairings (upper half to lower half of figure parts) indicated much lower pressures for the alternate interfairing shapes except near the end of the interfairing ($x/l \approx 0.93$) where the results were mixed, depending on nozzle spacing and nozzle configuration. Comparing the interfairing pressure distributions for the cruise-nozzle configurations to the afterburning-nozzle configurations (left half to right half of figure parts) indicated that the interfairing pressures started recovery farther upstream and generally reached higher pressures near the end of the interfairing for the afterburning-nozzle configurations. For the close-spaced afterbody (fig. 11) this effect was most noticeable with the alternate interfairing. When compared to the close-spaced afterbody, the wide-spaced afterbody generally produced more negative pressure coefficients on the interfairings, but the pressures recovered to higher values near the beginning of the nozzles (compare like parts of figs. 11 and 12).

Afterbody axial-force coefficient.- Figure 14 presents the variation of afterbody axial-force coefficient with $p_{t,j}/p_\infty$ for all test configurations and Mach numbers. Initial

operation of the jet below choked conditions generally produced the largest effect, a reduction of afterbody drag, especially at subsonic Mach numbers. Increasing $p_{t,j}/p_\infty$ above the initial jet-on value tended to first increase the drag to a maximum value at $p_{t,j}/p_\infty$ near 3.0, or slightly higher depending on Mach number, and then to slowly decrease the drag up to the highest recorded values of $p_{t,j}/p_\infty$. A large decrease in afterbody drag was indicated for changing from the cruise- to the afterburning-nozzle configurations at all Mach numbers. Both of the effects discussed above are confirmed by the interfairing pressure distributions in figures 12 and 13.

Installing the alternate interfairing on the close-spaced afterbody with cruise nozzles caused a significant afterbody drag increase; but with the afterburning nozzles it caused only a small drag increase except at supersonic Mach numbers. Installing the alternate interfairing generally had less effect on the wide-spaced afterbody than on the close-spaced afterbody, for the cruise nozzles except at several Mach numbers above 0.80 where the effects were equal (M = 0.90 and 1.3) or greater (M = 0.95). The increment in drag coefficient for the alternate interfairing seemed to be fairly constant with increasing $p_{t,j}/p_\infty$, except for the close-spaced afterbody with afterburning nozzles at M = 2.20 (fig. 14(h)) where the drag for the alternate interfairing decreased faster than for the basic interfairing, causing them to have nearly equal drag at the highest value of $p_{t,j}/p_\infty$.

Figure 15 presents the variation of afterbody axial-force coefficient with Mach number. This figure is a cross plot of data from figure 14, at values of $p_{t,j}/p_\infty$ typical of a turbofan-powered aircraft (fig. 9). The solid and dotted lines show the difference in afterbody drag coefficient between the close- and wide-spaced afterbody configurations, respectively. In all cases, the wide-spaced afterbody had the higher drag. This drag increase was fairly large $\left(C_{A,a} \text{ increment of } 0.015 \text{ to } 0.025\right)$ for all configurations and test conditions, except for configurations with afterburning nozzles at subsonic speeds and for the cruise-nozzle alternate-interfairing configurations at the lower subsonic speeds tested.

Figure 16 presents the variation of afterbody axial-force coefficient with Reynolds number for the close-spaced afterbody with the alternate interfairing and afterburning nozzles (configuration 4) at M = 2.20. These data points were taken at jet-off conditions only, while deliberately varying tunnel stagnation pressure from the lowest to the highest values possible in the 4- by 4-foot facility. The actual Reynolds number spread for all of the jet-on data taken in the 4- by 4-foot tunnel for this test at controlled temperature and pressure is shown by arrows, indicating no significant change due to Reynolds number.

Nozzle Pressure and Integrated Force Measurements

Pressure distributions.- Figure 17 presents typical longitudinal pressure-coefficient distributions on four different rows around the surface of the left nozzle for configura-

tions 3 to 6. Data are shown at Mach numbers of 0.80 and 1.30 for the cruise-nozzle (odd-numbered) configurations and Mach numbers of 0.80, 1.30, and 2.20 for the afterburning-nozzle (even-numbered) configurations at jet-off conditions and with jets operating near scheduled values of $p_{t,j}/p_\infty$. The average static-pressure coefficient around the base of the left nozzle is indicated at $x/l = 1.0$. Except for the pressures along row 4, the distributions along the nozzle surface for the cruise-nozzle configurations (configurations 3 and 5) exhibit characteristics similar to isolated nacelle distributions, with the pressures recovering rapidly toward the end of the nozzle boattail (figs. 17(a) and 17(d)). Row 4, which is in the wake of the interfairing and may be influenced by separated flow from this region − especially for the close-spaced afterbody with its blunter interfairing shape, is most noticeably affected by jet operation.

The pressure coefficient peaks near the beginning of the cylindrical afterburning nozzles reflect the recompression of the flow downstream of the rearward facing step between the afterbody and nozzles. The low pressures at the end of the nozzles ($x/l \approx 0.997$) were created by the flow around the corner into the base region of the nozzles. The base pressure coefficients averaged around this base annulus reached extremely low values (see figs. 17(b) and 17(e)) for $M = 0.80$ and 1.30 with jets operating.

Figure 18 presents the effects of jet operation on the nozzle-pressure-coefficient distributions ($\theta = 0^O$, row 2 only) for the close-spaced-afterbody (figs. 18(a) to 18(d)) and wide-spaced-afterbody (figs. 18(e) to 18(h)) configurations, respectively. Data are shown for Mach numbers of 0.60, 0.80, 0.90, and 1.30 and for values of $p_{t,j}/p_\infty$ ranging from 1.0 (jet off) up to approximately 8.0, depending on Mach number. The same effects of jet operation previously discussed for the afterbodies also were evident on the nozzles, but because of the closer proximity to the jet, the effects were much stronger and covered the entire surface of the nozzles. On the afterbody pressure distributions it was previously noted that the pressures near the end of the close-spaced afterbody, with alternate interfairing and cruise nozzles, recovered to higher values than with the basic interfairing at subsonic Mach numbers. This higher pressure also carried over onto the nozzles, as shown by comparing the upper left to the lower left parts of figures 18(a) to 18(c). The pressure coefficients on the cruise nozzles of the wide-spaced configurations, in general, were higher than for the close-spaced configurations at subsonic Mach numbers. Again, as noted previously for figure 17, the pressure coefficients near the end of the cylindrical surface and around the base annulii of the afterburning nozzles reached extremely low values (as low as -0.5) due to the pumping effects of the overexpanded nozzle flow.

Nozzle-boattail axial-force coefficient.- Since the afterburning nozzles had cylindrical boattails and therefore produced no boatta . ressure drag forces, only the forces on the cruise-nozzle configurations are presente this section. Figure 19 presents the effect of jet operation on the nozzle-boattail axial-force coefficient computed by an integration of the nozzle-boattail pressure measurements for the cruise nozzles at Mach

numbers from 0.60 to 1.30. Initial operation of the jet produced a large reduction in nozzle axial-force coefficient, but further increases in $p_{t,j}/p_\infty$ tended to increase the nozzle axial force up to $p_{t,j}/p_\infty \approx 3.0$ for the subsonic Mach numbers and up to $p_{t,j}/p_\infty \approx 3.5$ for the supersonic Mach numbers. Further increases in $p_{t,j}/p_\infty$ beyond these values again reduced the nozzle axial-force coefficient, and for some conditions, to values below those recorded at the initial jet-on point.

A comparison between the basic-interfairing and alternate-interfairing configurations shows that the alternate-interfairing configurations generally produced lower nozzle axial-force coefficients. The largest differences due to the interfairing shapes occurred for the close-spaced afterbody at $M = 0.60$ and $M = 0.70$; generally, the differences for the wide-spaced afterbodies were smaller, particularly at the lower subsonic speeds tested.

Figure 20 is a cross plot, at scheduled values of $p_{t,j}/p_\infty$, presenting the variation of nozzle-boattail axial-force coefficient with Mach number for the cruise-nozzle configurations. In this figure the data from the close- and wide-spaced afterbody configurations are plotted together for direct comparison. At all subsonic Mach numbers the wide-spaced-afterbody configurations created a flow field which produced thrust on the nozzles, except for the basic interfairing at $M = 0.95$, while the flow field resulting from the close-spaced-afterbody configurations produced drag on the nozzles except for the alternate-interfairing configuration at $M = 0.60$ and 0.70. For the wide-spaced-afterbody configuration with the basic interfairing, the nozzle drag rise near $M = 1.0$ was much more noticeable and occurred sooner than for the close-spaced-afterbody configuration. In summary, the flow field created by the different afterbody shapes resulted in lower nozzle-boattail axial-force coefficients for the wide-spaced-afterbody configurations than for the close-spaced-afterbody configurations at subsonic Mach numbers but resulted in about equal nozzle-boattail axial-force coefficients at the supersonic Mach numbers.

Total Axial-Force Coefficient

The variation of total axial-force coefficient (the sum of data from figs. 15, 20, and 24(b)) with Mach number is presented in figure 21 at scheduled values of $p_{t,j}/p_\infty$ for the cruise-nozzle configurations. This figure, plotted in the same manner as figure 20, permits a direct comparison between the close- and wide-spaced configurations. The same Mach number effects and interfairing-shape effects shown in figure 20 are also evident here, but the differences in axial force between the two spacings are strongly influenced by the dominant afterbody forces. At subsonic Mach numbers the wide-spaced configurations have a small advantage, but at supersonic Mach numbers the close-spaced configurations had better performance than the wide-spaced configurations. Since the afterburning nozzles were cylindrical, they would sense only skin-friction drag which

would be essentially constant regardless of configuration. Therefore, the effect of spacing on total axial force is the same as the effect on the afterbody alone, which showed (fig. 15) that the close-spaced configurations had lower drag through the Mach number range for either interfairing. The differences were small at subsonic speeds but significant at supersonic speeds. The choice between close- or wide-spaced configurations would be dependent on mission requirements, as well as consideration of factors other than afterbody-nozzle drag.

Theoretical Afterbody Drag Coefficients

Methods for computing wave-drag and skin-friction-drag coefficients. - The afterbody cross-sectional area progression of the alternate-interfairing configurations with cruise nozzles was calculated by a computer program for axisymmetric bodies (adapted from ref. 6) to yield a minimum wave-drag afterbody area distribution at a Mach number of 1.000001 with the restraint of a given forebody geometry, afterbody length, nozzle geometry, and an infinite cylindrical exhaust plume. It was believed, therefore, that some insight into the usefulness of the program as a design tool might be gained by comparing the measured total drag to the calculated wave drag plus skin-friction drag for three-dimensional mathematical models. The theoretical drag was determined by the methods outlined in reference 6 for nonaxisymmetric wave-drag and surface-area calculations and in reference 8 for the skin-friction-drag calculations. Figure 22 presents the machine-plotted illustrations of two typical examples of the mathematical models used in the skin-friction and wave-drag programs.

Figure 23 presents the variation of calculated wave drag for the afterbodies plus nozzles with Mach number for all the configurations. Note that the cruise-nozzles configurations which had the greatest afterbody closure (smallest bases) are all grouped together at drag levels considerably higher than the afterburning-nozzle configurations which had less closure (larger bases). The symbols with asterisks beside them denote points where violations occurred in the program due to the steep surface slopes on the interfairings and nozzles which might produce errors in the calculations.

Figure 24(a) presents the variation of calculated afterbody skin-friction axial-force coefficient with Mach number for the four afterbody configurations used in the investigation. Note that the skin-friction drag of the alternate interfairing afterbodies was lower than for the basic interfairing afterbodies, since the surface areas of these configurations were the smallest. The test conditions used for these calculations (density, static temperature, and velocity) were approximately constant for each Mach number; therefore, the differences in drag levels between configurations are approximately proportional to the surface-area differences.

16

Figure 24(b) presents the variation of calculated nozzle skin-friction axial-force coefficient with Mach number for the two different nozzle configurations, each installed with the close- and wide-spaced afterbodies. The small variation in drag shown here for like nozzle configurations probably is due to slight changes in tunnel conditions, and to the method of obtaining the comparatively small nozzle drag by taking the difference between the large skin-friction-drag level of the entire configuration and that of the entire configuration without the nozzles. The skin-friction drag of the afterburning nozzles is substantially higher than for the cruise nozzles because the surface area of the afterburning nozzles is about 26 percent greater than that of the cruise nozzles.

Comparisons with measured total axial force.- Figures 25(a) and 25(b) present comparisons of measured total-axial-force coefficient (for scheduled values of $p_{t,j}/p_\infty$) with the sum of the computed values of wave-drag coefficient and skin-friction-drag coefficient, for the close- and wide-spaced-afterbody configurations, respectively. (Note scale change.) The close-spaced-afterbody configurations with afterburning nozzles and basic interfairing gave the best agreement, and the wide-spaced-afterbody configuration with the same nozzles and interfairing was nearly as good. Very poor agreement was obtained with the cruise nozzles, indicating that the greater closure rate of the cruise nozzles created errors in the calculation of the wave drag. These errors probably would not occur for wave-drag calculations where fineness ratios of the bodies were on the order of 10 or better and, therefore, had lower local slopes.

Performance Characteristics

Effects of variation of jet-total-pressure ratio.- To facilitate conversion of aerodynamic coefficients to values ratioed to ideal thrust, the variation of aerodynamic ideal-thrust coefficient $\left(F_i/q_\infty A_{max}\right.$ or $F_i/p_a A_{max}$ for static conditions$\left.\right)$ with $p_{t,j}/p_\infty$ is presented in figure 26 for the cruise and afterburning nozzles at all test Mach numbers. The remainder of the figures to be presented, then, are all given in terms of a ratio to ideal isentropic thrust.

Figure 27 presents the variation of gross-thrust ratio with $p_{t,j}/p_\infty$ for all the configurations at $M = 0$ to $M = 1.30$. The cruise-nozzle (odd-numbered) configurations gave the highest performance at the low values of $p_{t,j}/p_\infty$, especially around $p_{t,j}/p_\infty = 3.0$; whereas the afterburning-nozzle configurations had the best performance at the highest values of $p_{t,j}/p_\infty$. This was expected since the cruise nozzles had a design $p_{t,j}/p_\infty$ of about 2.5 and the afterburning nozzles had a design $p_{t,j}/p_\infty$ near 7.4. Maximum performance for the cruise-nozzle configurations ranged from 0.947 to 0.977 and generally occurred between $p_{t,j}/p_\infty = 3.0$ and $p_{t,j}/p_\infty = 4.0$, depending on Mach number; for the afterburning nozzle configurations, no peak was reached at the maximum values of $p_{t,j}/p_\infty$ set in the Langley 16-foot tunnel investigation ($M = 0$ to 1.30).

Figure 28 presents the variation of gross-thrust minus nozzle-drag ratio $\left(F_j - F_{A,n}\right)\!/F_i$ with $p_{t,j}/p_\infty$ for the various configurations for $M = 0$ to $M = 1.30$. Because nozzle drag for the afterburning nozzles includes only skin-friction and base-pressure forces, $\left(F_j - F_{A,n}\right)\!/F_i$ for the afterburning-nozzle (even-numbered) configurations is very similar to F_j/F_i. A slight reduction in $\left(F_j - F_{A,n}\right)\!/F_i$ is produced by the extremely low base pressures acting on the nozzle bases for the supersonic Mach numbers at low values of $p_{t,j}/p_\infty$. This same effect was noted on the nozzle pressure distributions for the afterburning nozzles (see figs. 18(d) and 18(h) for examples). For the wide-spaced configurations with cruise nozzles (configurations 5 and 7) the performance was particularly good because some thrust on the nozzle boattails was actually realized at the low subsonic Mach numbers, which resulted in values of $\left(F_j - F_{A,n}\right)\!/F_i$ greater than 1.0 (see figs. 28(e) and 28(g)). Because of the high drag for the cruise nozzles ($\beta = 18.3^\circ$), $\left(F_j - F_{A,n}\right)\!/F_i$ was low for the supersonic Mach numbers for all cruise-nozzle configurations.

Figure 29 presents the variation of gross-thrust minus total-drag ratio $\left(F_j - F_{A,t}\right)\!/F_i$ with $p_{t,j}/p_\infty$ for the various configurations for $M = 0$ to $M = 1.30$. When afterbody drag is included, the performance is reduced considerably for all configurations, especially for the supersonic Mach numbers. The afterburning-nozzle configurations had the best overall performance, particularly for the high subsonic and supersonic Mach numbers.

Figure 30 presents the variation of F_j/F_i, $\left(F_j - F_{A,n}\right)\!/F_i$, and $\left(F_j - F_{A,t}\right)\!/F_i$ with $p_{t,j}/p_\infty$ for the afterburning-nozzle configurations at $M = 2.20$ only. These data were plotted separately from the transonic data because of the wider variation in $p_{t,j}/p_\infty$ (0 to 20 compared to 0 to 8). The performance of all four afterburning-nozzle configurations was good at the higher $p_{t,j}/p_\infty$ range typical of operation at $M = 2.20$ $\left(p_{t,j}/p_\infty \approx 11.0\right)$.

Effect of nozzle lateral spacing.- Figure 31, a cross plot at scheduled values of $p_{t,j}/p_\infty$, presents the variation of gross-thrust ratio with Mach number for all the configurations and permits a direct comparison between close- and wide-spaced afterbodies having similar nozzles and interfairing shapes. As indicated by the figure, F_j/F_i was essentially the same for the two spacings since all external effects have been removed. Slight differences between them may be due to differences in the internal plumbing to the nozzles and slight variations in tunnel conditions or accuracy of measuring equipment. For the cruise nozzles, maximum performance was about 0.970 and occurred between $M = 0.80$ and $M = 0.90$; for the afterburning nozzles no peak in performance was reached, but the maximum achieved was about 0.989 at $M = 2.20$.

Figure 32 is a cross plot of $\left(F_j - F_{A,n}\right)\!/F_i$ at scheduled values of $p_{t,j}/p_\infty$ so that direct comparison between the close- and wide-spaced-afterbody configurations can

be made. It is quite evident from this figure that the cruise-nozzle configurations bene-
fited greatly from the wider spacing at subsonic Mach numbers but had no advantage at
supersonic Mach numbers. The alternate interfairing shape also produced some addi-
tional gains in performance, particularly at $M = 0.90$ where $\left(F_j - F_{A,n}\right)/F_i$ reached
a value of 0.998, for the wide-spaced-afterbody configuration. For the afterburning-
nozzle configurations little or no advantage is indicated for the wide-spaced afterbodies.

Figure 33 is a cross plot at scheduled values of $p_{t,j}/p_\infty$, presenting the variation
of $\left(F_j - F_{A,t}\right)/F_i$ with Mach number for the various configurations. The strong influ-
ence of afterbody drag is very apparent if this figure is compared to figure 32. For the
cruise-nozzle configurations, $\left(F_j - F_{A,t}\right)/F_i$ decreases very rapidly between $M = 0.60$
and $M = 0.95$ and then drops as low as 0.505 at the supersonic Mach numbers. When
all external drag was included, the wide-spaced-afterbody configurations showed only a
slight advantage, and then only for the cruise-nozzle configurations at subsonic Mach
numbers. At $M = 1.20$ and 1.30 the wide-spaced configurations with the cruise nozzles
show about a 5-percent loss compared to the close-spaced configurations. For the after-
burning nozzles the configurations of the two spacing ratios had about the same perfor-
mance at subsonic Mach numbers, but the close-spaced configurations had slightly better
performance at the supersonic Mach numbers.

CONCLUSIONS

An investigation of the effect of nozzle lateral spacing and interfairing shape on the
drag and performance of twin-jet afterbodies utilizing both maximum- and minimum-
throat-area configurations of hinged-flap convergent-divergent nozzles was conducted at
Mach numbers of 0 and 0.60 to 2.20. The jet-total-pressure ratio was varied from 1.0
(jet off) to approximately 20, depending on Mach number and nozzle configuration. Two
lateral spacings of the nozzle exits were tested with the two afterbodies having similar
interfairing shapes. An alternate, blunter interfairing was also studied that had different
shapes but the same longitudinal cross-sectional area distribution for the close- and wide-
spaced afterbodies.

At scheduled jet-total-pressure ratios assumed for a turbofan engine, the following
results are indicated:

1. For the entire Mach number range, and especially at supersonic speeds, the
afterbody drag coefficient was higher for the wide-spaced configurations than for the
close-spaced configurations.

2. The nozzle axial-force coefficients were negative (thrust) on the cruise nozzles
for the wide-spaced-afterbody configurations at the lower subsonic Mach numbers tested
and were always lower than the close-spaced-afterbody configurations at subsonic Mach

numbers. However, at supersonic Mach numbers the nozzle drag was about the same for both spacing ratios.

3. For the basic interfairings, the wide-spaced afterbody with the cruise nozzles maintained some reduction in total drag as compared to the close-spaced afterbody at all subsonic Mach numbers, except 0.95.

4. At supersonic Mach numbers for both the cruise and afterburning nozzles, the close-spaced-afterbody configurations had lower total drag than the wide-spaced configurations.

5. Installing the alternate (blunter) interfairings increased the afterbody drag coefficient in all cases, and was particularly detrimental at supersonic Mach numbers. However, for the cruise-nozzle configurations, installation of the alternate interfairing reduced the nozzle drag coefficient, especially for the close-spaced afterbody at subsonic Mach numbers. As a net result, installation of the alternate interfairing had little effect on total-drag coefficient at subsonic Mach numbers but increased the total-drag coefficient at supersonic Mach numbers.

6. For the supersonic Mach numbers the sum of the calculated wave-drag and skin-friction-drag coefficients showed good agreement with the measured total-drag coefficient for the basic-interfairing configurations with the afterburning nozzles. However, the calculated drag coefficient of the cruise-nozzle configurations, which had greater afterbody closure and therefore steeper local slopes, showed very poor agreement with the measured drag, particularly for the close-spaced afterbody with the alternate interfairing where local slopes near the end of the interfairing were also quite high.

7. When comparing the effect of spacing ratio on the basis of gross-thrust minus total-drag ratio, the wide-spaced-afterbody configurations with the cruise nozzles had only a slight advantage at subsonic Mach numbers. At supersonic Mach numbers the same configurations suffered a 5-percent loss as compared to the close-spaced configurations. Adding the afterbody axial force and the nozzle-boattail axial force together (total afterbody drag) indicated that the gains in nozzle performance derived from the wider spacing are partially offset by the increased afterbody drag.

8. For the afterburning-nozzle configurations, spacing ratio had little or no effect on gross-thrust minus total-drag ratio at subsonic Mach numbers; but at the supersonic Mach numbers, the close-spaced configurations had slightly better performance.

Langley Research Center,
    National Aeronautics and Space Administration,
        Hampton, Va., July 26, 1972.

20

REFERENCES

1. Corson, Blake W., Jr.; and Runckel, Jack F.: Exploratory Studies of Aircraft After-body and Exhaust-Nozzle Interaction. NASA TM X-1925, 1969.

2. Berrier, Bobby Lee; and Wood, Frederick H., Jr.: Effect of Jet Velocity and Axial Location of Nozzle Exit on the Performance of a Twin-Jet Afterbody Model at Mach Numbers up to 2.2. NASA TN D-5393, 1969.

3. Mercer, Charles E.; and Berrier, Bobby L.: Effect of Afterbody Shape, Nozzle Type, and Engine Lateral Spacing on the Installed Performance of a Twin-Jet Afterbody Model. NASA TM X-1855, 1969.

4. Maiden, Donald L.; and Runckel, Jack F.: Effect of Nozzle Lateral Spacing on After-body Drag and Performance of Twin-Jet Afterbody Models With Convergent Nozzles at Mach Numbers up to 2.2. NASA TM X-2099, 1970.

5. Lee, Edwin E., Jr.; and Runckel, Jack F.: Performance of Closely Spaced Twin-Jet Afterbodies With Different Inboard-Outboard Fairings and Nozzle Shapes. NASA TM X-2329, 1971.

6. Harris, Roy V., Jr.: An Analysis and Correlation of Aircraft Wave Drag. NASA TM X-947, 1964.

7. Shapiro, Ascher H.: The Dynamics and Thermodynamics of Compressible Fluid Flow. Vol. II. Ronald Press Co., c.1954.

8. Peterson, John B., Jr.: A Comparison of Experimental and Theoretical Results for the Compressible Turbulent-Boundary-Layer Skin Friction With Zero Pressure Gradient. NASA TN D-1795, 1963.

TABLE I.- AFTERBODY-NOZZLE GEOMETRY

	Configurations 1 and 2	Configurations 3 and 4	Configurations 5 and 6	Configurations 7 and 8
Geometry for cruise-power nozzles (odd-numbered configurations)				
$2A_e/A_{max}$	0.124	0.124	0.124	0.124
A_e/A_t	1.035	1.035	1.035	1.035
$(p_{t,j}/p_\infty)_{design}$	2.47	2.47	2.47	2.47
L/d_t	1.79	1.79	1.79	1.79
L/d_{eng}	0.793	0.793	0.793	0.793
$2A_{eng}/A_{max}$	0.524	0.524	0.524	0.524
S_{eng}/d_{eng}	1.143	1.143	1.477	1.477
$2A_t/A_{max}$	0.120	0.120	0.120	0.120
S_{eng}/d_t	2.365	2.365	3.08	3.08
S_w/A_{max}	13.001	12.551	13.276	12.984
β, deg	18.31	18.31	18.31	18.31
Geometry for afterburning-power nozzles (even-numbered configurations)				
$2A_e/A_{max}$	0.492	0.492	0.492	0.492
A_e/A_t	1.641	1.641	1.641	1.641
$(p_{t,j}/p_\infty)_{design}$	7.42	7.42	7.42	7.42
L/d_t	1.08	1.08	1.08	1.08
L/d_{eng}	0.816	0.816	0.816	0.816
$2A_{eng}/A_{max}$	0.524	0.524	0.524	0.524
S_{eng}/d_{eng}	1.143	1.143	1.477	1.477
$2A_t/A_{max}$	0.30	0.30	0.30	0.30
S_{eng}/d_t	1.50	1.50	1.95	1.95
S_w/A_{max}	13.415	12.965	13.690	13.398
β, deg	0	0	0	0

TABLE II.- CONFIGURATION DESCRIPTION

Configuration	Nozzles	Spacing	Interfairing
1	Cruise	Close	Basic
2	Afterburning	Close	Basic
3	Cruise	Close	Alternate
4	Afterburning	Close	Alternate
5	Cruise	Wide	Basic
6	Afterburning	Wide	Basic
7	Cruise	Wide	Alternate
8	Afterburning	Wide	Alternate
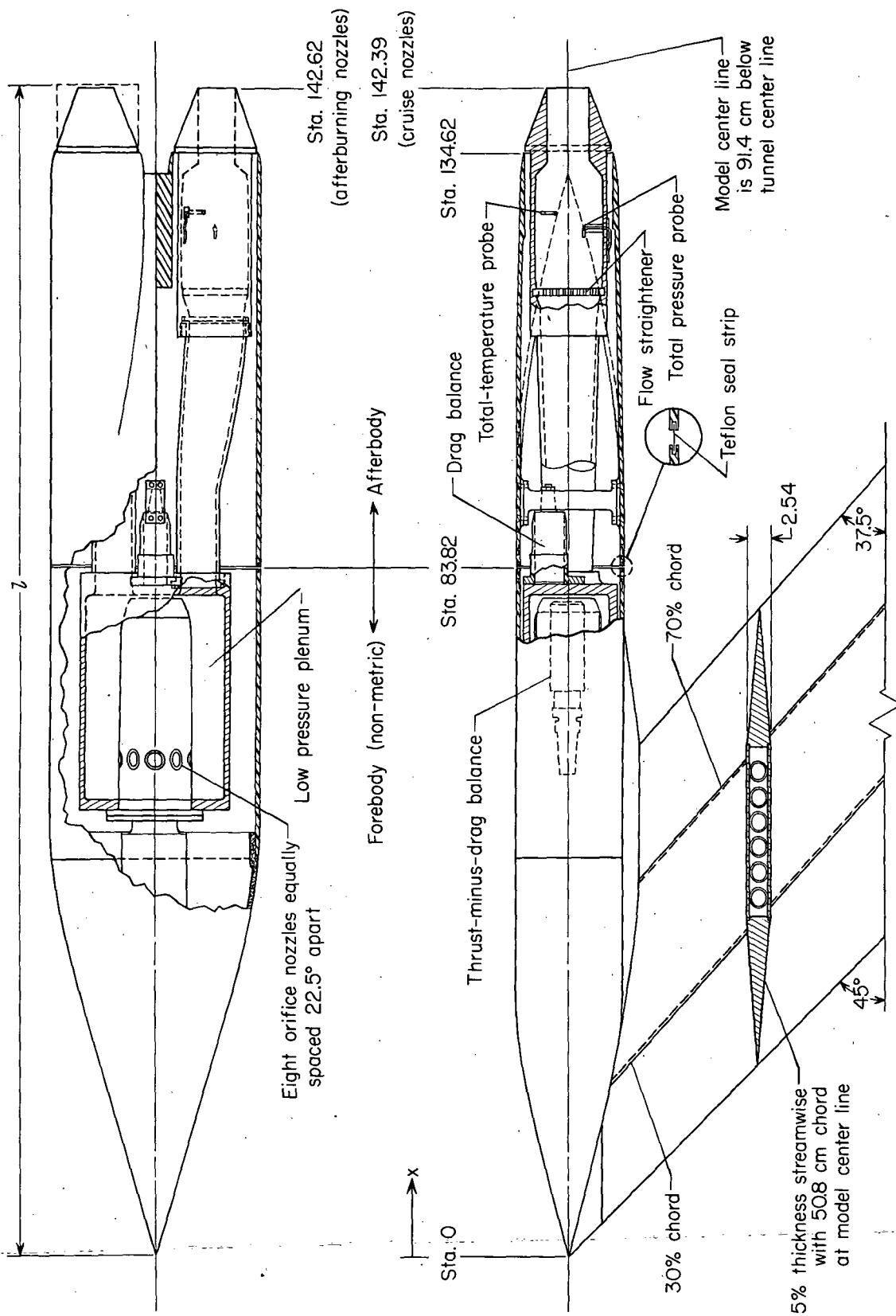
Figure 1.- Sketch of air-powered nacelle (configuration 5). All dimensions are in centimeters.

Sta. 142.62
(afterburning nozzles)

Sta. 142.39
(cruise nozzles)

Sta. 134.62

Total-temperature probe

Flow straightener

Total pressure probe

Model center line
is 91.4 cm below
tunnel center line

Teflon seal strip

Drag balance

Afterbody

Forebody (non-metric)

Sta. 83.82

2.54

70% chord

Thrust-minus-drag balance

37.5°

45°

Eight orifice nozzles equally
spaced 22.5° apart

Low pressure plenum

30% chord

5% thickness streamwise
with 508 cm chord
at model center line

Sta. 0

x

Figure 2.- Air-powered twin-jet nacelle model installed in the Langley 16-foot transonic tunnel (configuration 7 installed).
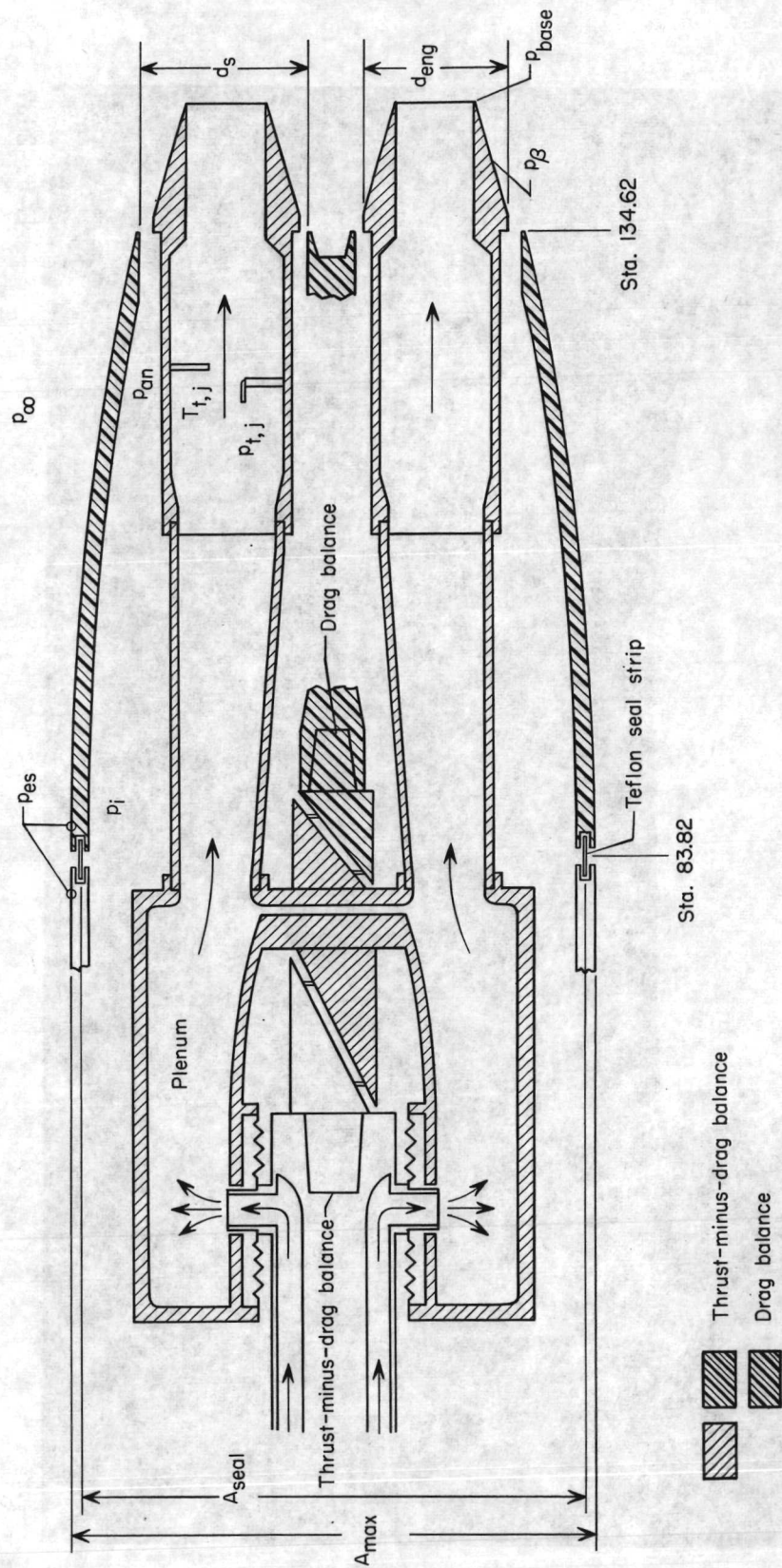
Figure 3. - Schematic showing balance arrangement and airflow paths.

Close-spaced afterbody geometry and orifice locations

Station	Nacelle geometry r	Nacelle geometry S	Interfairing geometry z_1 (basic)	Interfairing geometry z_2 (alternate)	Row 1	Row 2	Row 3	Row 4	Row 5-8	x/l
83.82	6.350	6.350	6.350	6.350	X					0.623
88.90	6.350	6.350	6.350	6.350						
91.44	6.350	6.350	6.299	6.350	X		X			.677
93.98	6.350	6.350	6.172	6.350						.695
96.52	6.350	6.350	6.020	6.350			X			
99.06			5.766	6.342						.730
101.60	6.309	6.308	5.486	6.330						
104.14			5.156	6.309		X				
106.68			4.801	6.287						.766
109.22			4.394	6.248		X				
111.76			3.988	6.198						.801
114.30	6.172	6.134	3.556	6.121	X	X	X			.837
116.84			3.099	6.045						
119.38	6.045	5.994	2.642	5.918	X	X	X			.873
121.92			2.108	5.664						.891
124.46	5.888	5.872	1.676	5.258	X	X	X			.908
127.00			1.270	4.674	X	X	X			.917
129.54	5.664	5.664	.838	3.734	X	X	X			.926
130.81			.610		*X	X	X	*X	X	.935
132.08	5.512	5.547	.406	1.270	X	X	X			
133.35		5.547								
134.62	5.131	5.547								

* Same orifice

Sta. 134.62

50.643

25.4

S_{eng}

Engine $\mathbb{C}$

5.547

z_2

z_1

12.7

Row 1
Row 2
Row 3
Row 4
Row 5
Row 6
Row 7
Row 8
r
S
12.7
56.25°
45°
67.5°
78.75°

(a) Close-spaced afterbody geometry and orifice locations. All dimensions are in centimeters.

Figure 4.— Sketches of afterbody geometry and orifice locations (nozzles not shown).

27
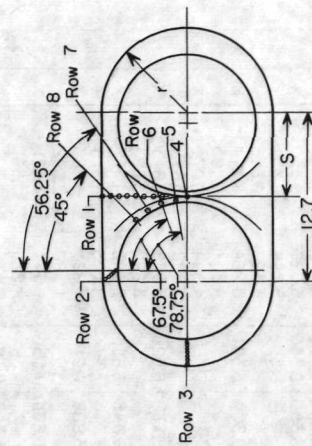
Wide-spaced afterbody geometry and orifice locations

Nacelle geometry			Interfairing geometry		Orifice locations						x/l
Station	r	S	z_1 (basic)	z_2 (alternate)	Row 1	Row 2	Row 3	Row 4	Row 5–7	Row 8	
83.82	6.350	6.350	6.350	6.350	X						0.623
88.90	6.350	6.350	6.350	6.350							
91.44	6.350	6.350	6.299	6.350							
93.98	6.350	6.350	6.172	6.350							
96.52	6.350	6.358	6.020	6.350	X						.677
99.06			5.766	6.342							
101.60			5.486	6.325							
104.14	6.309	6.391	5.156	6.274	X	X	X				.730
106.68			4.801	6.185							
109.22			4.394	6.071	X						.766
111.76			3.988	5.893							
114.30	6.172	6.528	3.556	5.613	X						.801
116.84			3.099	5.283							
119.38	6.045	6.655	2.642	4.877	X	X					.837
121.92			2.108	4.318							
124.46	5.888	6.812	1.621	3.683	X	X	X			X	.873
127.00	5.664	7.036	1.080	2.692	X	X	X				.891
129.54			.541	1.321	X	X					.908
130.81			.279	.661	X	X	X	X	X		.917
132.08	5.512	7.188	0	0	X	X			X	X	.926
133.35					X	X				X	.935
134.62	5.131	7.239									

(b) Wide-spaced afterbody.

Figure 4.– Concluded.
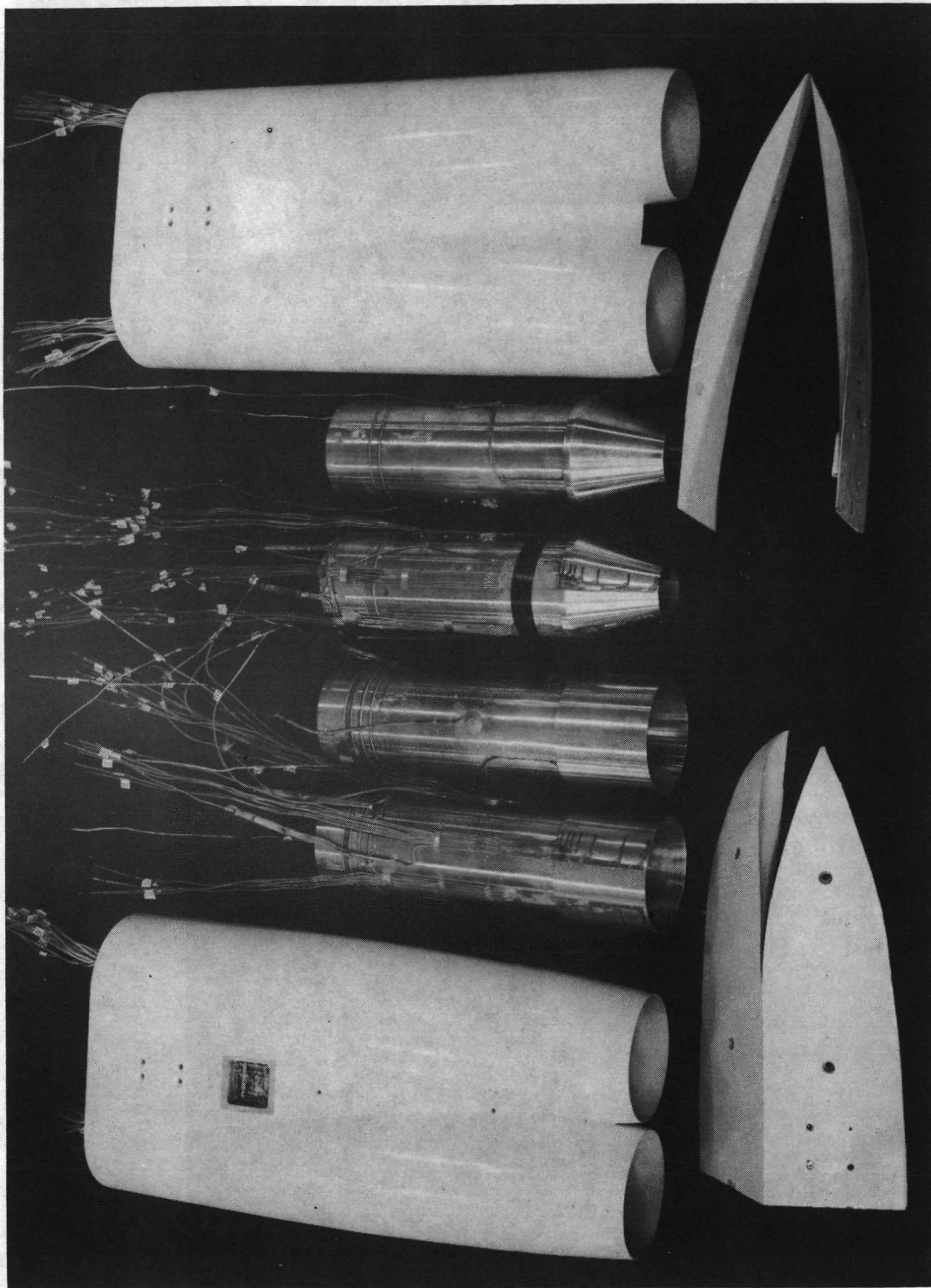
L-71-8295

(a) Photograph of afterbodies, nozzles, and interfairings.

Figure 5. - Photographs of model parts.

29
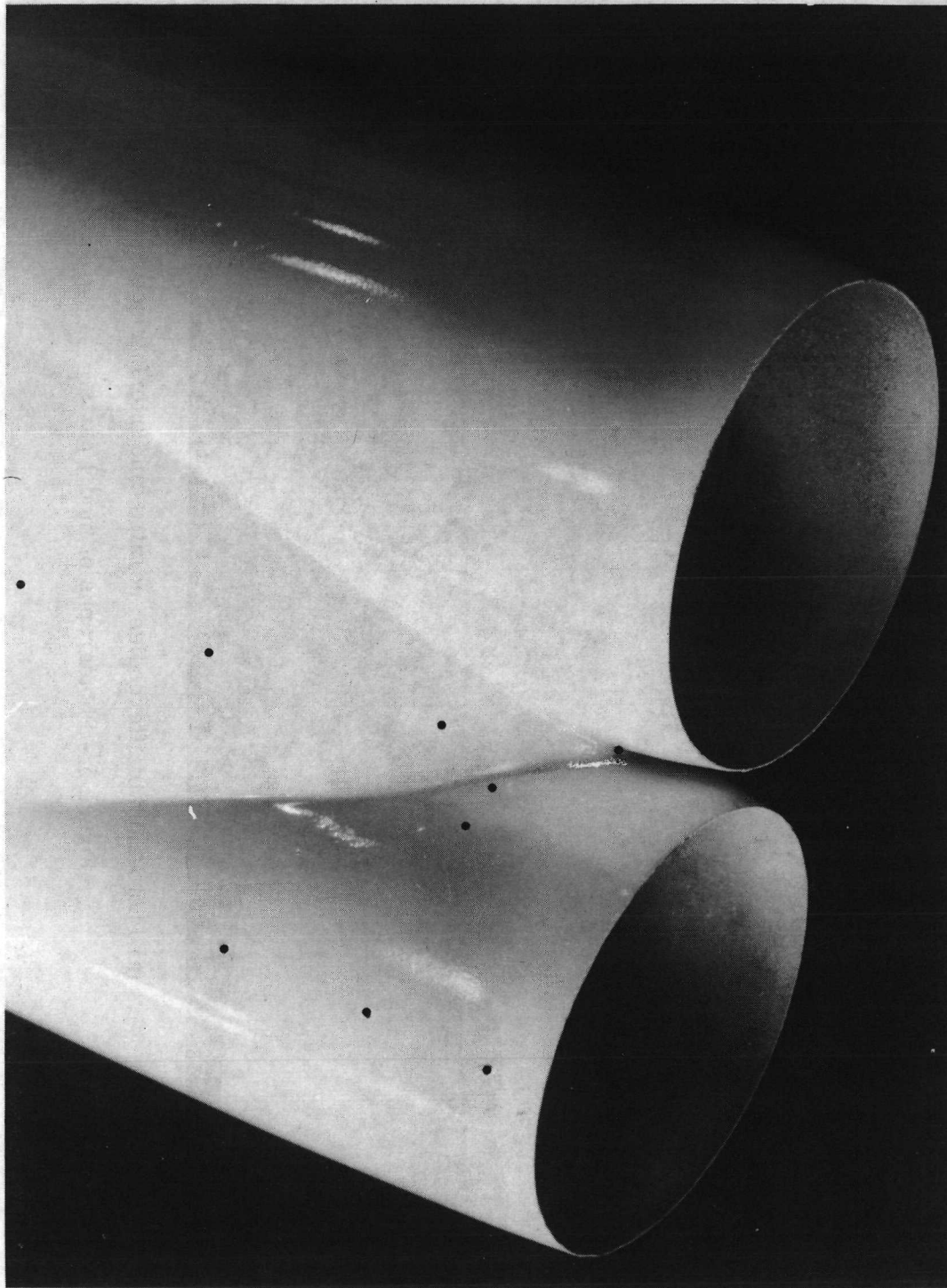
L-70-7093

(b) Detail photograph of close-spaced afterbody around interfairing-nacelle juncture (configuration 3, 4).

Figure 5.- Continued.
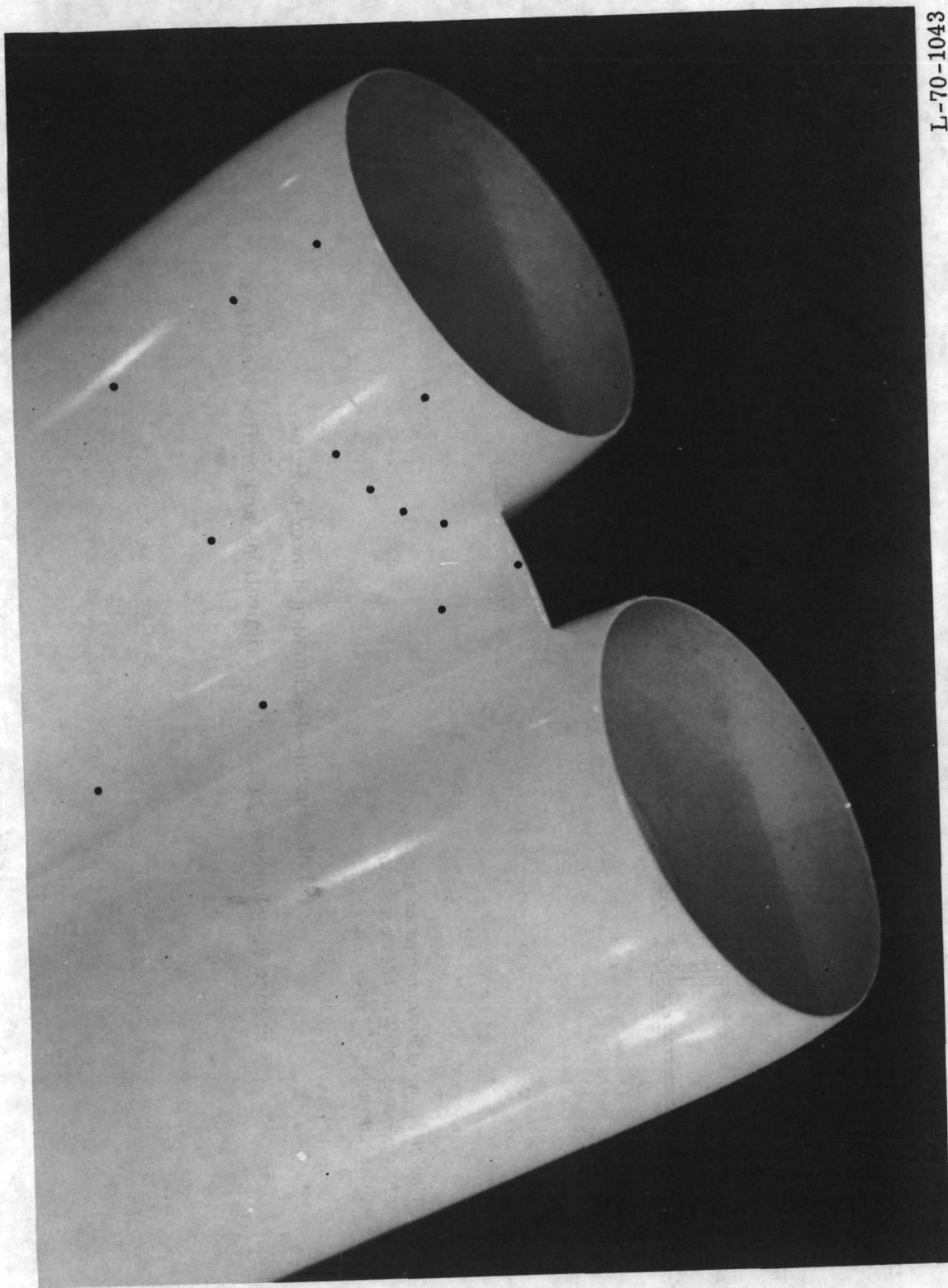
L-70-1043

(c) Detail photograph of wide-spaced afterbody around interfairing-nacelle juncture (configuration 5, 6).

Figure 5.- Concluded.
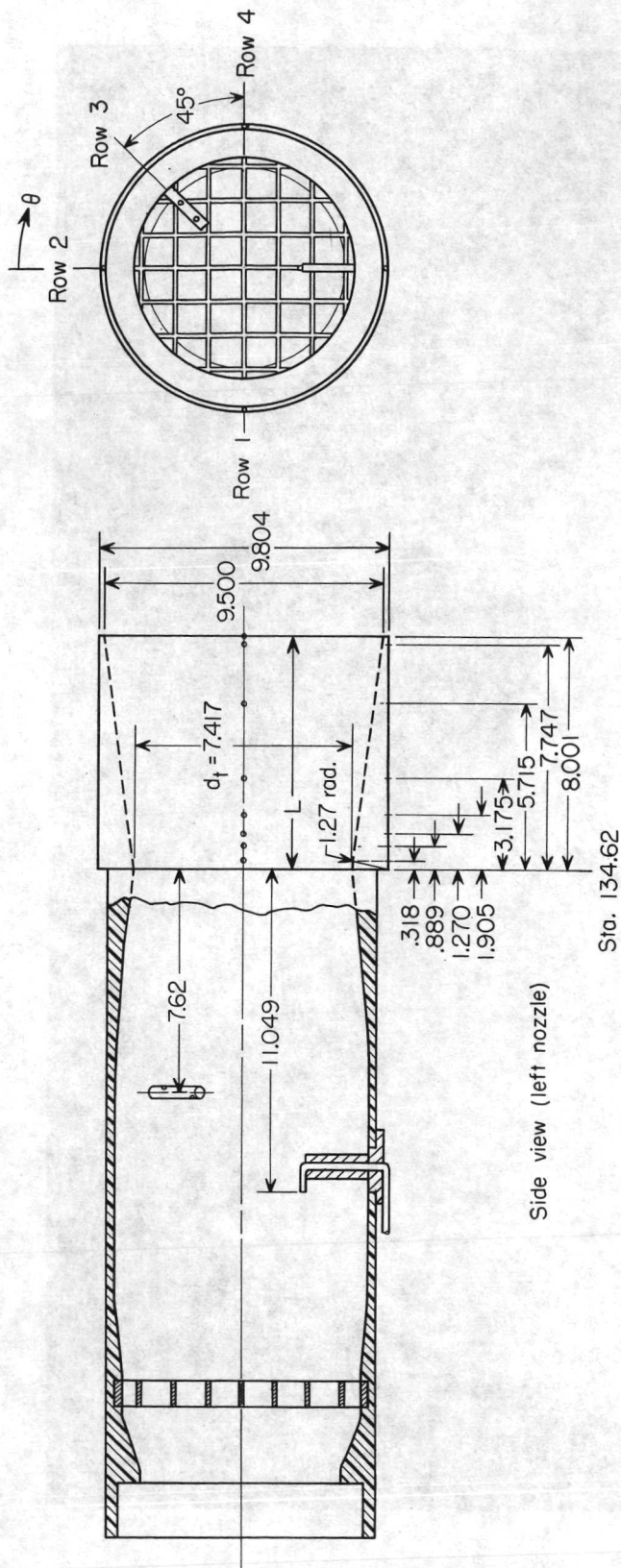
Row 4

Row 3

45°

θ

Row 2

Row 1

9.804

9.500

$d_t = 7.417$

L

1.27 rad.

7.747

8.001

5.715

3.175

.318
.889
1.270
1.905

7.62

11.049

Side view (left nozzle)

Sta. 134.62

Note: Left nozzle, only, is instrumented on external
surface—4 rows of 7 orifices each, plus
4 base pressures 90° apart—(see end view).

(a) Maximum-afterburning-power nozzles.

Figure 6.- Sketches of nozzle configurations and orifice locations.
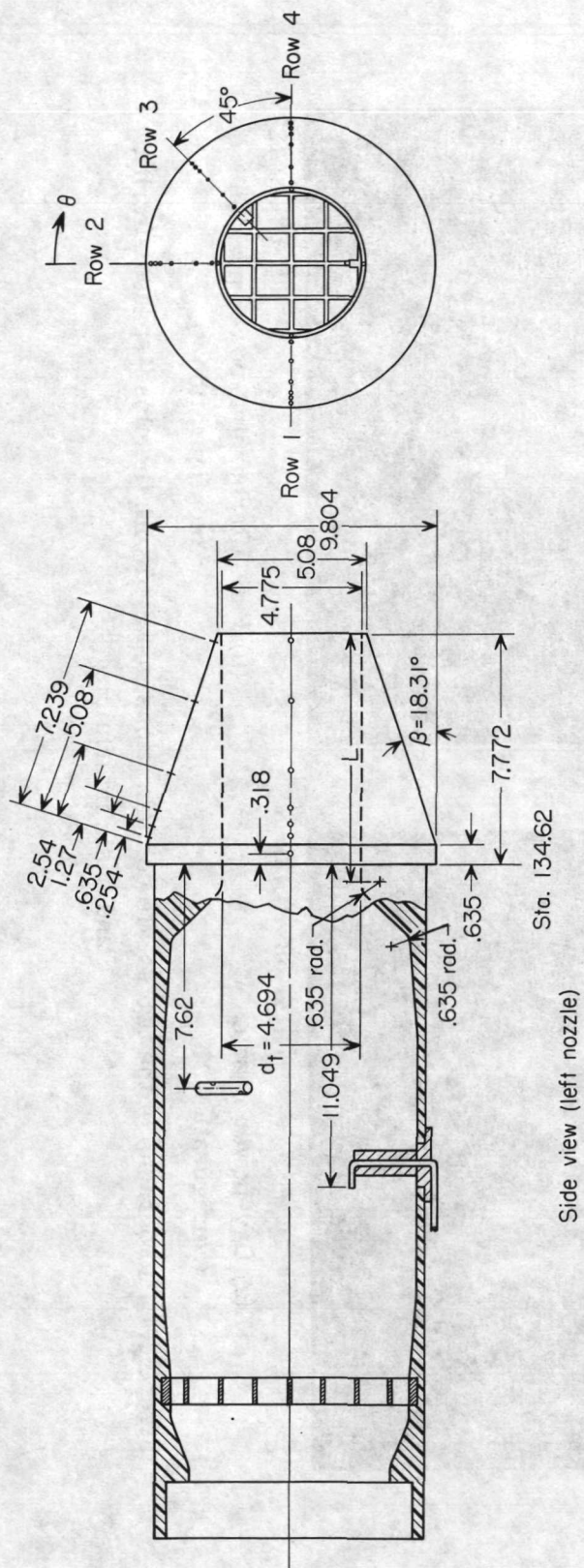
32

Side view (left nozzle)

Note: Left nozzle, only, is instrumented on external
surface—4 rows of 7 orifices each, plus
4 base pressures 90° apart—(see end view).

(b) Dry-power nozzles.

Figure 6. – Concluded.

33
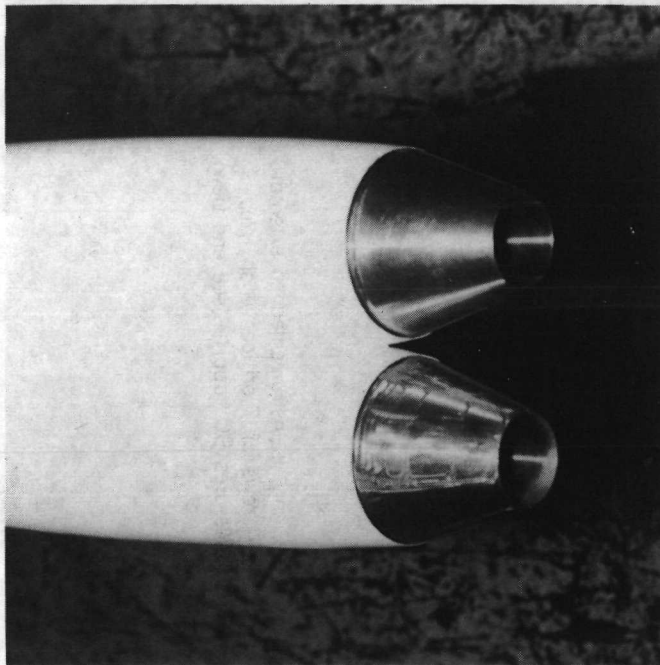
L-68-10 169

(a) Dry-power nozzles
(configuration 1).
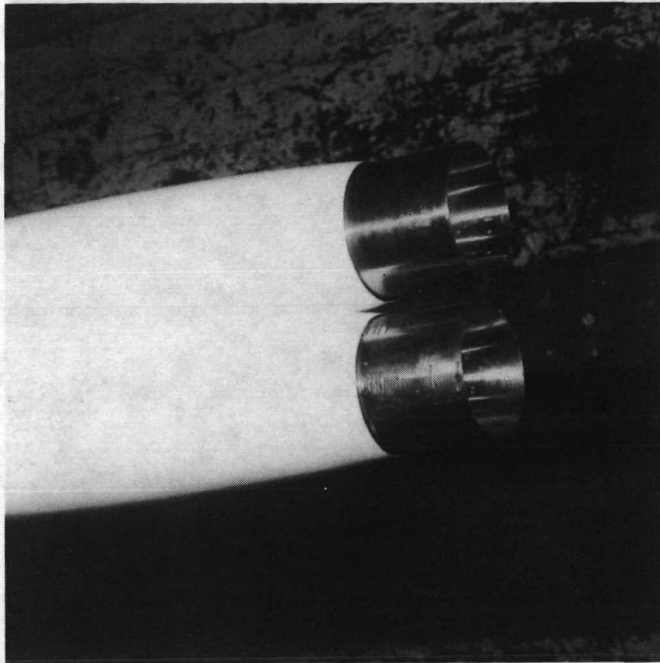
L-68-10 122

(b) Full-afterburning-power nozzles
(configuration 2).

Figure 7.- Photographs of the two nozzle configurations installed with the close-spaced afterbody and basic interfairing.

34
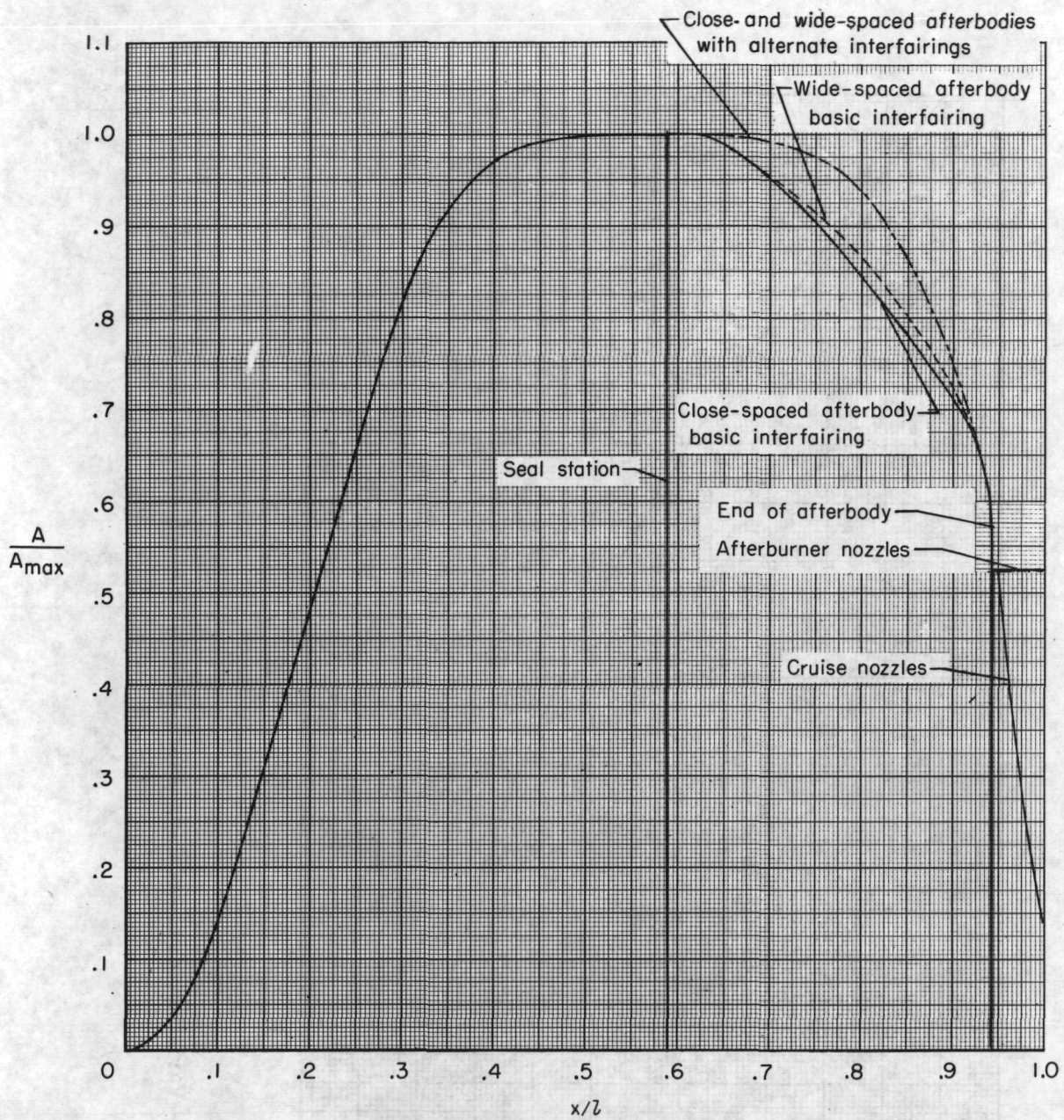
Figure 8.- Cross-sectional area distributions for the various afterbodies and nozzles.

35
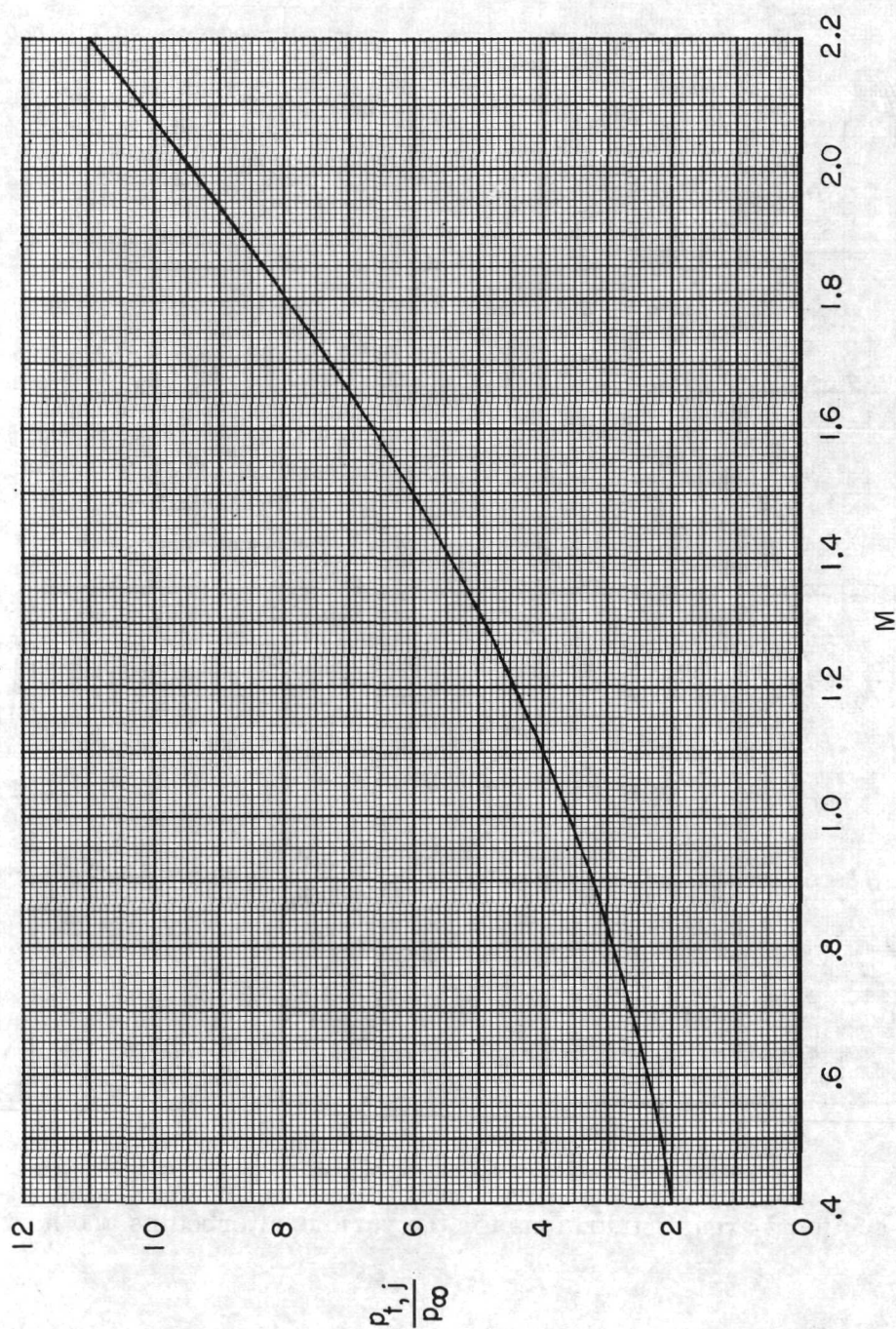
Figure 9. - Variation of jet-total-pressure ratio with Mach number for a schedule typical of a turbofan-engine configuration.
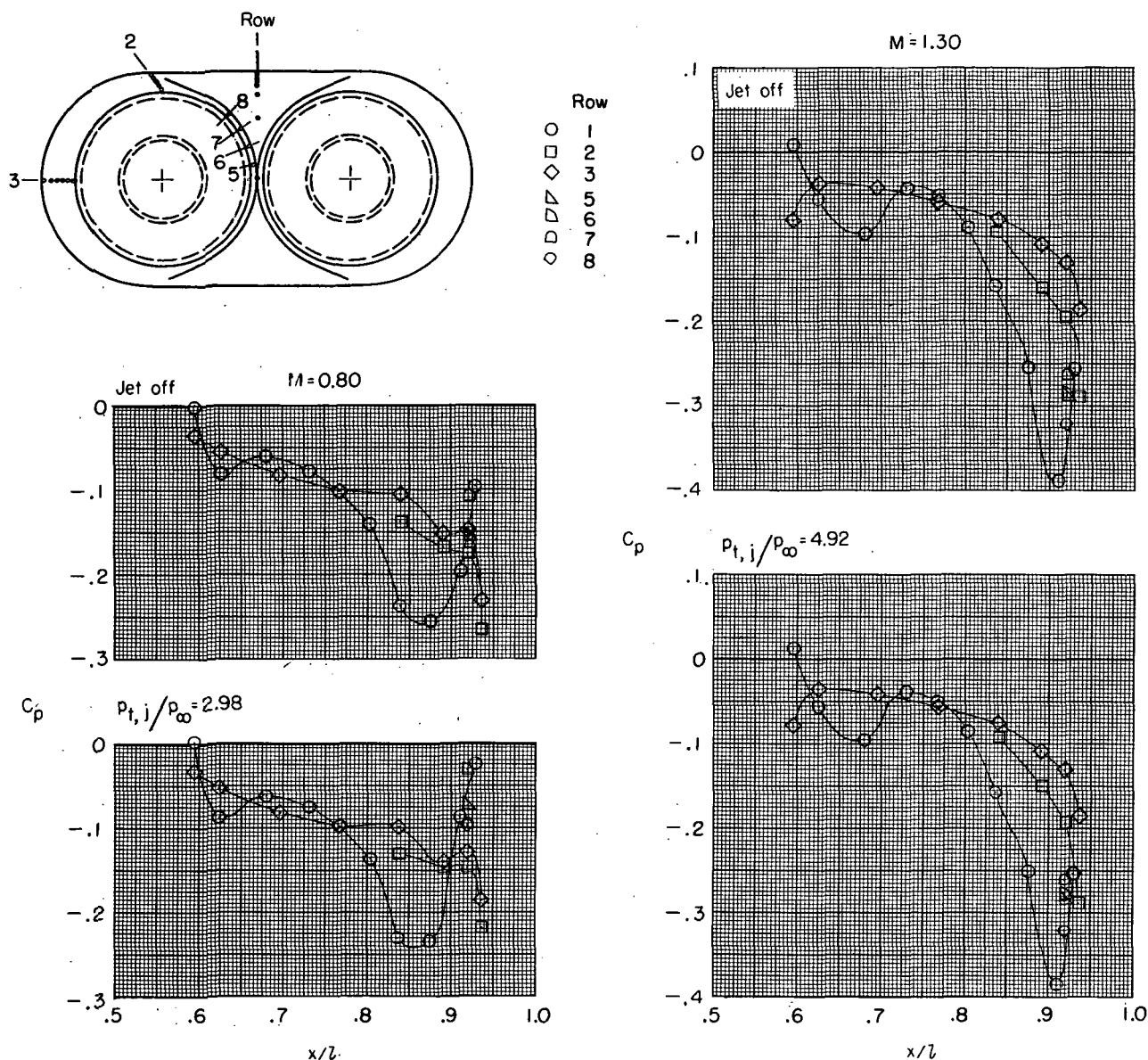
(a) Configuration 3 (close-spaced, alternate interfairing, cruise nozzles).

Figure 10.- Typical examples of pressure distributions from rows around the afterbody for jet-off conditions and near scheduled jet-total-pressure ratios.
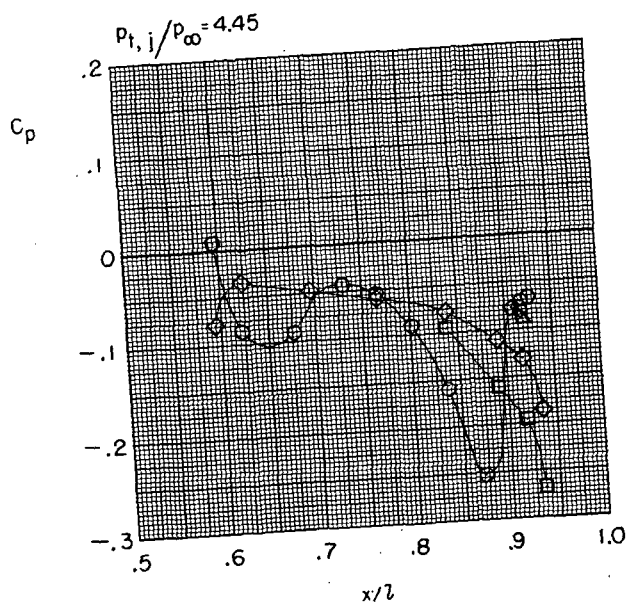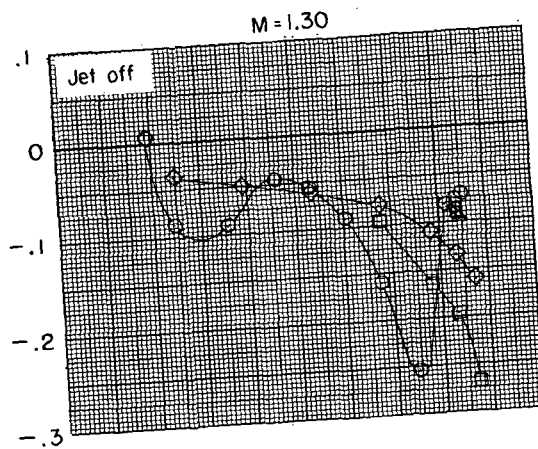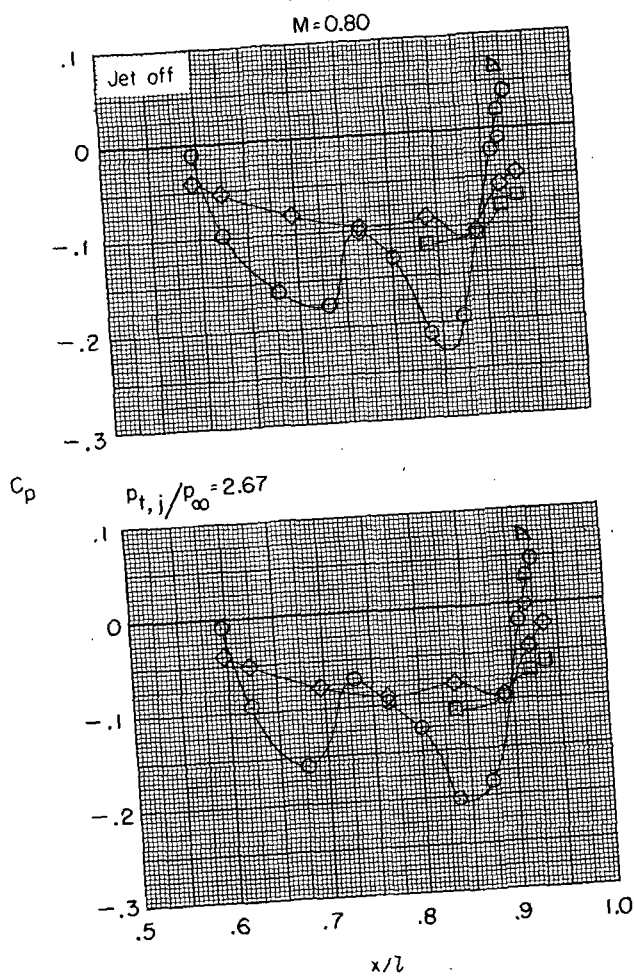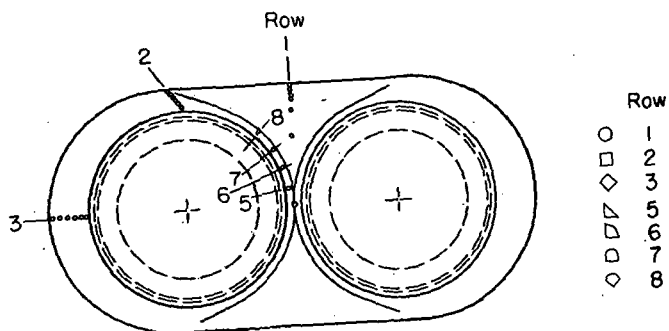
(b) Configuration 4 (close-spaced, alternate interfairing, afterburning nozzles).

Figure 10.- Continued.

Row
○   1
□   2
◇   3
△   5
◻   6
◻   7
◇   8

Jet off

.1

0

−.1

−.2

C_p

$p_{t,j}/p_\infty = 8.97$

.1

0

−.1

−.2

.5   .6   .7   .8   .9   1.0

x/l
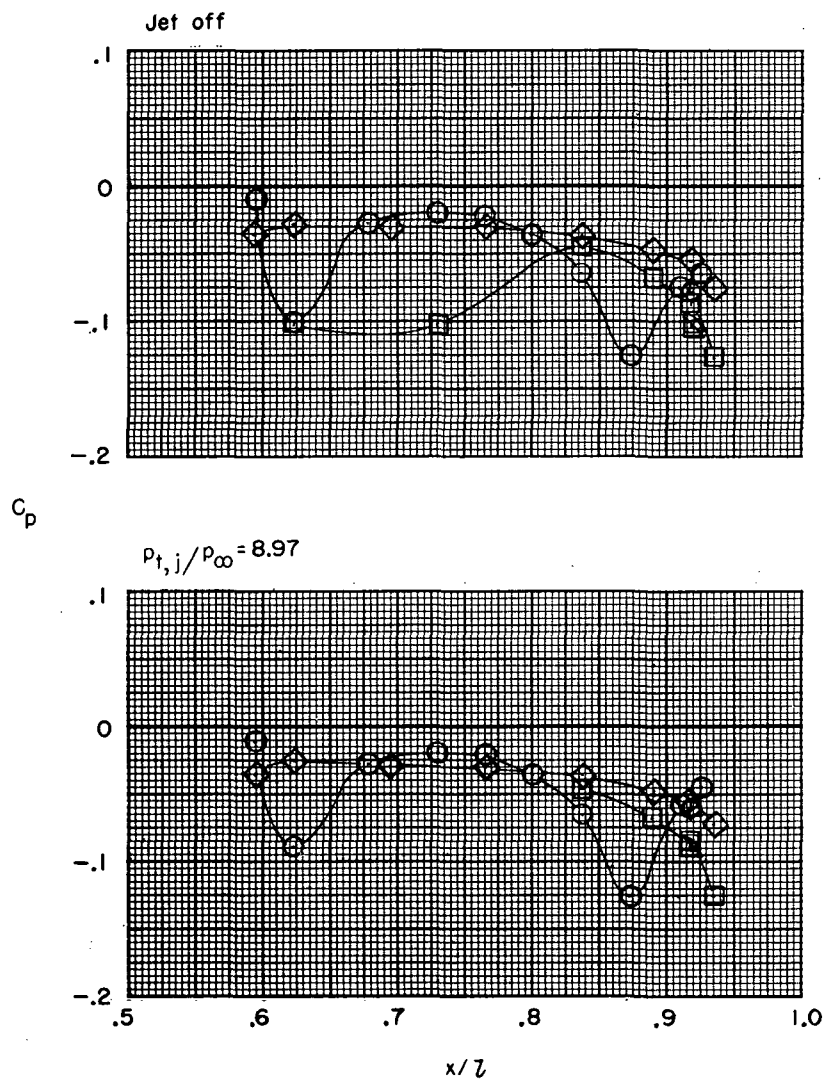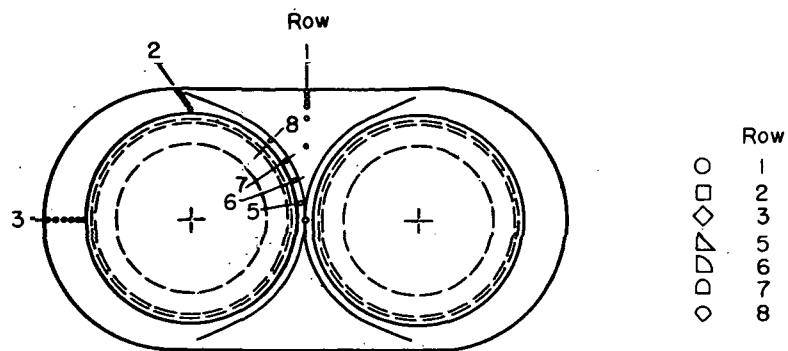
(c) Configuration 4 (close-spaced, alternate interfairing,
afterburning nozzles);   M = 2.20.

Figure 10.- Continued.
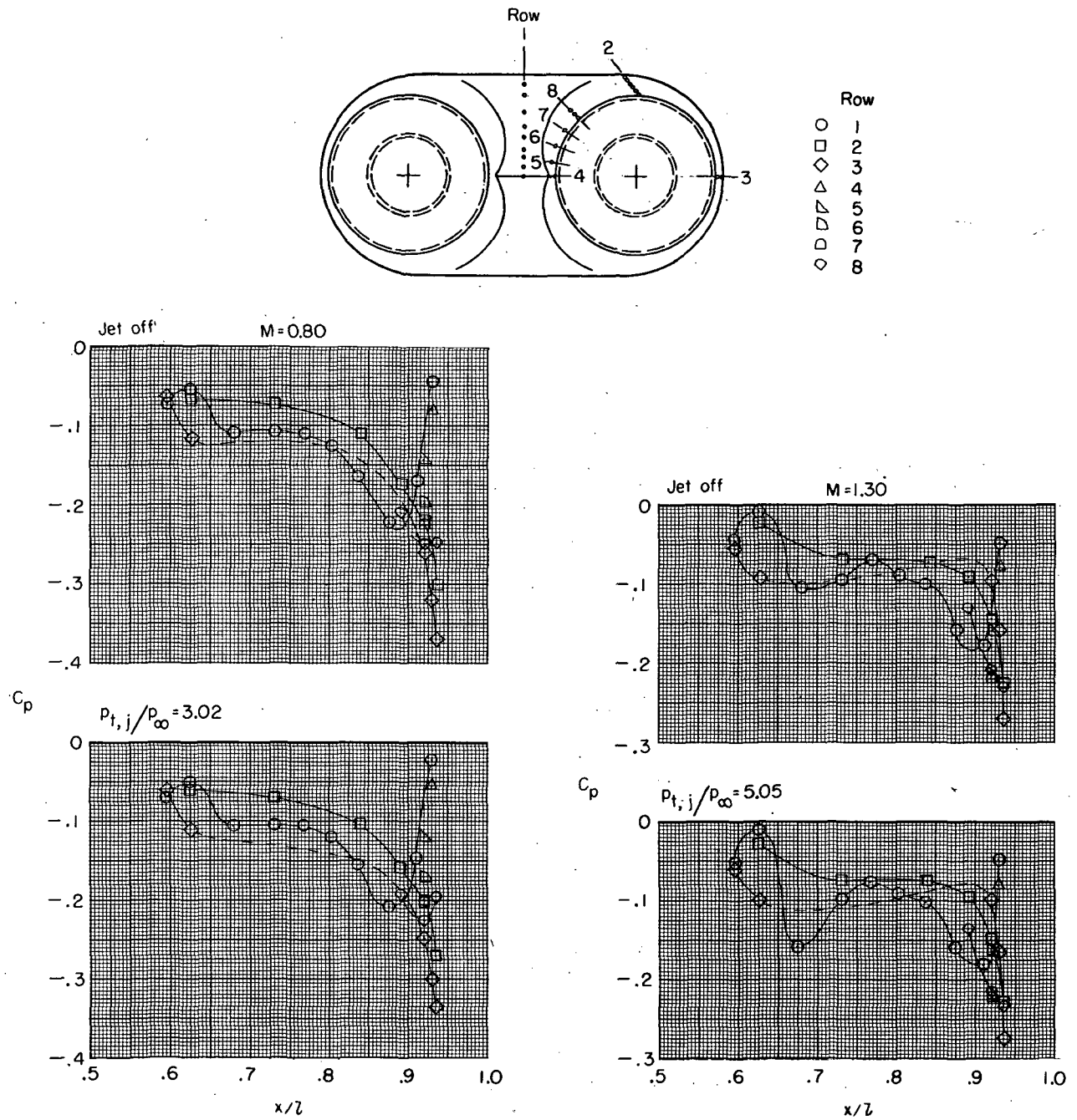
(d) Configuration 5 (wide-spaced, basic interfairing, cruise nozzles).

Figure 10.- Continued.
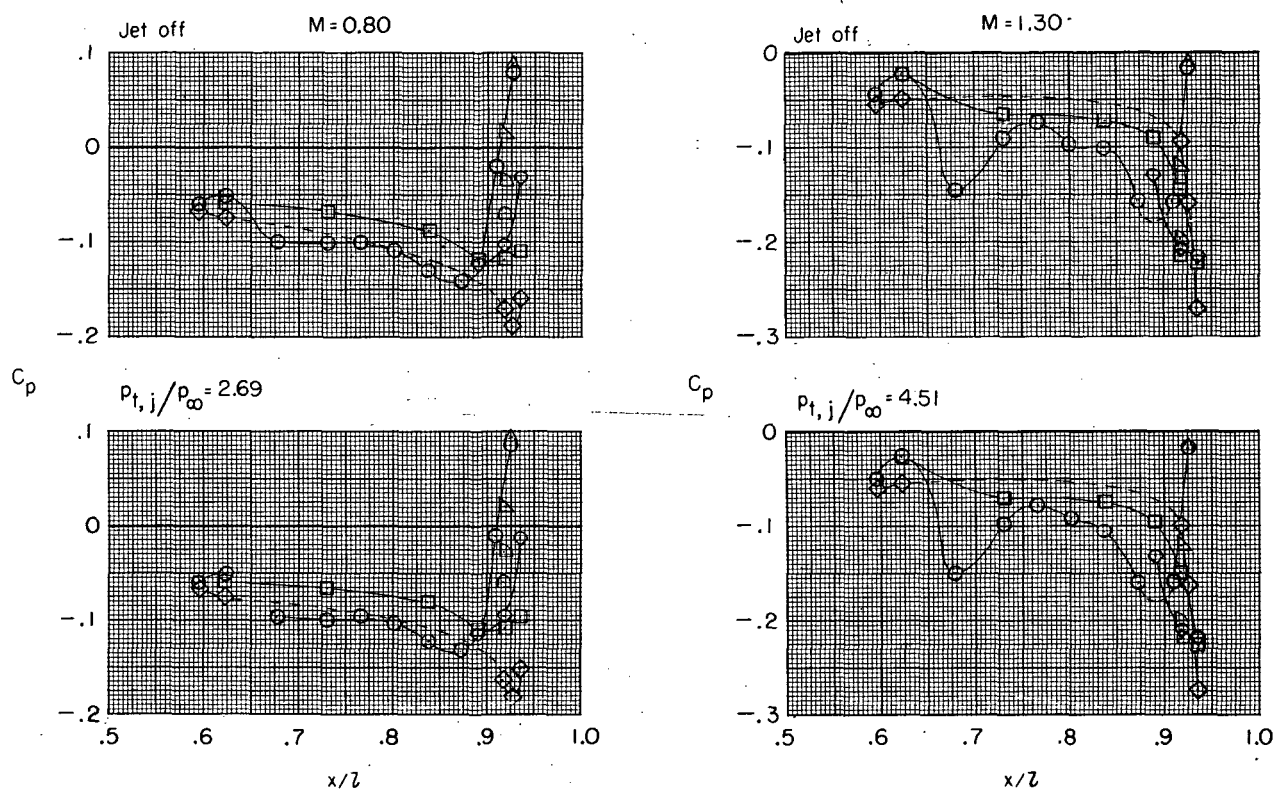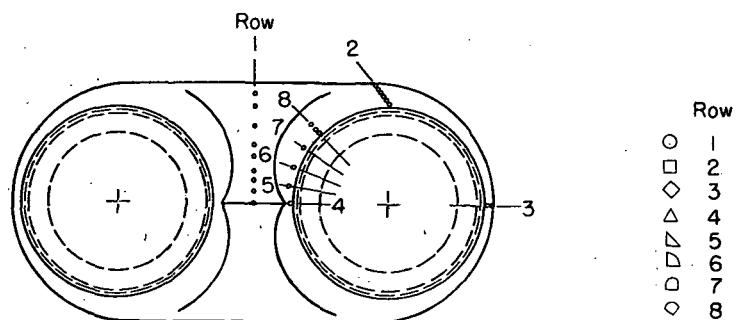
(e) Configuration 6 (wide-spaced, basic interfairing, afterburning nozzles).

Figure 10.- Continued.
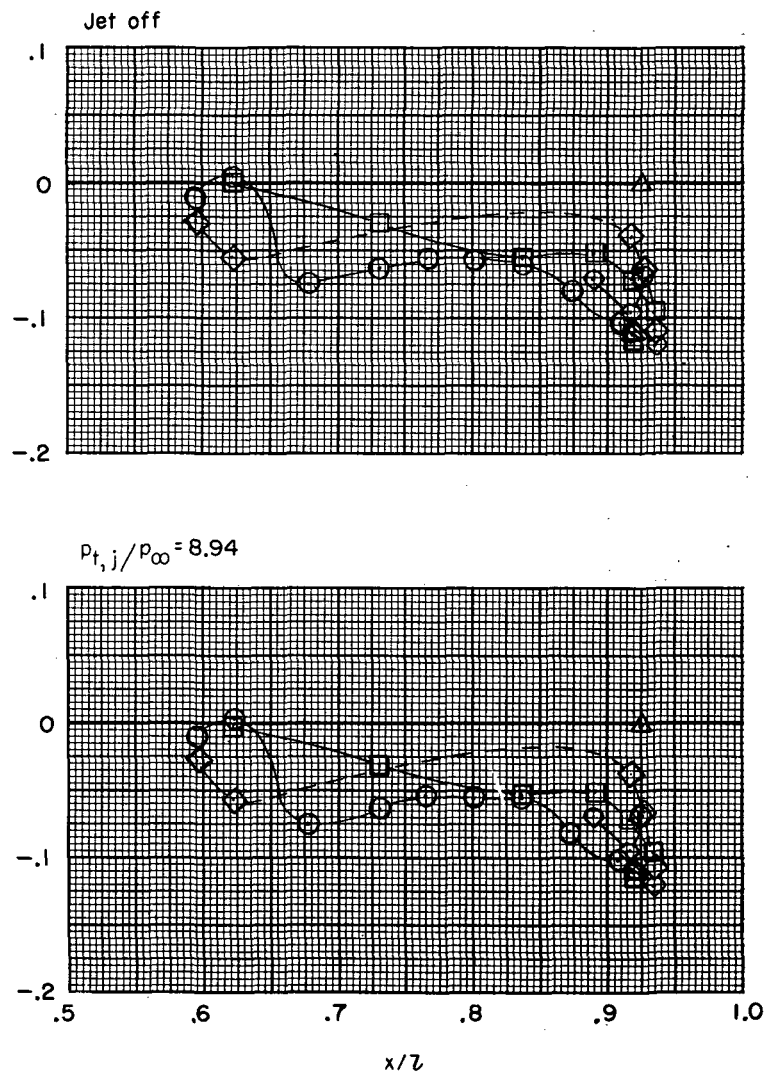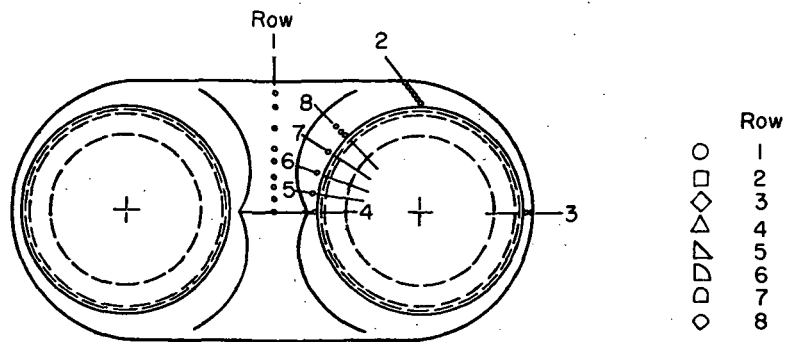
(f) Configuration 6 (wide-spaced, basic interfairing,
afterburning nozzles); M = 2.20.

Figure 10.- Concluded.

Cruise nozzles

Afterburning nozzles

Configuration 1

Configuration 2

Basic interfairing

$p_{t,j}/p_\infty$

○ 1.02
□ 1.60
◇ 3.00
△ 4.97

$p_{t,j}/p_\infty$

○ 0.95
□ 1.44
◇ 2.69
△ 3.92

Configuration 3

Configuration 4

Alternate interfairing

$C_{p,if}$

$p_{t,j}/p_\infty$

○ 1.03
□ 1.59
◇ 3.00
△ 4.93

$p_{t,j}/p_\infty$

○ 0.85
□ 1.44
◇ 2.65
△ 3.96

x/l
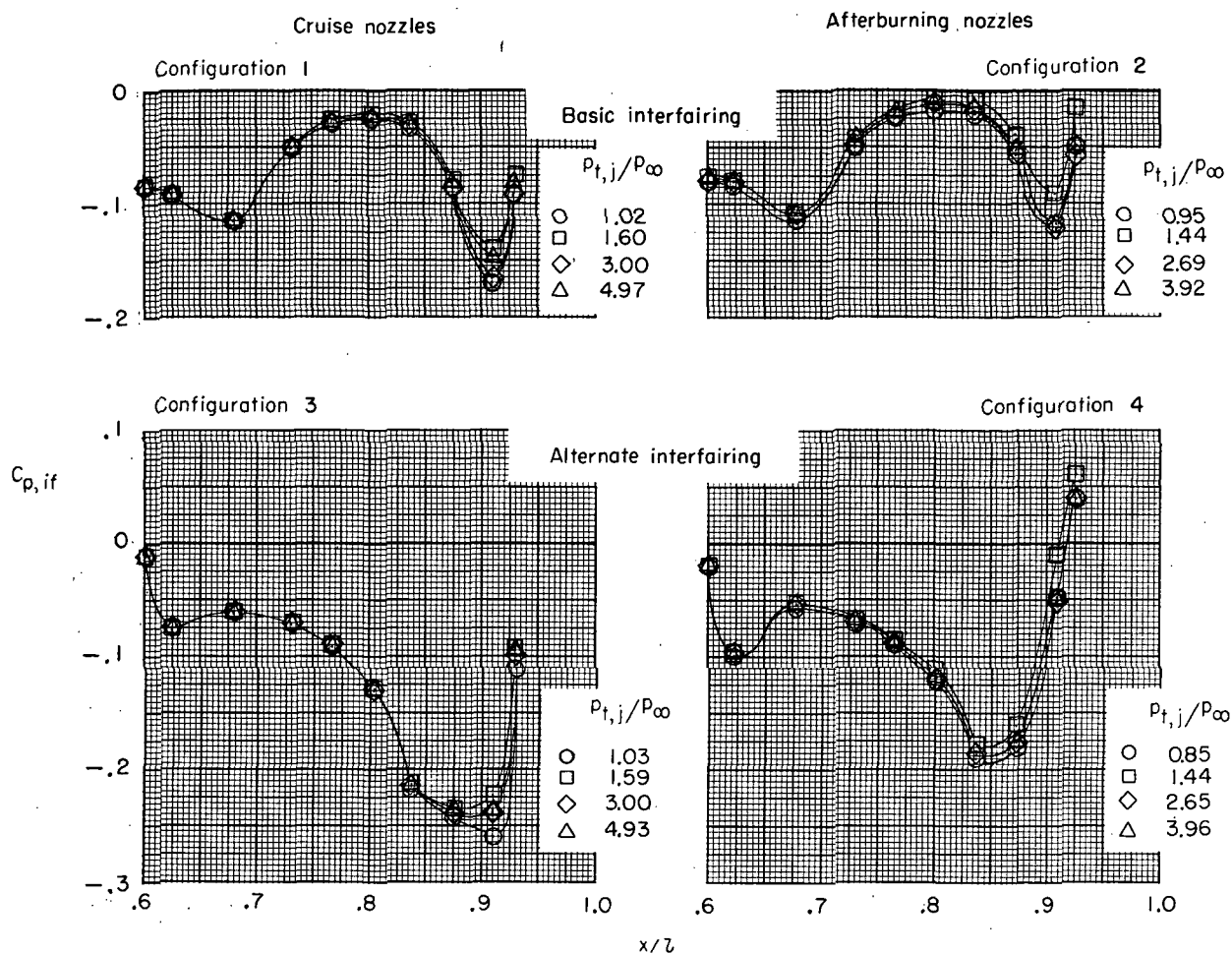
(a) M = 0.60.

Figure 11.- Effect of jet operation on the interfairing pressure distributions (row 1) for the close-spaced-afterbody configurations at transonic Mach numbers.
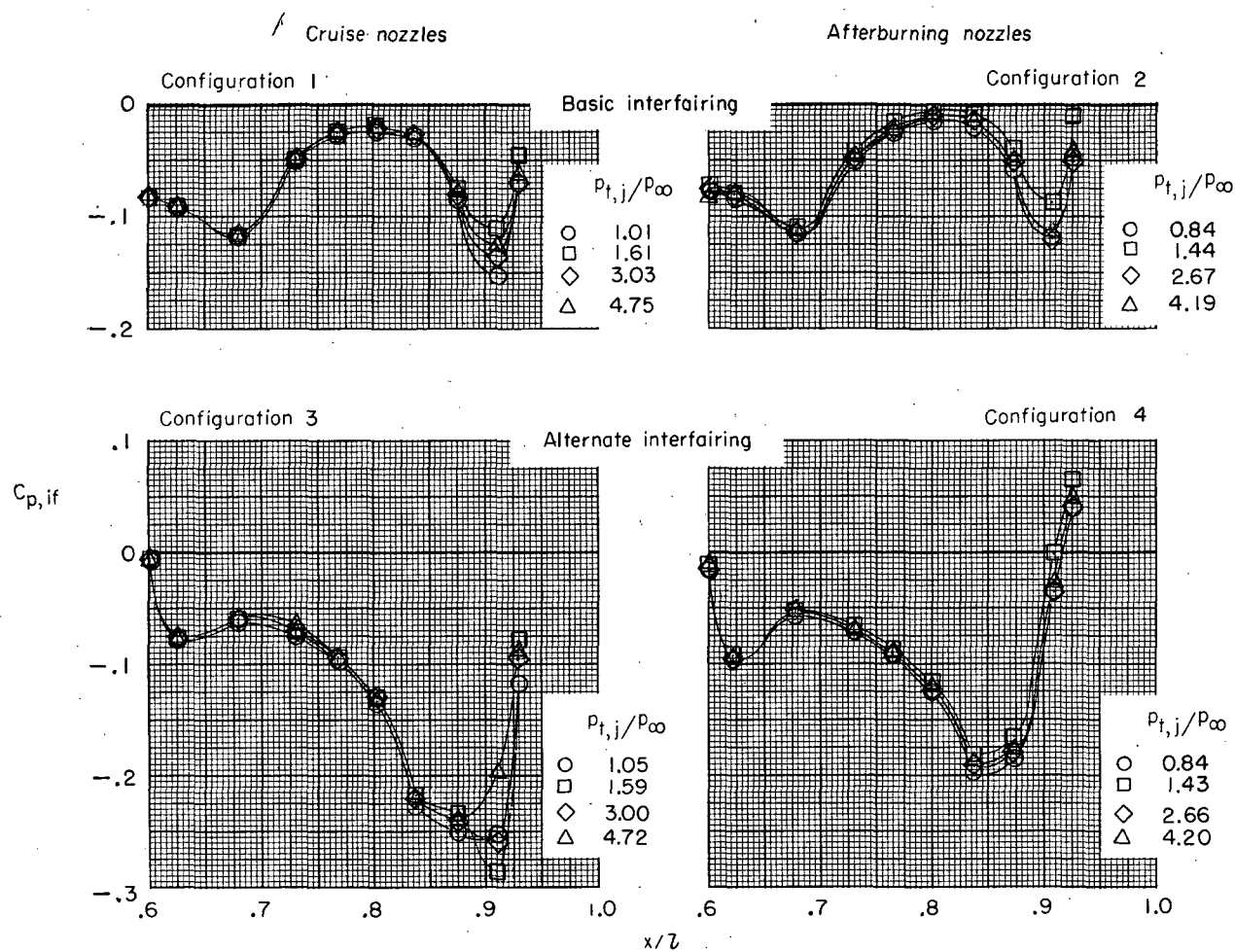
(b)   M = 0.70.

Figure 11.- Continued.

(c) M = 0.80.

Figure 11.- Continued.
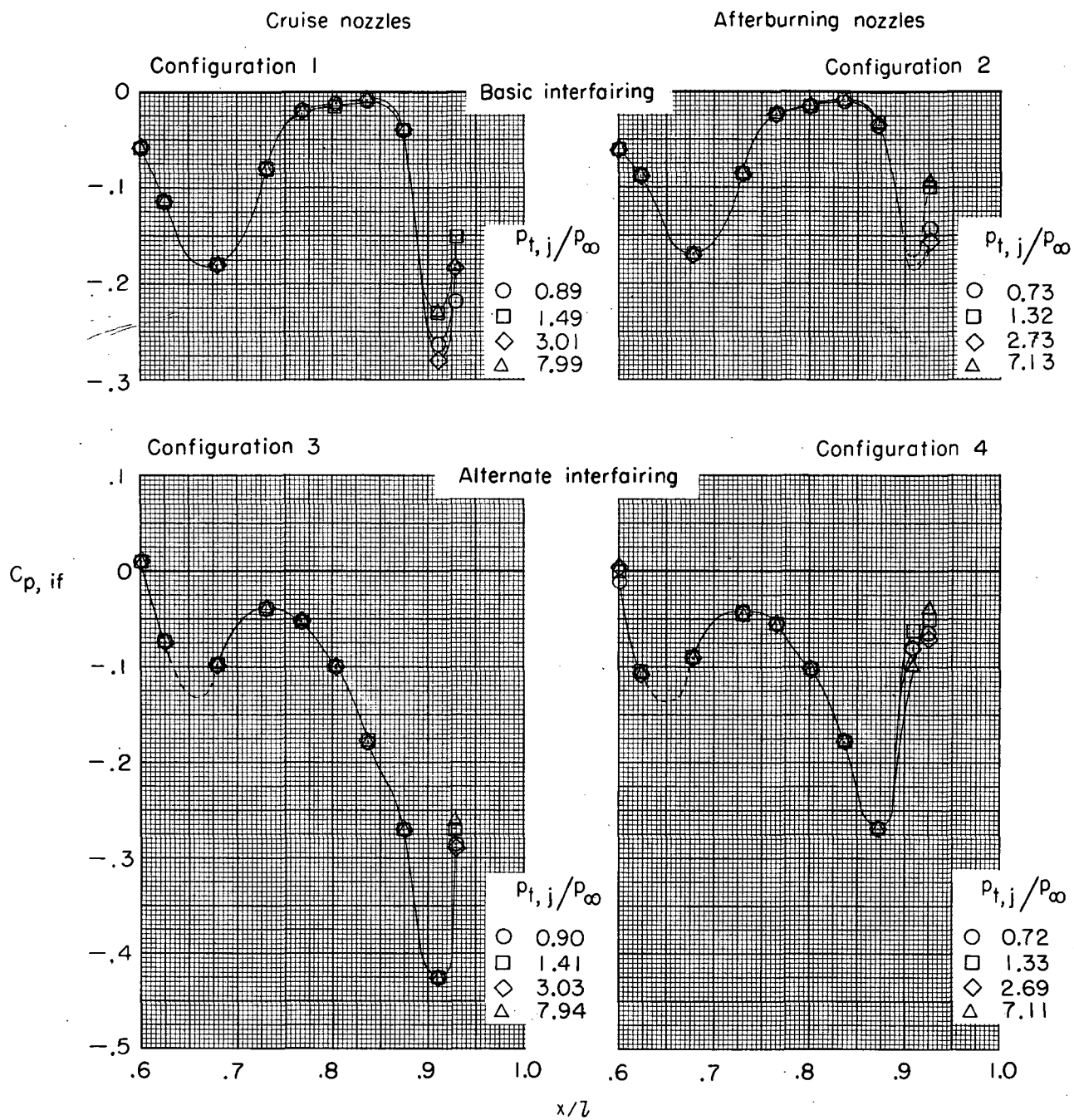
Cruise nozzles

Afterburning nozzles

Configuration 1

Configuration 2

Basic interfairing

$p_{t,j}/p_\infty$

○ 0.98
□ 1.56
◇ 3.02
△ 5.97

$p_{t,j}/p_\infty$

○ 0.82
□ 1.36
◇ 2.69
△ 5.27

$C_{p,if}$

Configuration 3

Configuration 4

Alternate interfairing

$p_{t,j}/p_\infty$

○ 1.03
□ 1.48
◇ 3.00
△ 5.92

$p_{t,j}/p_\infty$

○ 0.82
□ 1.32
◇ 2.70
△ 5.26

x/l

(d)   M = 0.90.

Figure 11.- Continued.

46

Cruise nozzles

Configuration 1

Afterburning nozzles

Configuration 2

Basic interfairing

$p_{t,j}/p_\infty$

○   0.97
□   1.68
◇   3.01
△   5.96

$p_{t,j}/p_\infty$

○   0.81
□   1.45
◇   2.74
△   5.27

Configuration 3

Configuration 4

Alternate interfairing

$C_{p,if}$

$p_{t,j}/p_\infty$

○   1.00
□   1.72
◇   3.02
△   5.92

$p_{t,j}/p_\infty$

○   0.81
□   1.44
◇   2.67
△   5.26

x/l

(e)   M = 0.95.

Figure 11.- Continued.

(f) M = 1.20.

Figure 11.- Continued.

Cruise nozzles

Afterburning nozzles

Configuration 1

Basic interfairing

Configuration 2

$p_{t,j}/p_\infty$

○ 0.86
□ 1.50
◇ 2.94
△ 7.89

$p_{t,j}/p_\infty$

○ 0.69
□ 1.32
◇ 2.68
△ 7.06

Configuration 3

Alternate interfairing

Configuration 4

$C_{p,if}$

$p_{t,j}/p_\infty$

○ 0.73
□ 1.45
◇ 2.98
△ 7.52

$p_{t,j}/p_\infty$

○ 0.69
□ 1.36
◇ 2.70
△ 7.04

x/l
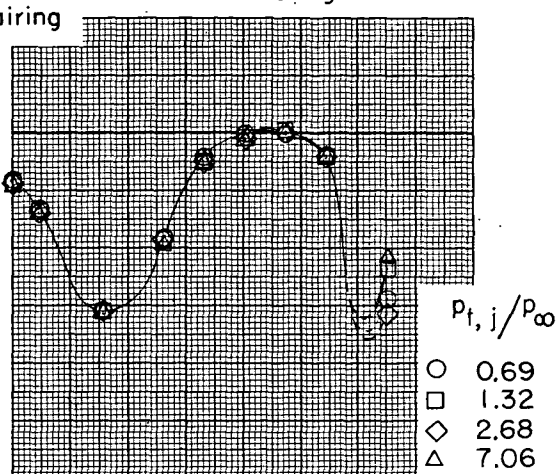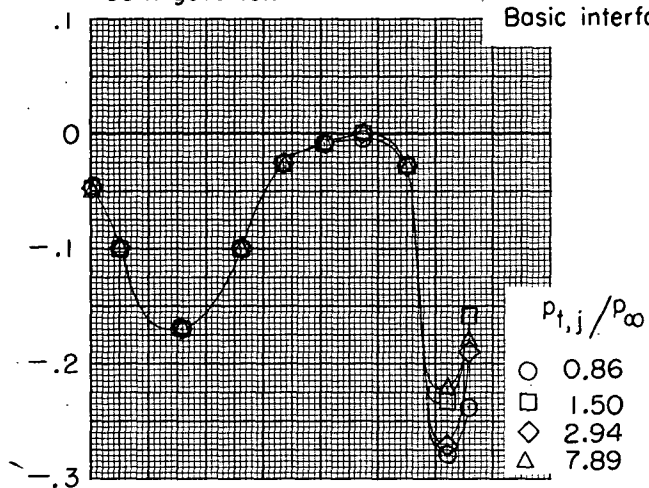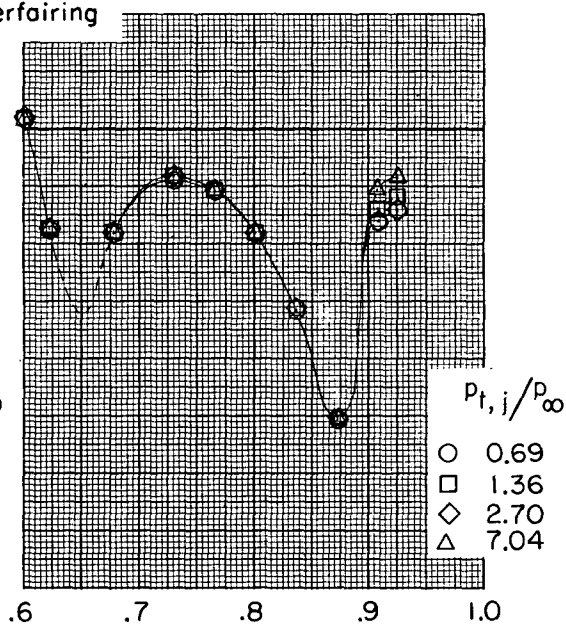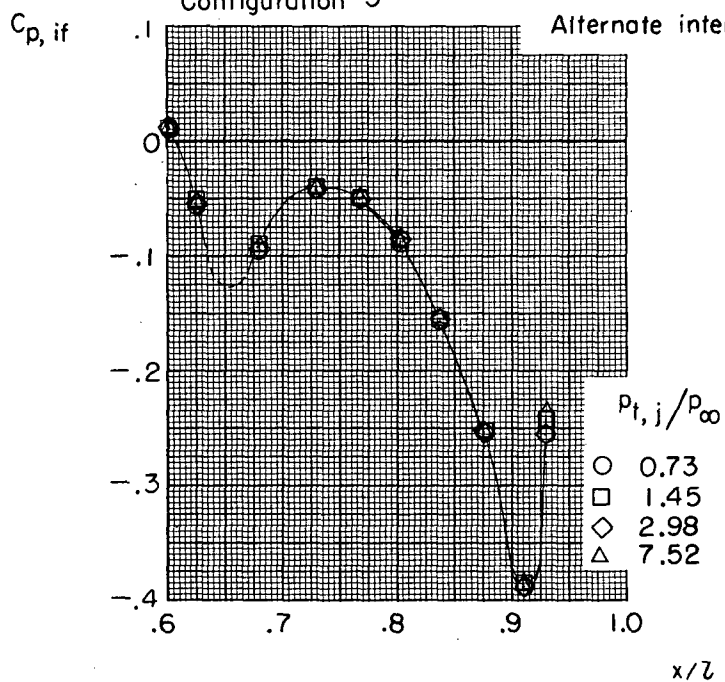
(g)   M = 1.30.

Figure 11.- Concluded.

Cruise nozzles
Configuration 5

Afterburning nozzles
Configuration 6

Basic interfairing

$p_{t,j}/p_\infty$

○ 1.03
□ 1.61
◇ 3.03
△ 4.95

$p_{t,j}/p_\infty$

○ 0.85
□ 1.46
◇ 2.69
△ 3.89

$C_{p,if}$

Configuration 7

Alternate interfairing

Configuration 8

$p_{t,j}/p_\infty$

○ 1.03
□ 1.61
◇ 3.01
△ 4.97

$p_{t,j}/p_\infty$

○ 0.85
□ 1.43
◇ 2.67
△ 3.92

x/l
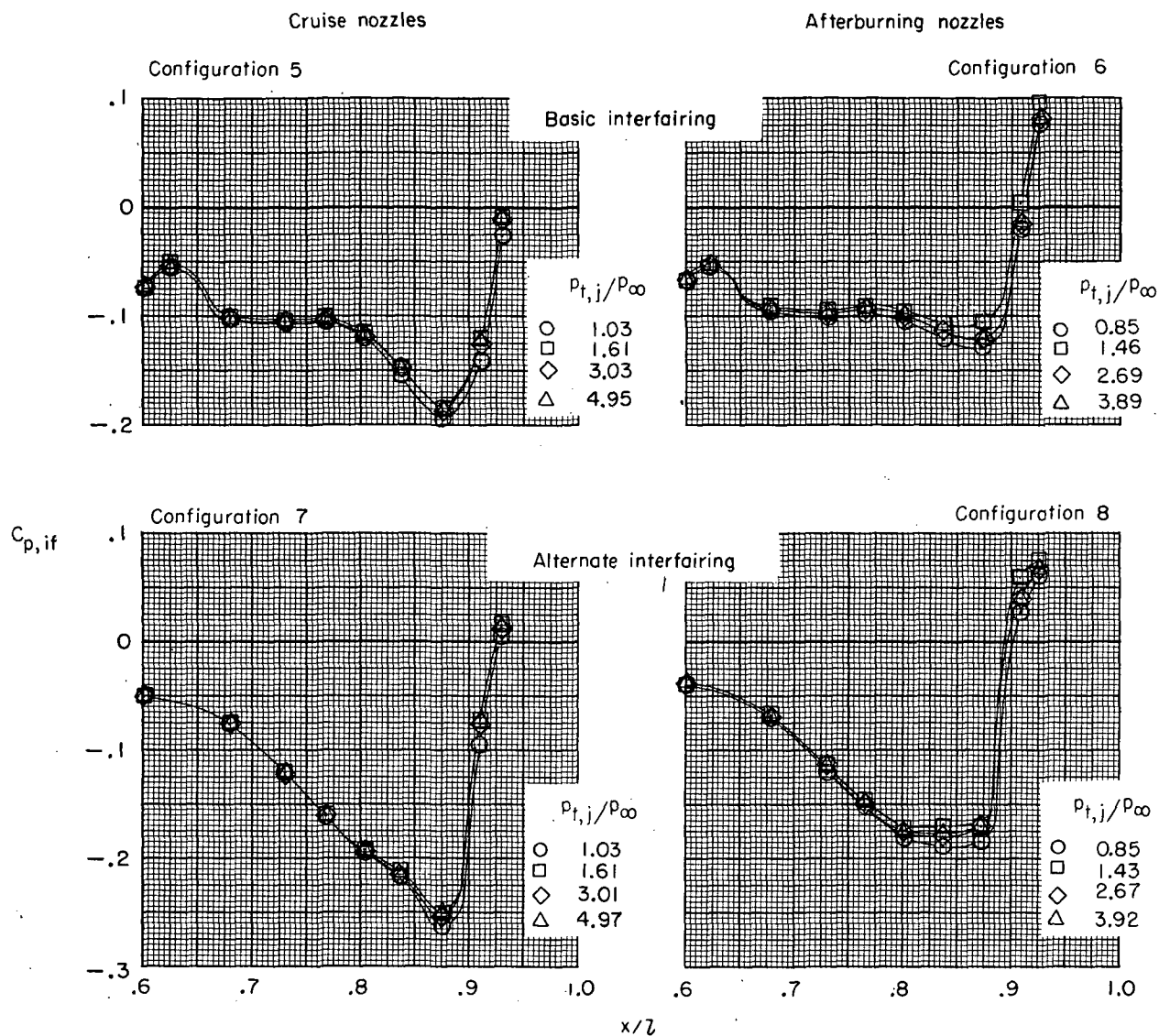
(a)   M = 0.60.

Figure 12.- Effect of jet operation on the interfairing pressure distributions (row 1)
for the wide-spaced-afterbody configurations at transonic Mach numbers.

(b)   M = 0.70.

Figure 12.- Continued.

Cruise nozzles

Configuration 5

Basic interfairing

Afterburning nozzles

Configuration 6

$p_{t,j}/p_\infty$	
O	1.05
□	1.62
◇	3.02
△	5.93

$p_{t,j}/p_\infty$	
O	0.83
□	1.45
◇	2.69
△	4.68

$C_{p,if}$

Configuration 7

Alternate interfairing

Configuration 8

$p_{t,j}/p_\infty$	
O	1.05
□	1.64
◇	3.02
△	5.96

$p_{t,j}/p_\infty$	
O	0.83
□	1.46
◇	2.68
△	4.65

x/l

(c)   M = 0.80.

Figure 12.- Continued.

Cruise nozzles

Configuration 5

Afterburning nozzles

Configuration 6

Basic interfairing

$p_{t,j}/p_\infty$

○	1.06
□	1.54
◇	3.04
△	5.93

$p_{t,j}/p_\infty$

○	0.82
□	1.36
◇	2.72
△	5.26

$C_{p,if}$

Configuration 7

Configuration 8

Alternate interfairing

$p_{t,j}/p_\infty$

○	1.06
□	1.62
◇	3.04
△	6.00

$p_{t,j}/p_\infty$

○	0.82
□	1.37
◇	2.71
△	5.28

x/l

(d) $M = 0.90$.

Figure 12.- Continued.

Cruise nozzles

Afterburning nozzles

Configuration 5

Configuration 6
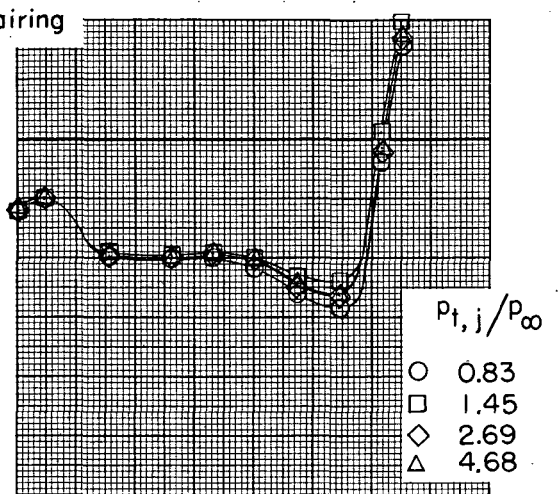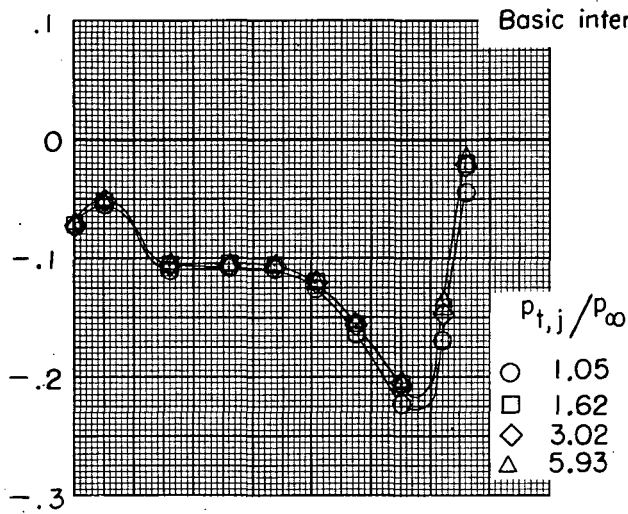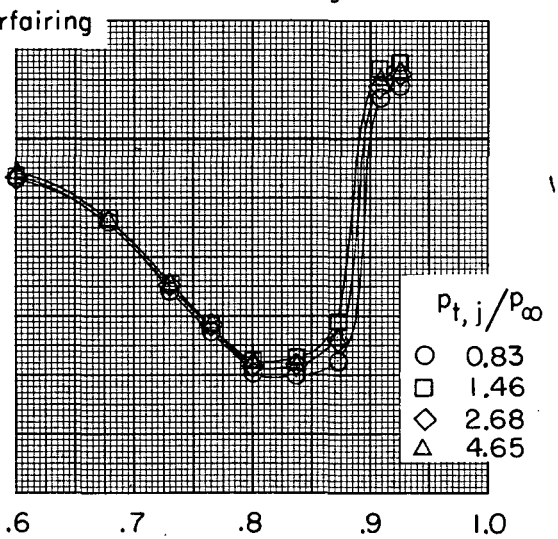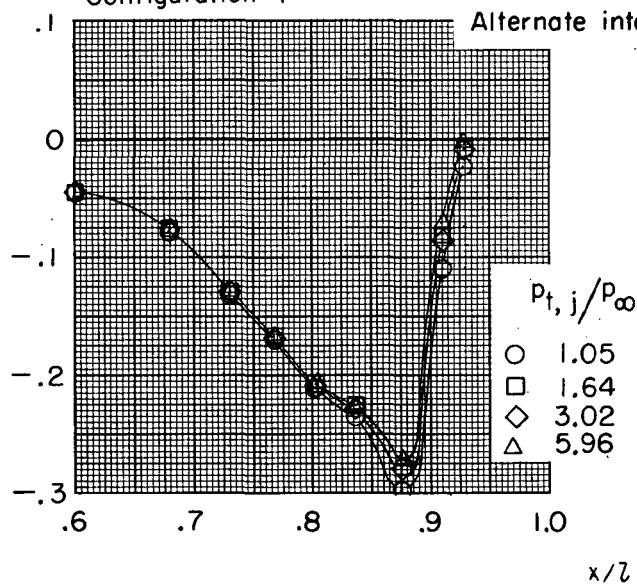
Basic interfairing

$p_{t,j}/p_\infty$

○ 1.02
□ 1.66
◇ 3.02
△ 5.95

$p_{t,j}/p_\infty$

○ 0.81
□ 1.48
◇ 2.71
△ 5.28

$C_{p,if}$

Configuration 7

Configuration 8

Alternate interfairing

$p_{t,j}/p_\infty$

○ 1.04
□ 1.69
◇ 3.05
△ 5.96

$p_{t,j}/p_\infty$

○ 0.82
□ 1.46
◇ 2.69
△ 5.34

x/l

(e)   M = 0.95.

Figure 12.- Continued.

Cruise nozzles

Afterburning nozzles

Configuration 5

Basic interfairing

Configuration 6

$p_{t,j}/p_\infty$

○ 0.87
□ 1.55
◇ 3.08
△ 8.03

$p_{t,j}/p_\infty$

○ 0.73
□ 1.39
◇ 2.75
△ 7.12

Configuration 7

Alternate interfairing

Configuration 8

$C_{p,if}$

$p_{t,j}/p_\infty$

○ 0.88
□ 1.49
◇ 3.05
△ 8.03

$p_{t,j}/p_\infty$

○ 0.73
□ 1.36
◇ 2.74
△ 7.11

x/l

(f)   M = 1.20.

Figure 12.- Continued.

55

Cruise nozzles

Afterburning nozzles

Configuration 5

Basic interfairing

Configuration 6

$p_{t,j}/p_\infty$

○ 0.84
□ 1.65
◇ 3.04
△ 7.96

$p_{t,j}/p_\infty$

○ 0.69
□ 1.39
◇ 2.74
△ 7.08

$C_{p,if}$

Configuration 7

Alternate interfairing

Configuration 8

$p_{t,j}/p_\infty$

○ 0.85
□ 1.54
◇ 3.04
△ 7.95

$p_{t,j}/p_\infty$

○ 0.69
□ 1.39
◇ 2.69
△ 7.10

x/l
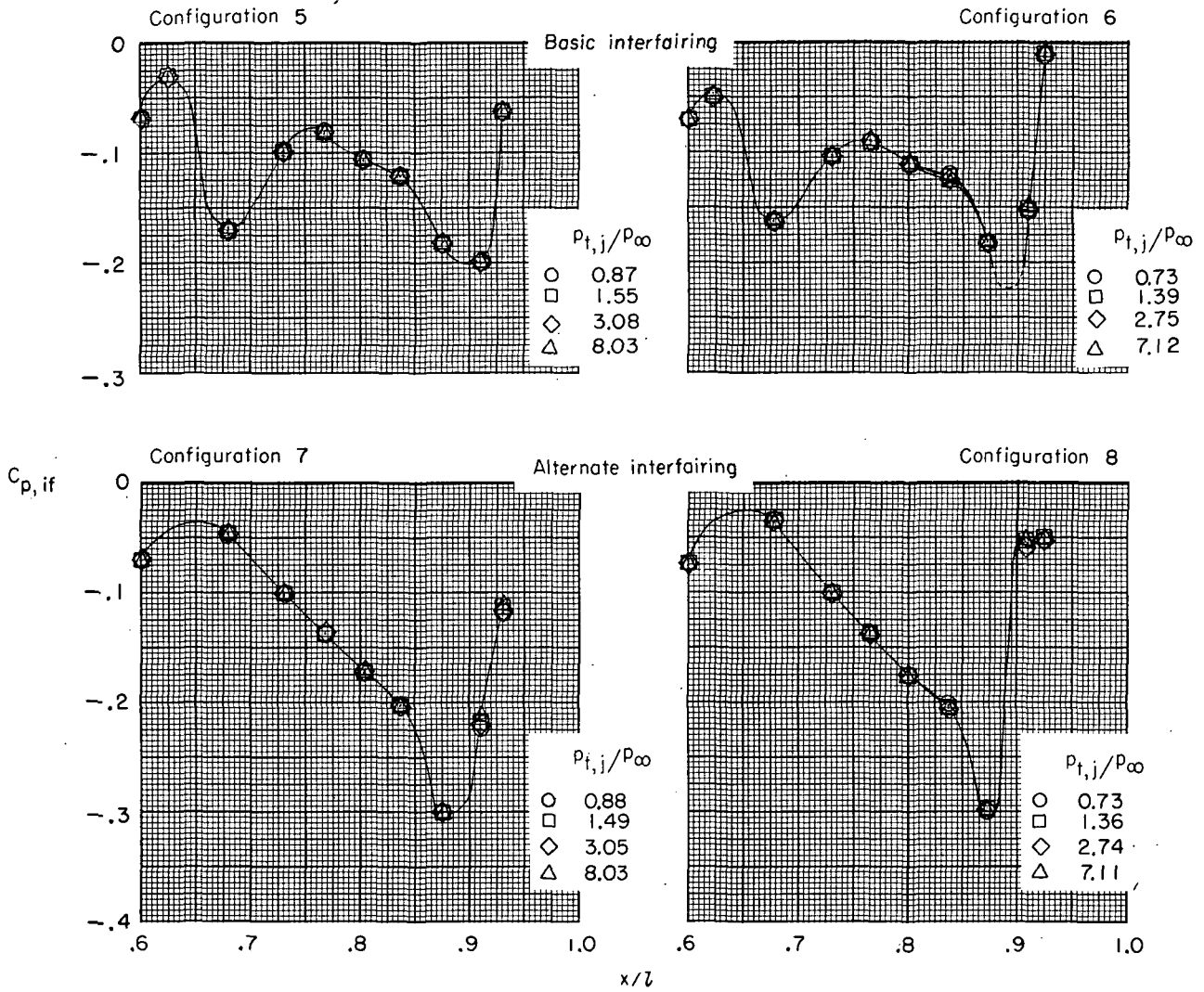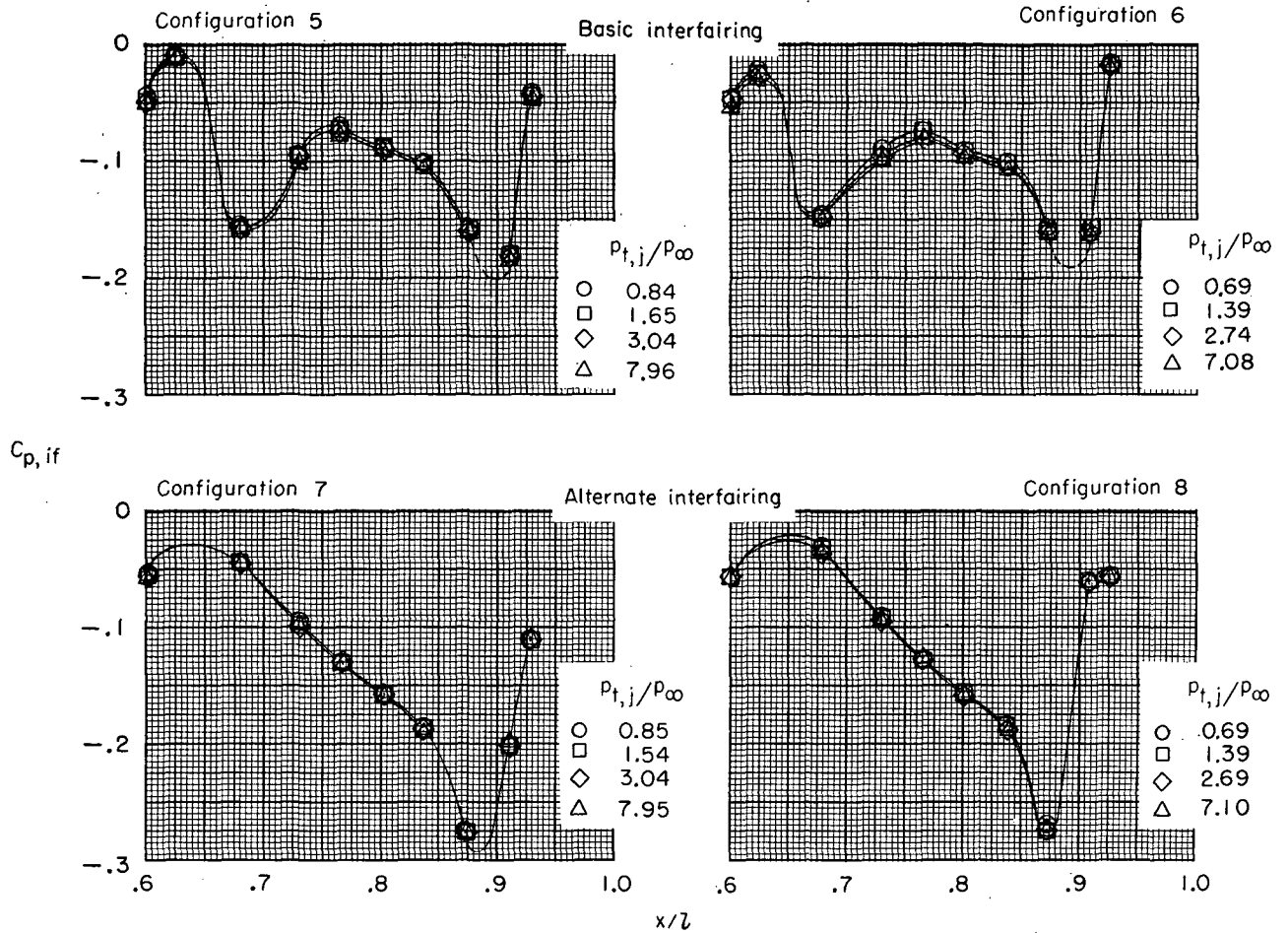
(g)   M = 1.30.

Figure 12.- Concluded.
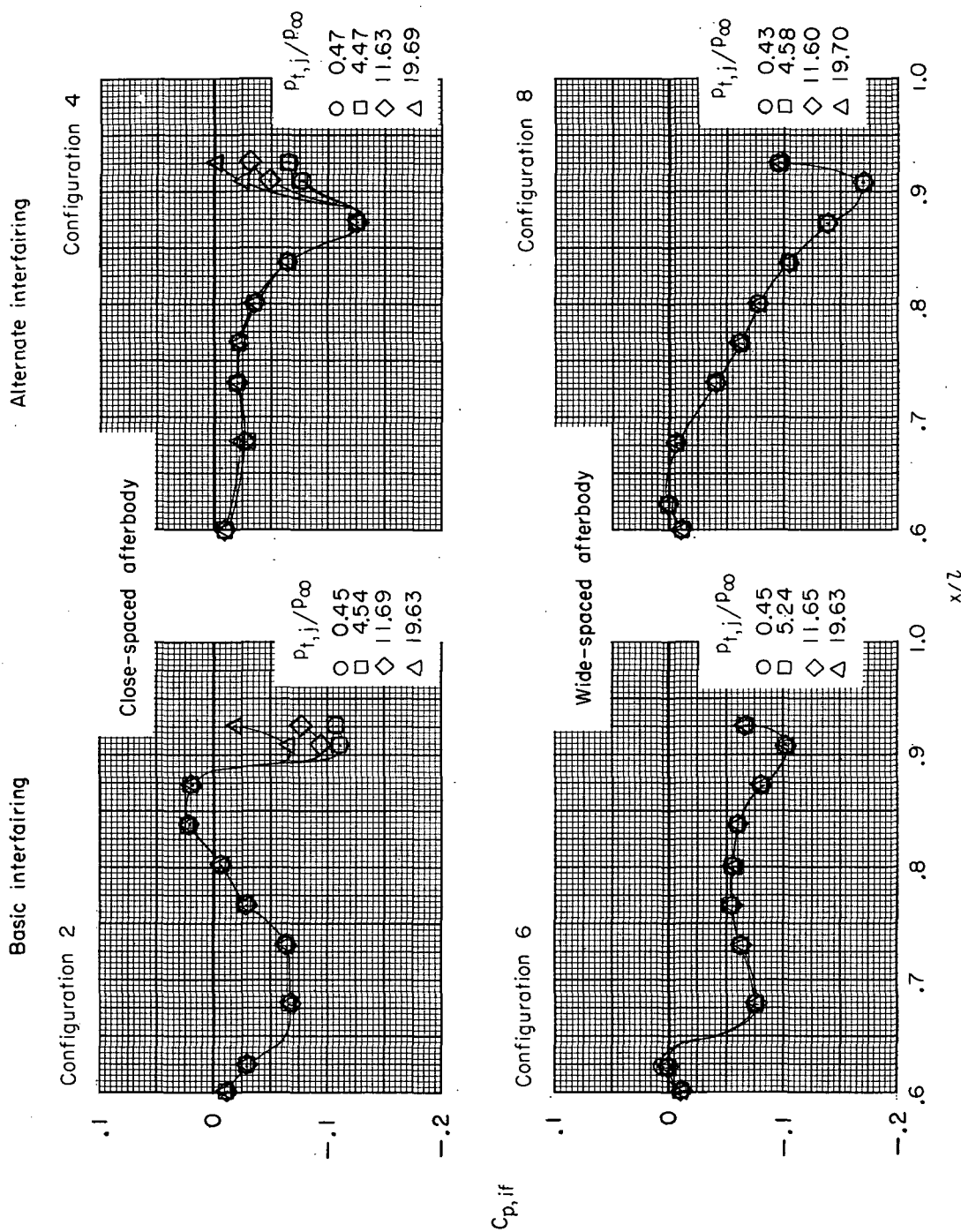
Figure 13.- Effect of jet operation on the interfairing pressure distributions (row 1) for the afterburning-nozzle configurations at M = 2.20.

(a) M = 0.60.
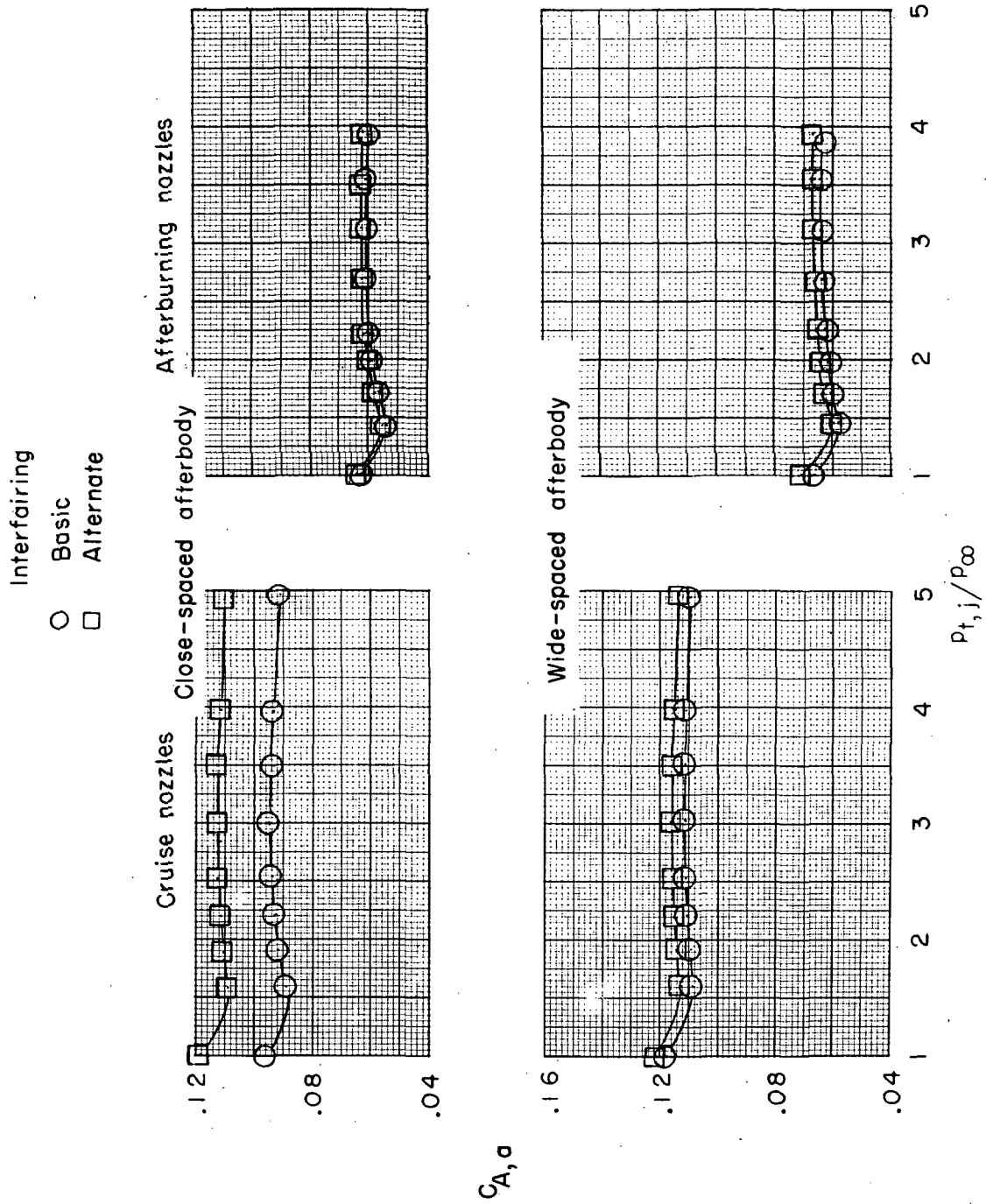
Figure 14.- Variation of afterbody axial-force coefficient with jet-total-pressure ratio.

(b) $M = 0.70$.

Figure 14.- Continued.

59
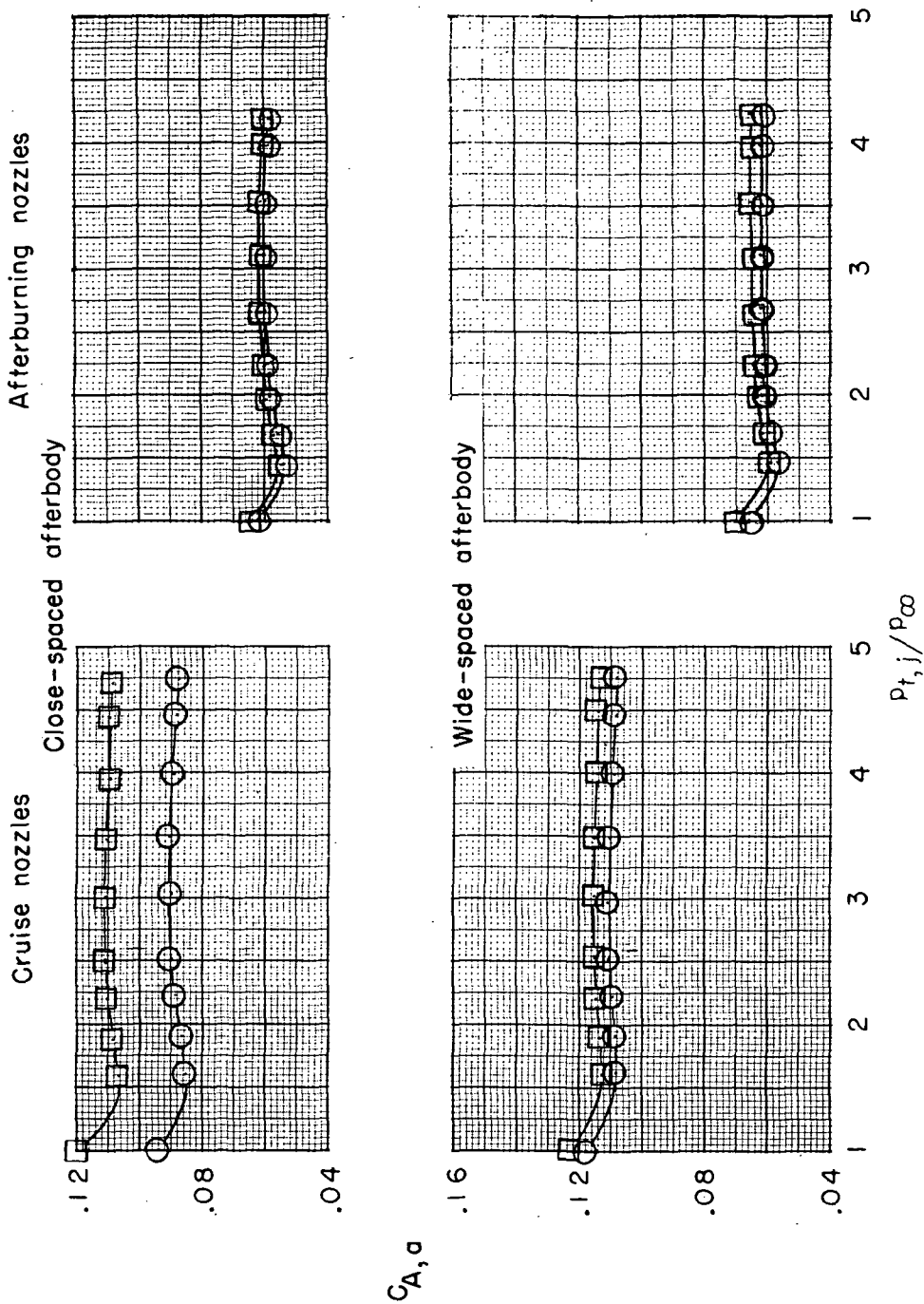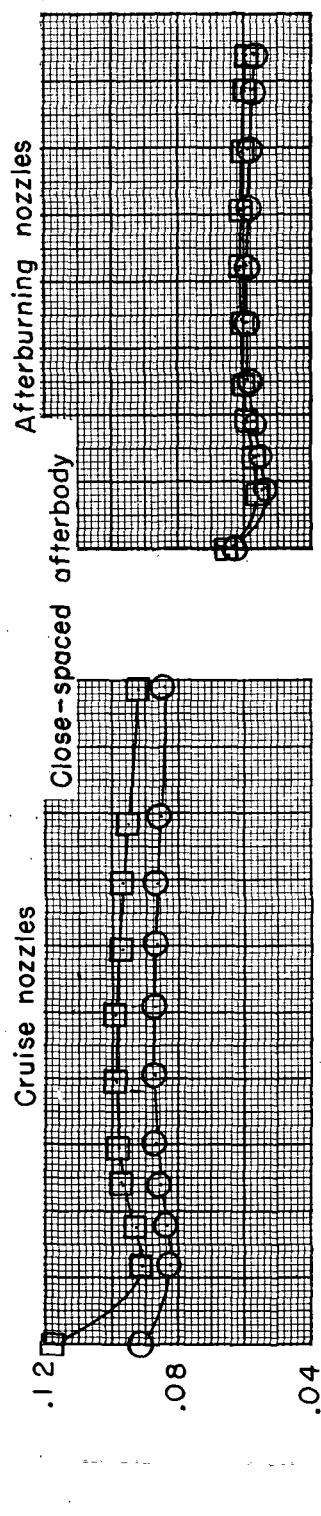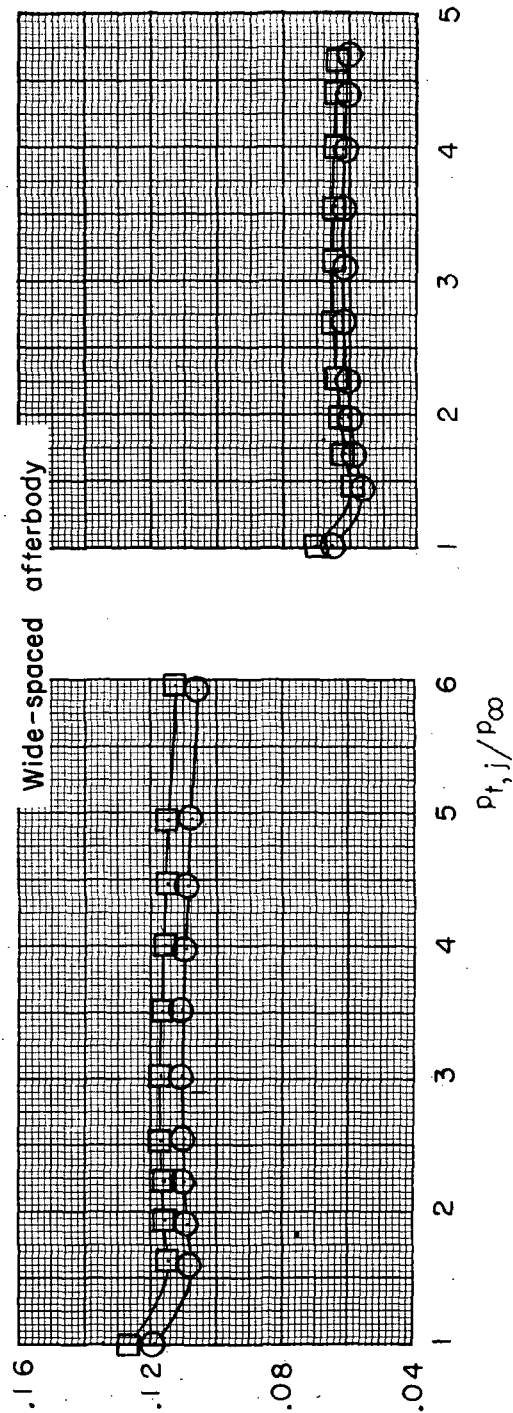
(c) M = 0.80.

Figure 14. - Continued.

60

(d) M = 0.90.

Figure 14.- Continued.

61

Interfairing

○ Basic
□ Alternate

Cruise nozzles

Close-spaced afterbody

Afterburning nozzles

Wide-spaced afterbody

$C_{A,a}$
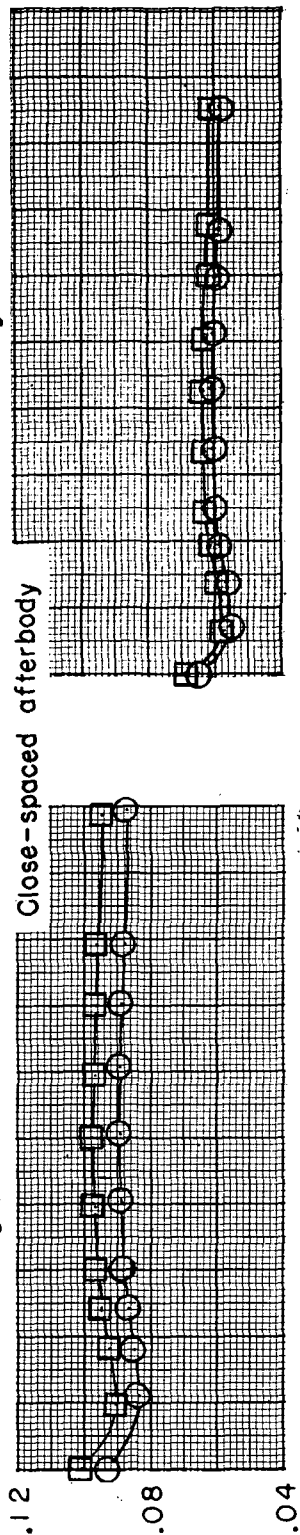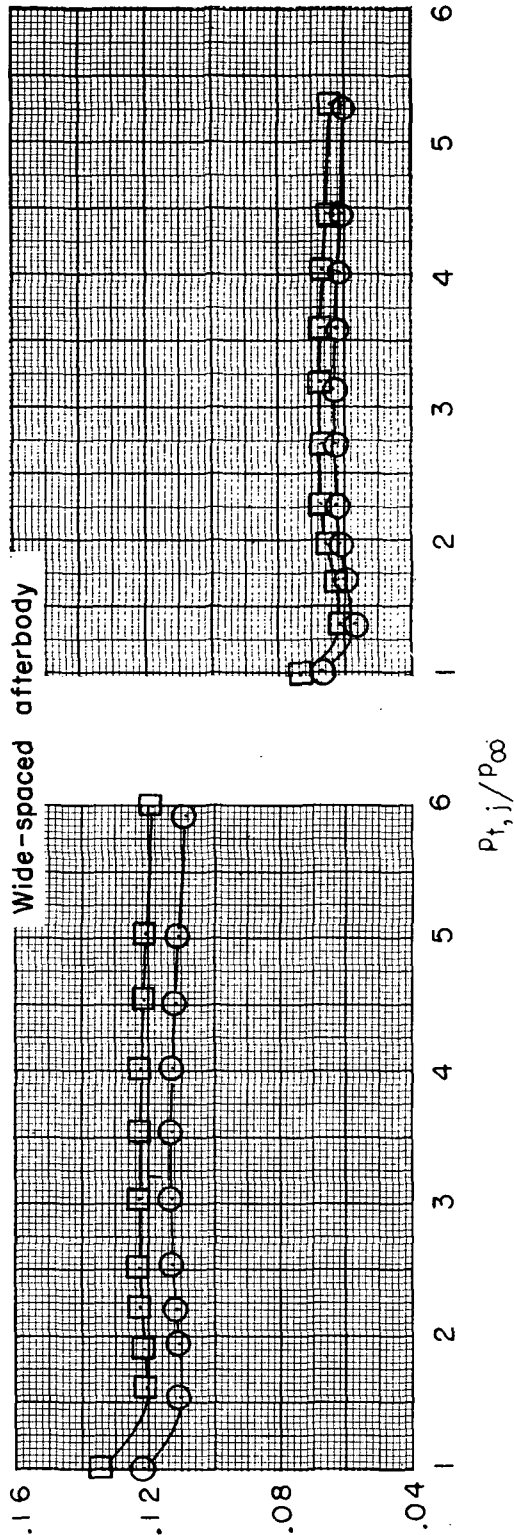
$p_{t,j}/p_\infty$
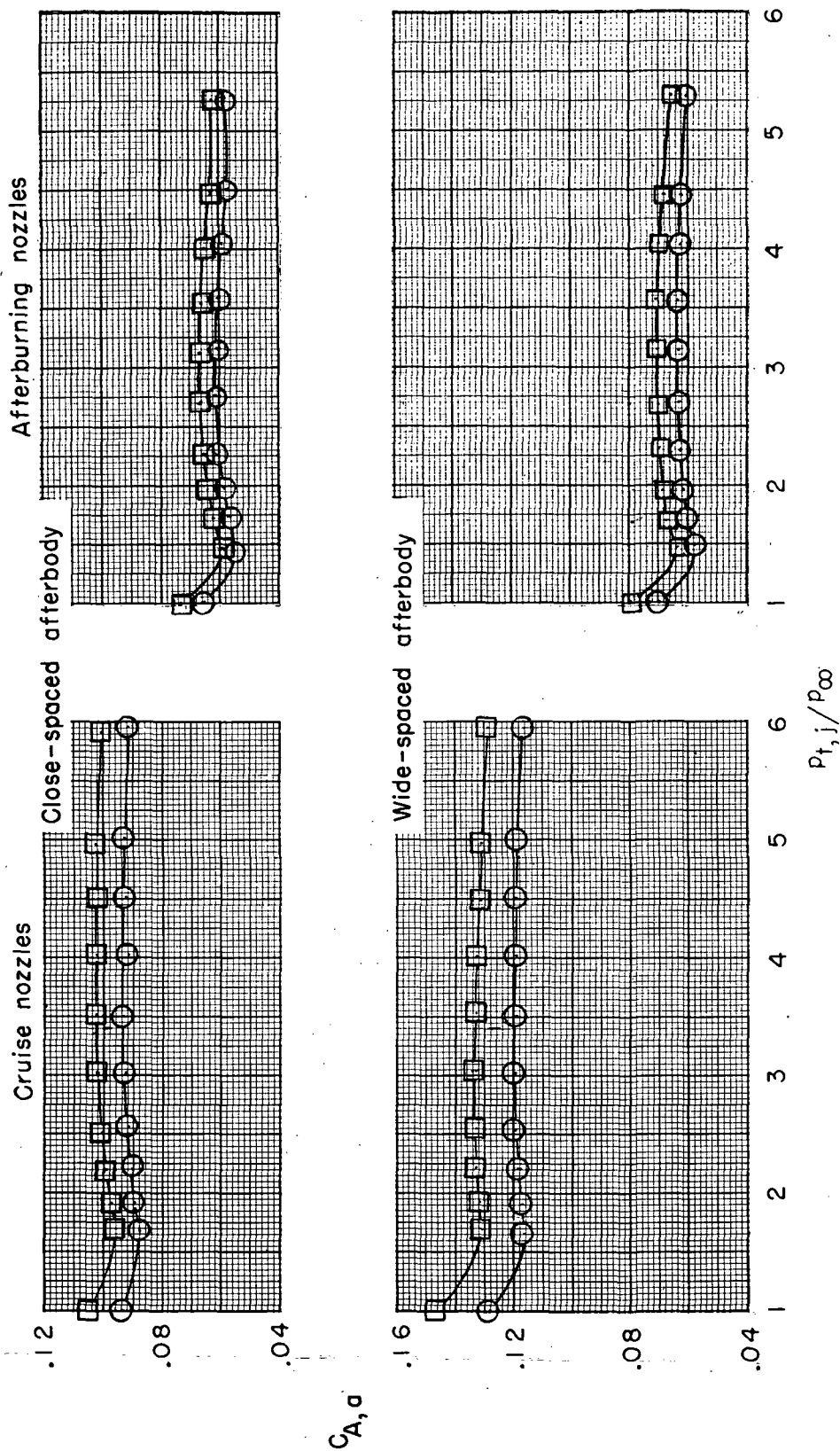
(e) $M = 0.95$.

Figure 14.- Continued.

(f) $M = 1.20$.

Figure 14. – Continued.

Interfairing

○ Basic
□ Alternate

Cruise nozzles   Close-spaced afterbody

Afterburning nozzles

Wide-spaced afterbody

$C_{A,a}$

$p_{t,j}/p_\infty$
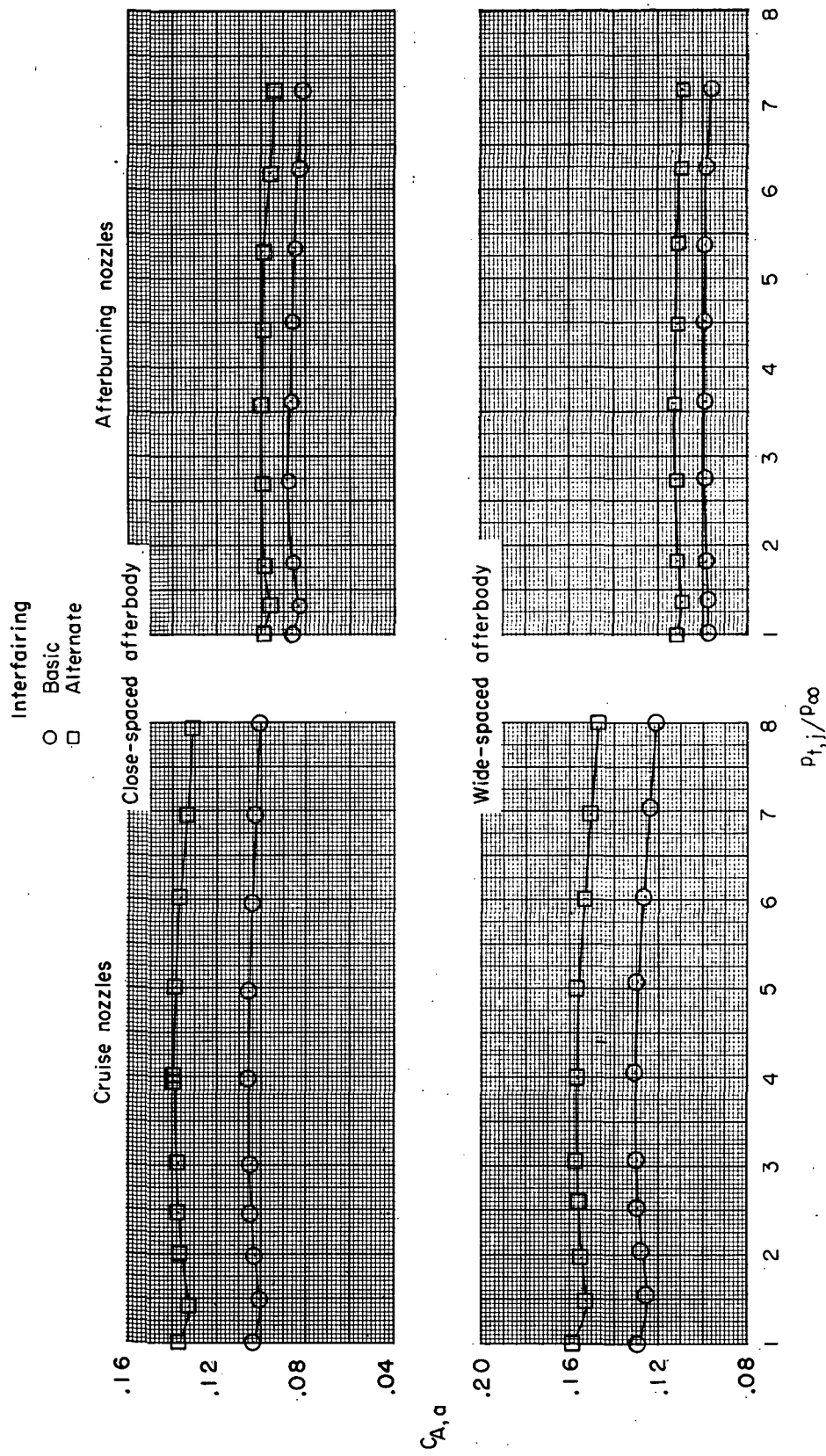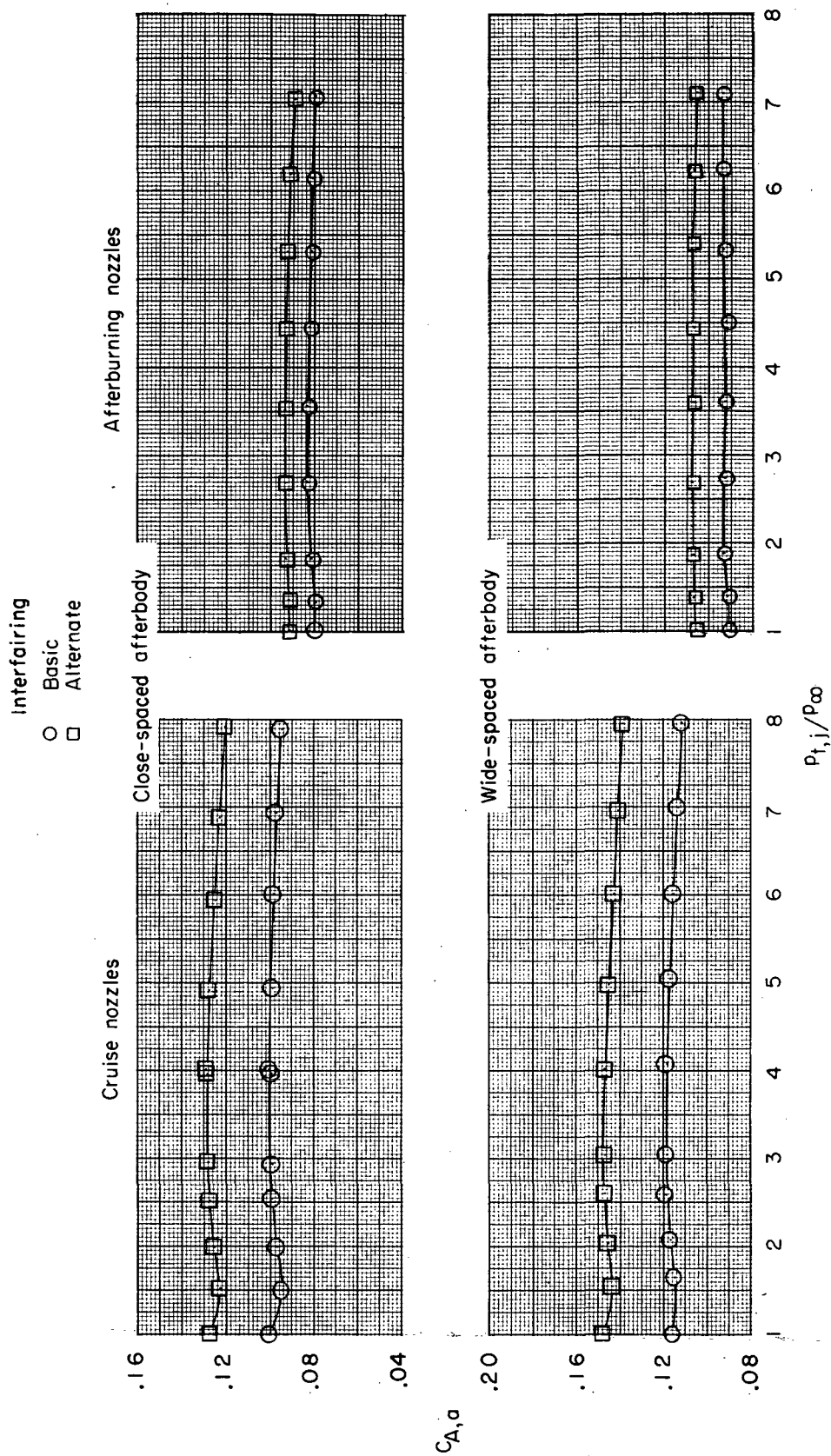
(g) M = 1.30.

Figure 14.- Continued.

Interfairing
○   Basic
□   Alternate

Afterburning nozzles
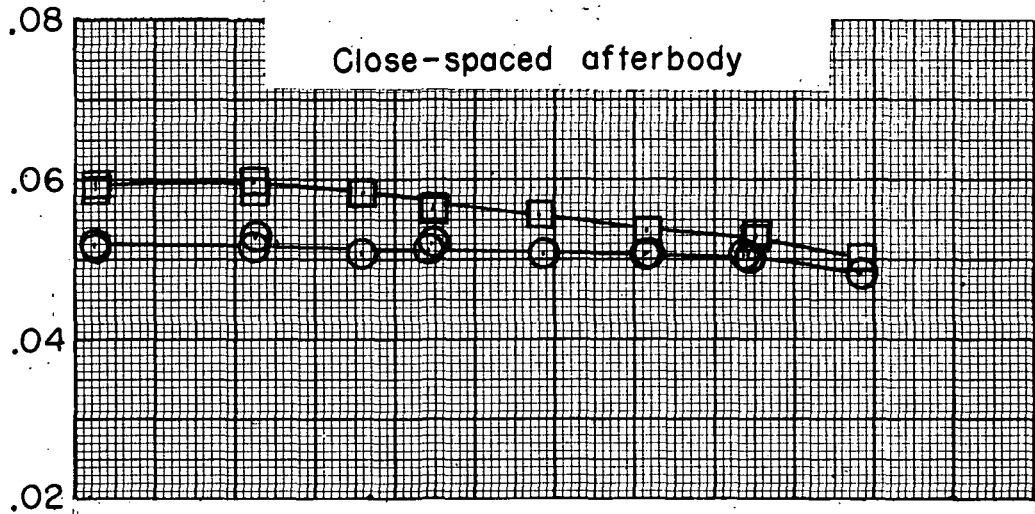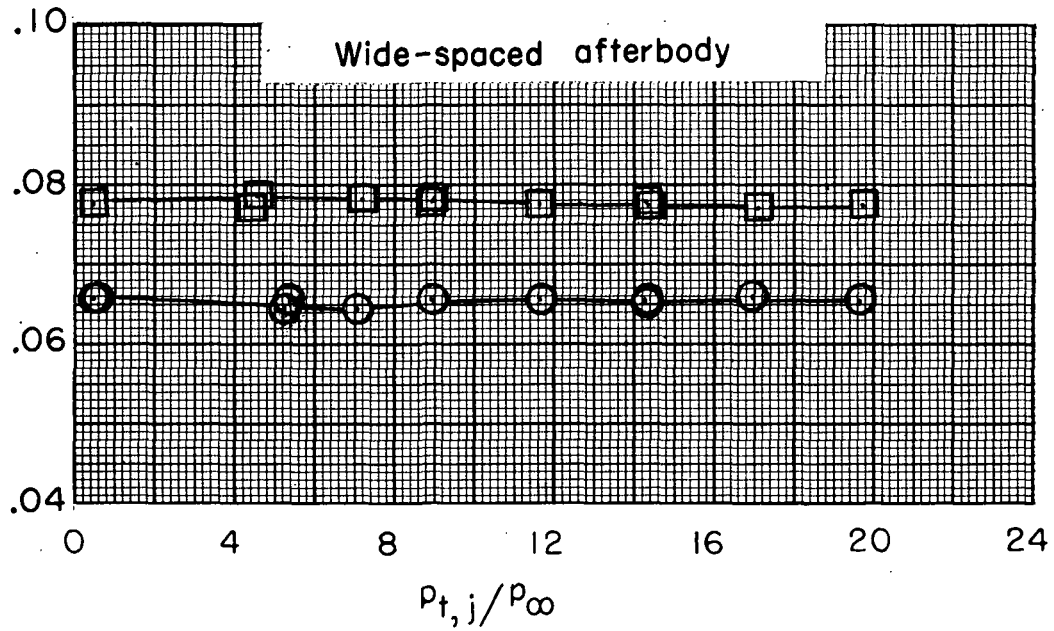
(h)   M = 2.20.

Figure 14.- Concluded.
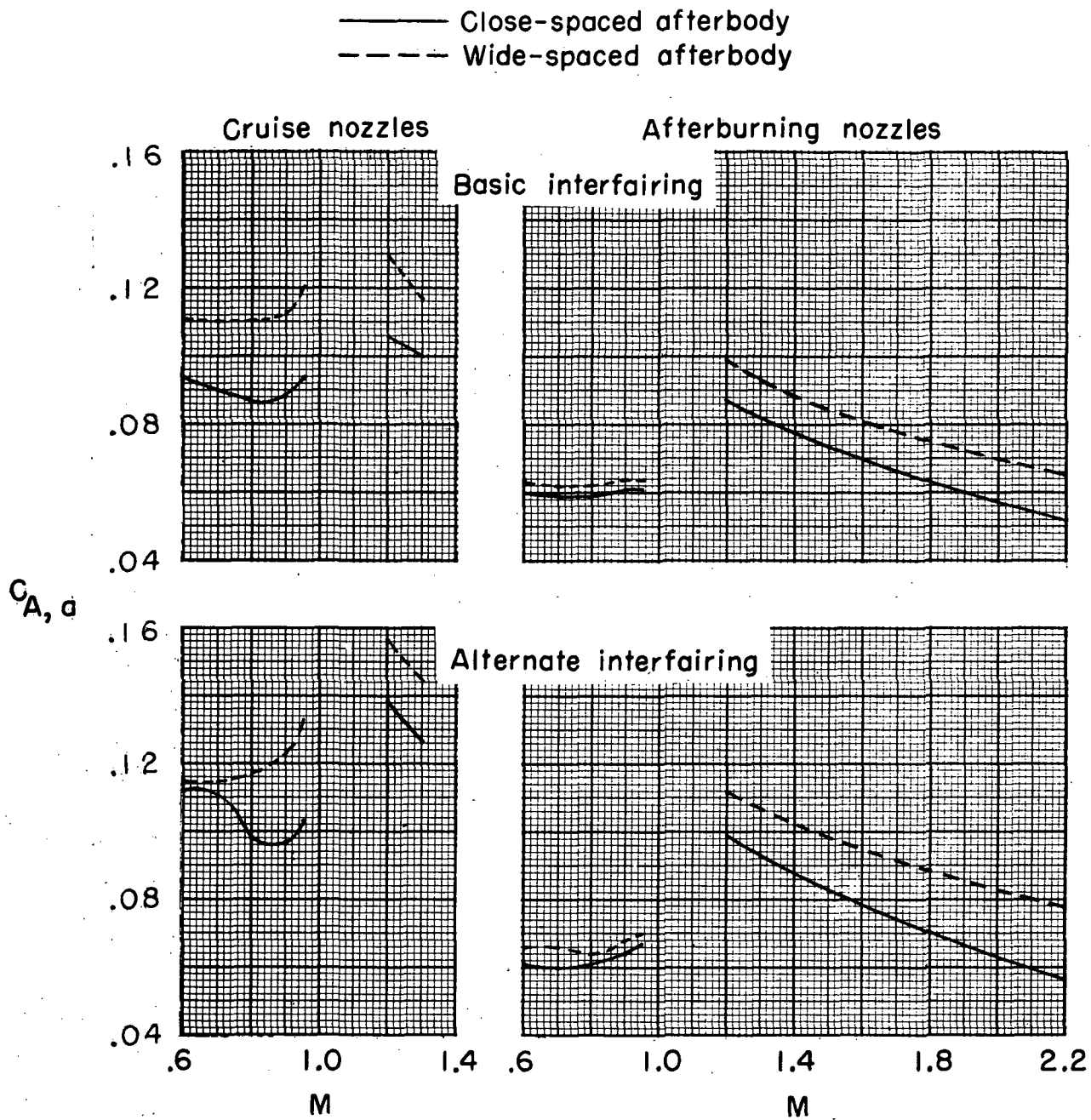
Figure 15.- Variation of afterbody axial-force coefficient with Mach number
at scheduled jet-total-pressure ratios.
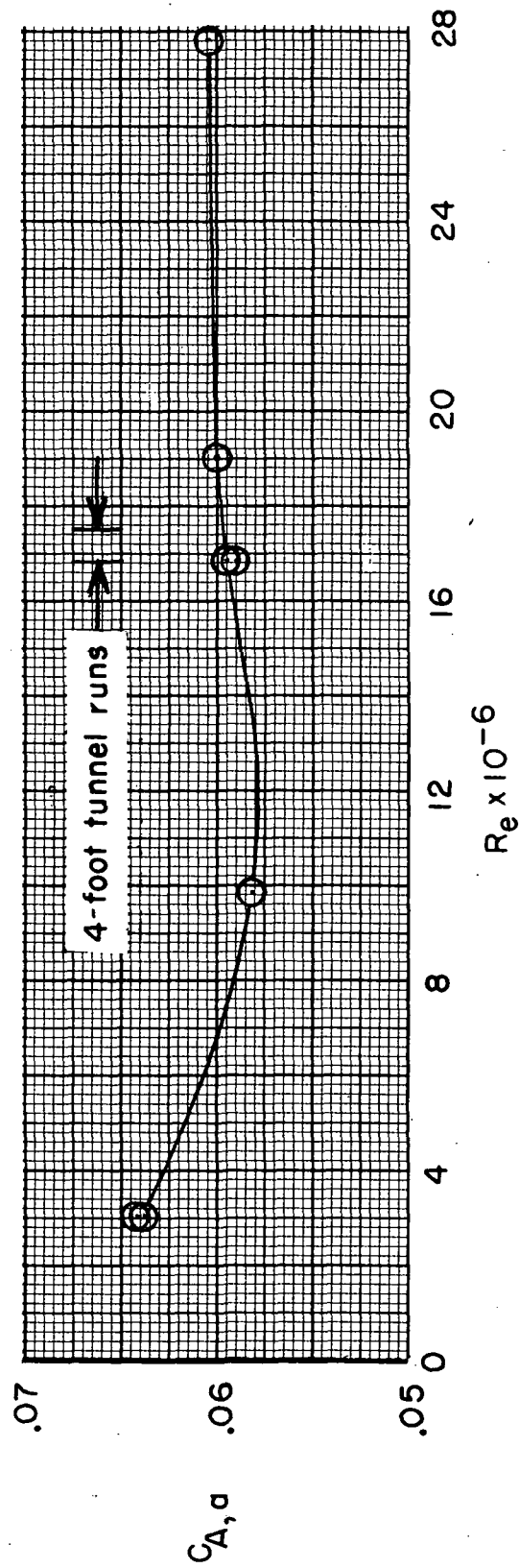
Figure 16.- Effect of Reynolds number variation on afterbody axial-force coefficient; configuration 4; M = 2.20; jet off.
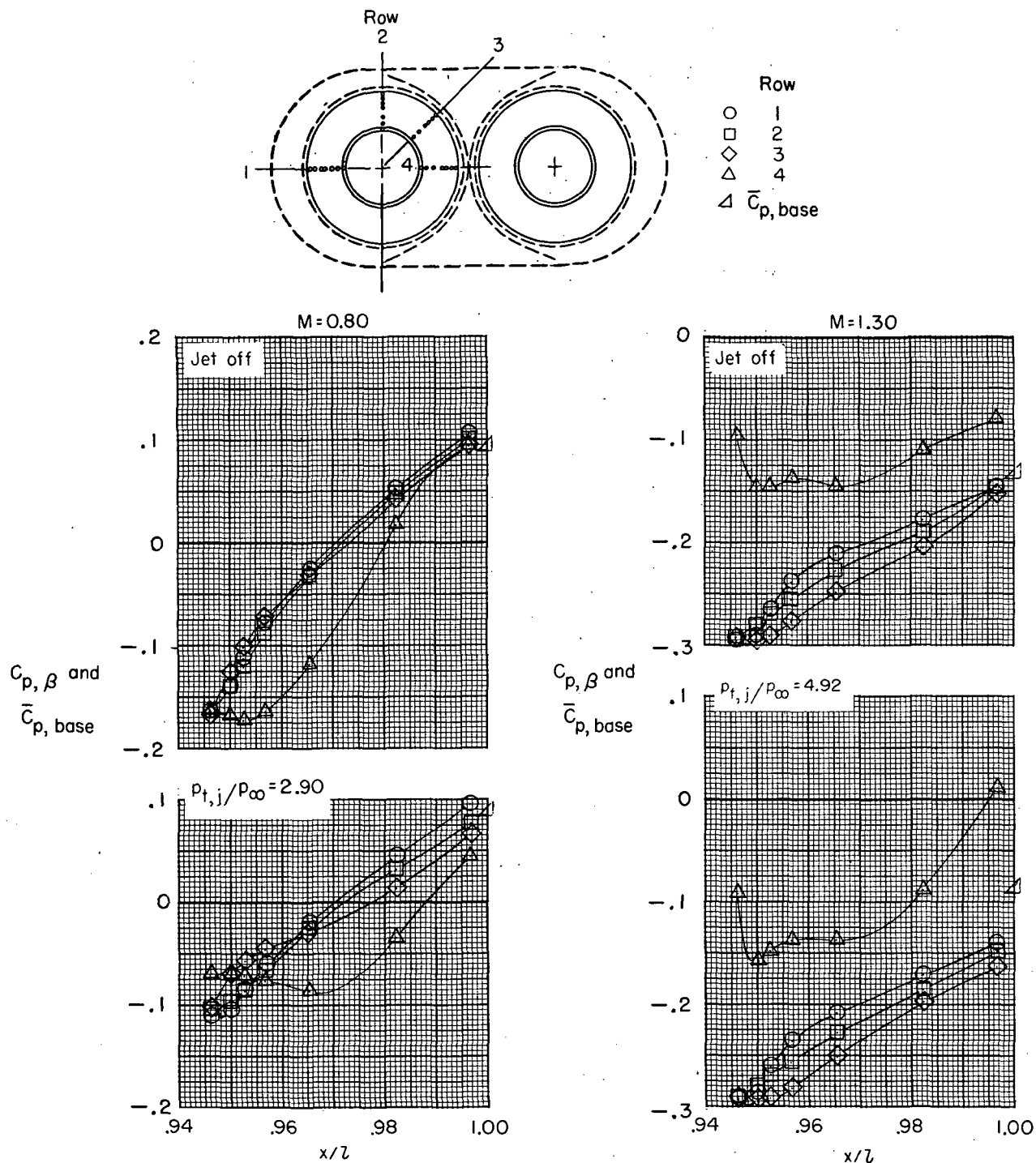
(a) Configuration 3.

Figure 17.- Typical examples of nozzle pressure distributions for several Mach numbers at jet off and scheduled jet-total-pressure ratios.
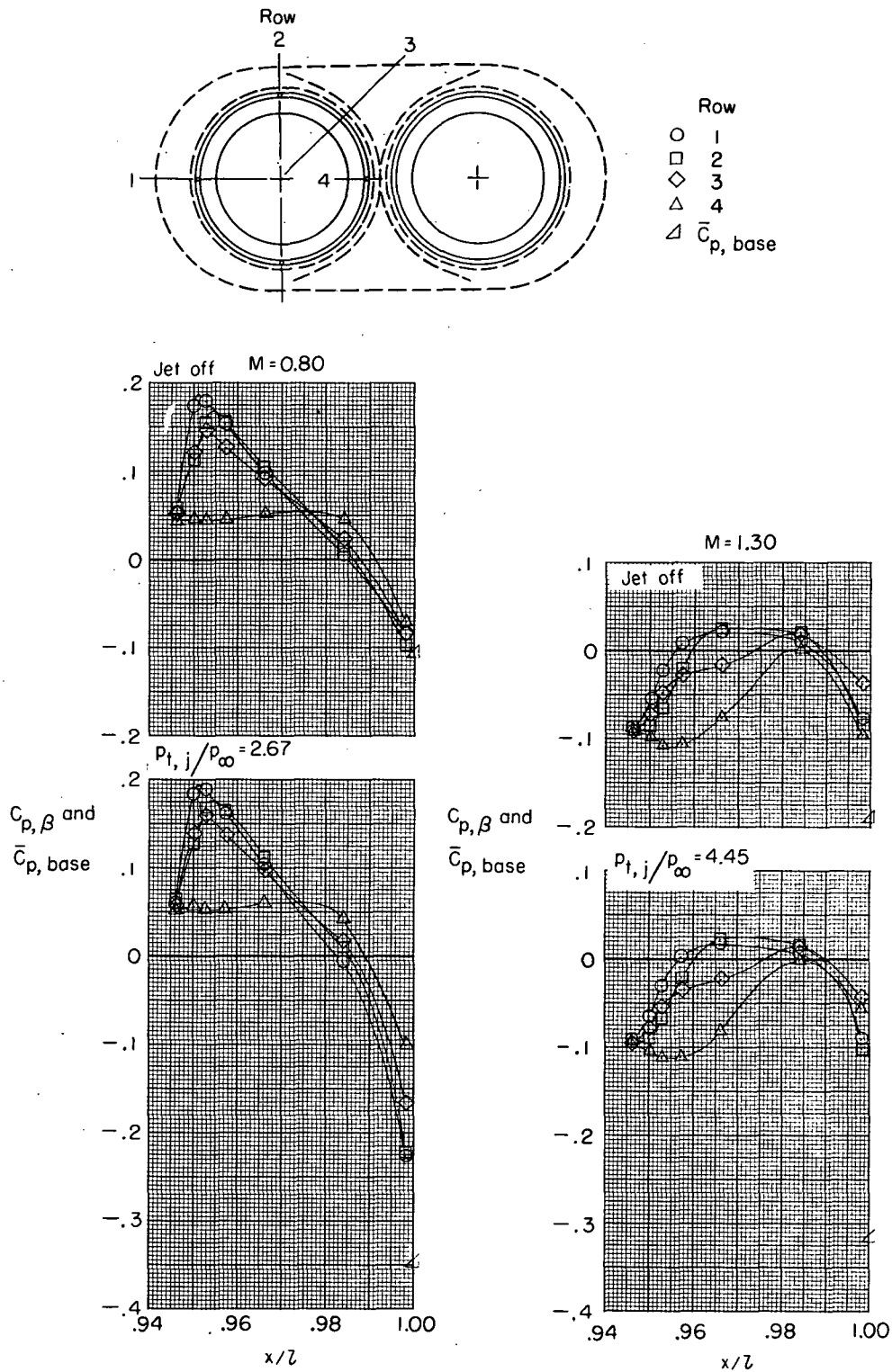
(b) Configuration 4.

Figure 17.– Continued.
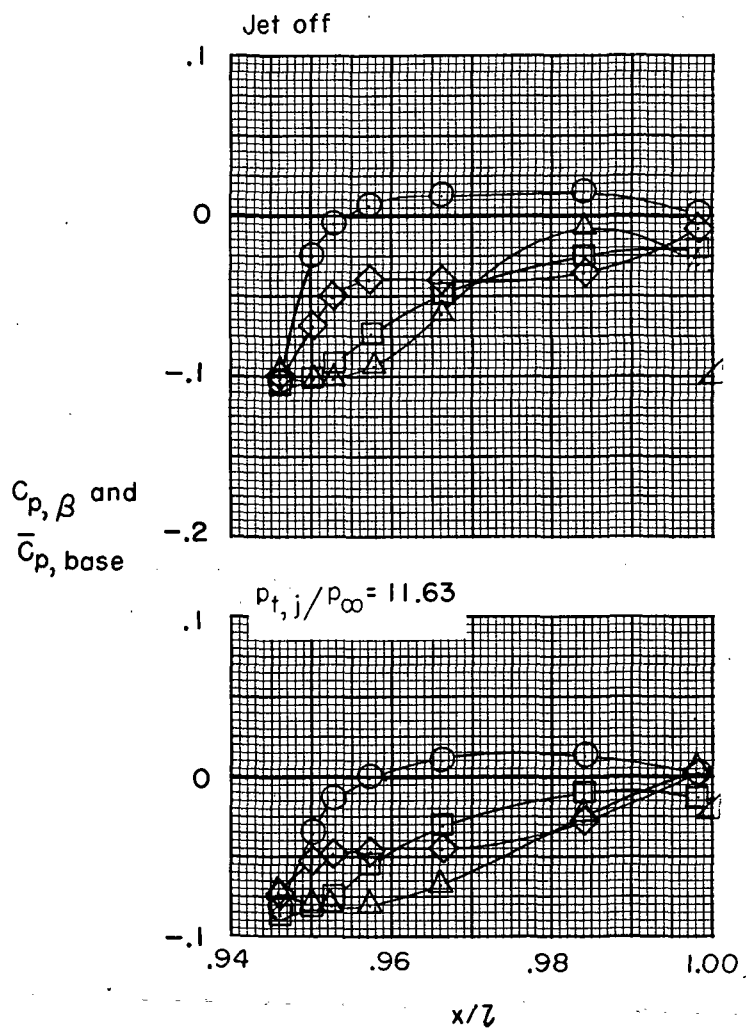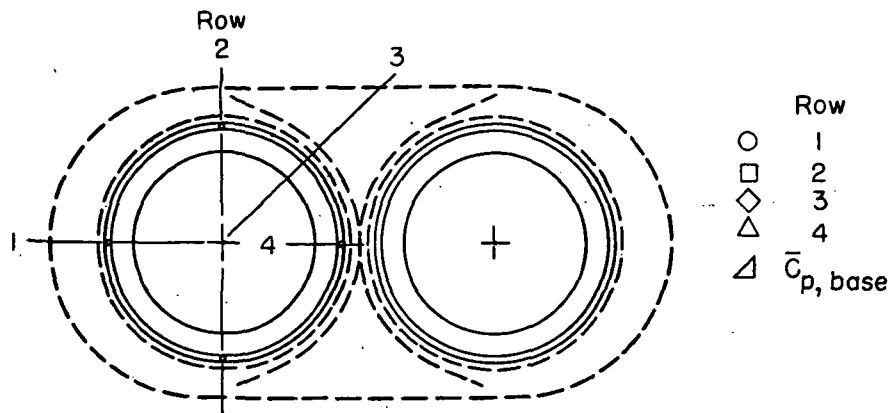
(c) Configuration 4;   M = 2.20.

Figure 17.- Continued.
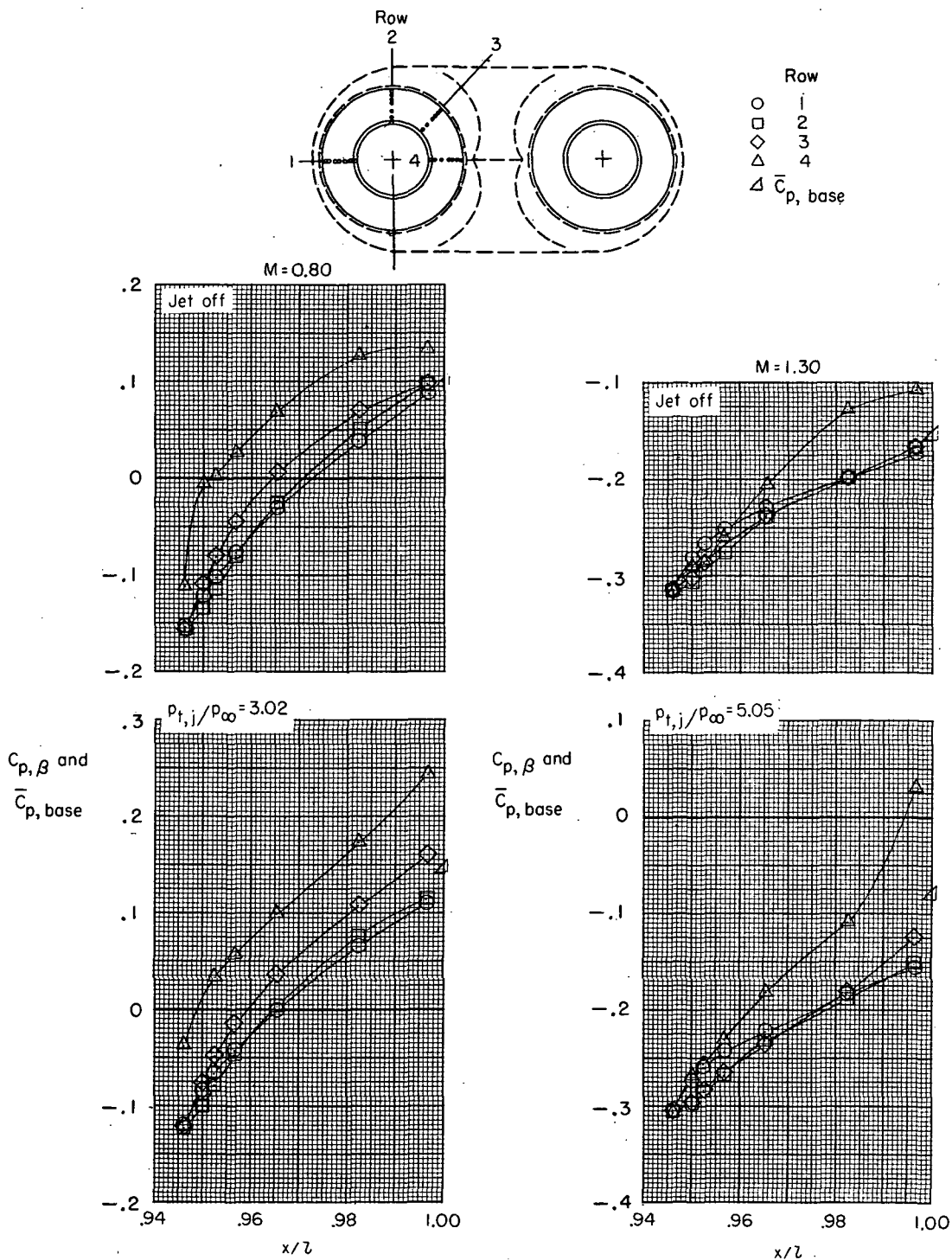
(d) Configuration 5.

Figure 17.- Continued.
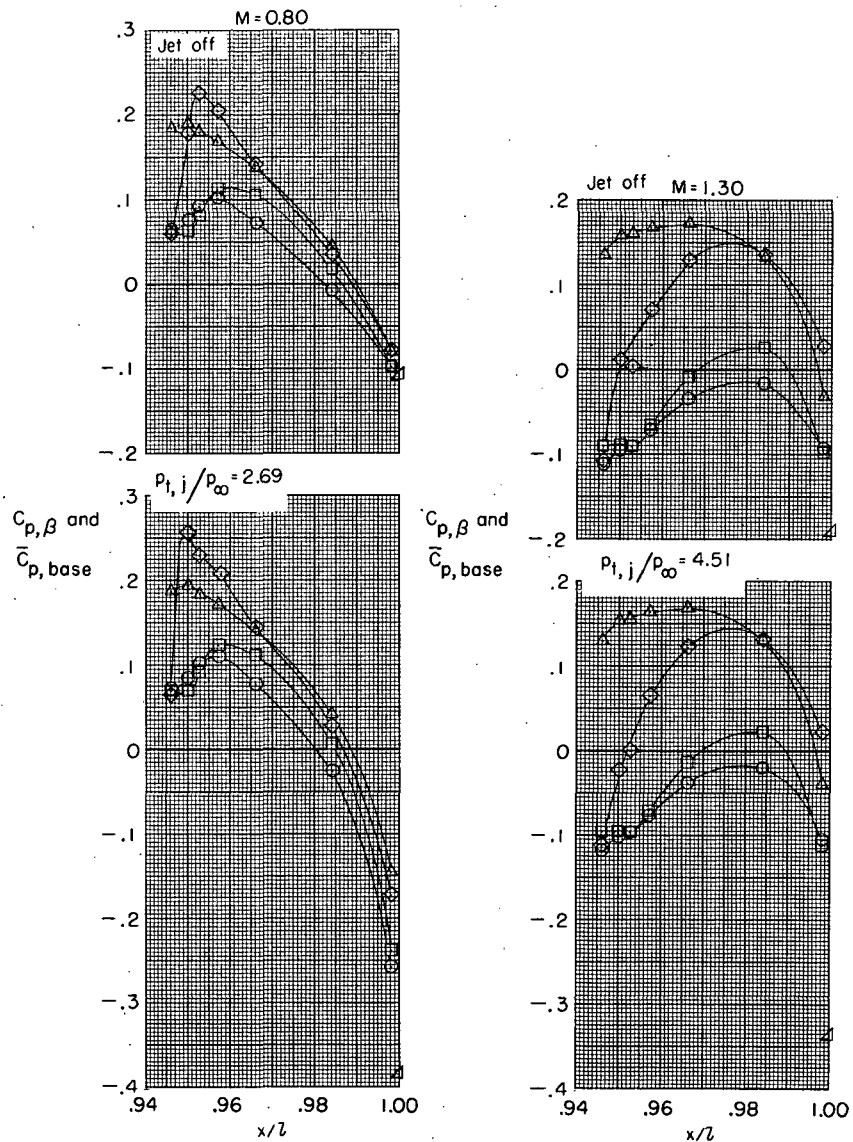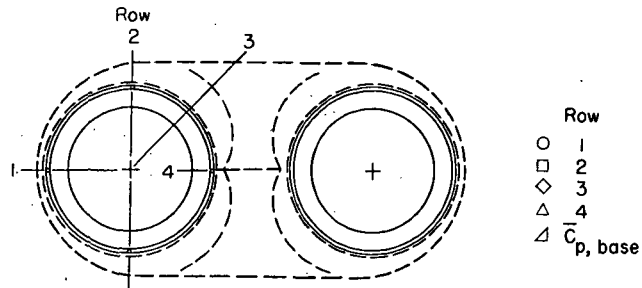
(e) Configuration 6.

Figure 17.- Continued.
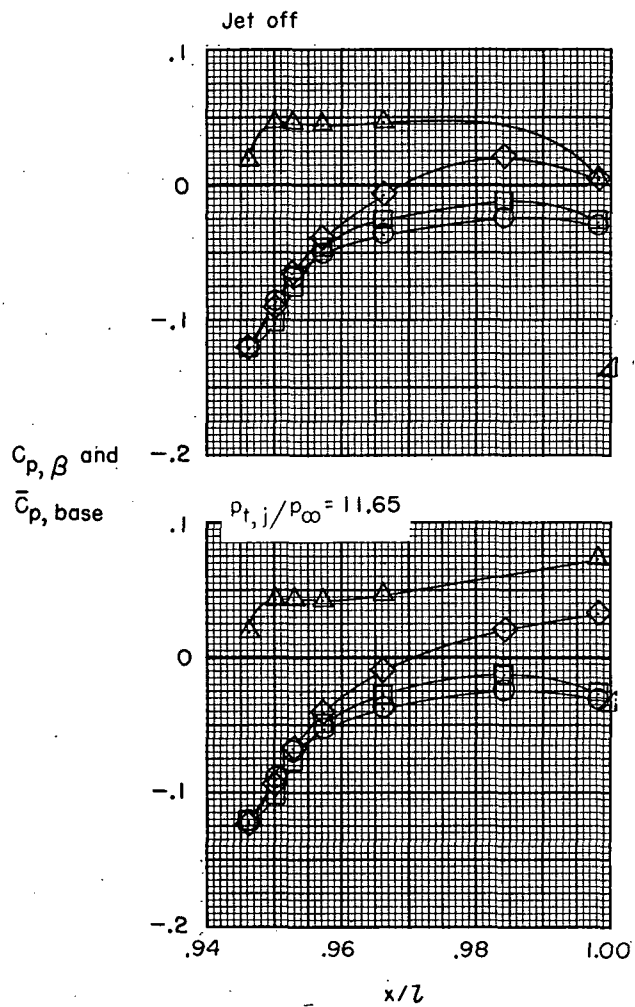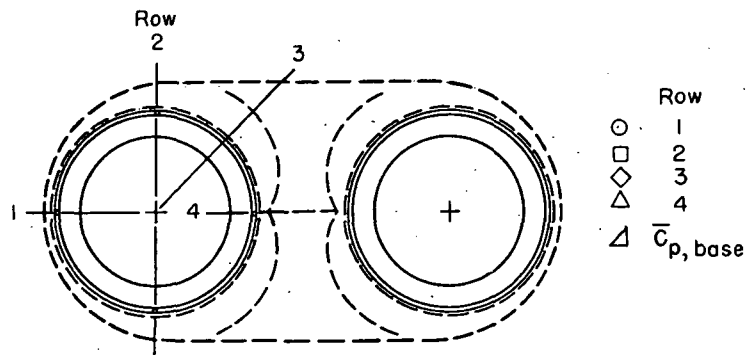
(f) Configuration 6;   M = 2.20.

Figure 17.- Concluded.
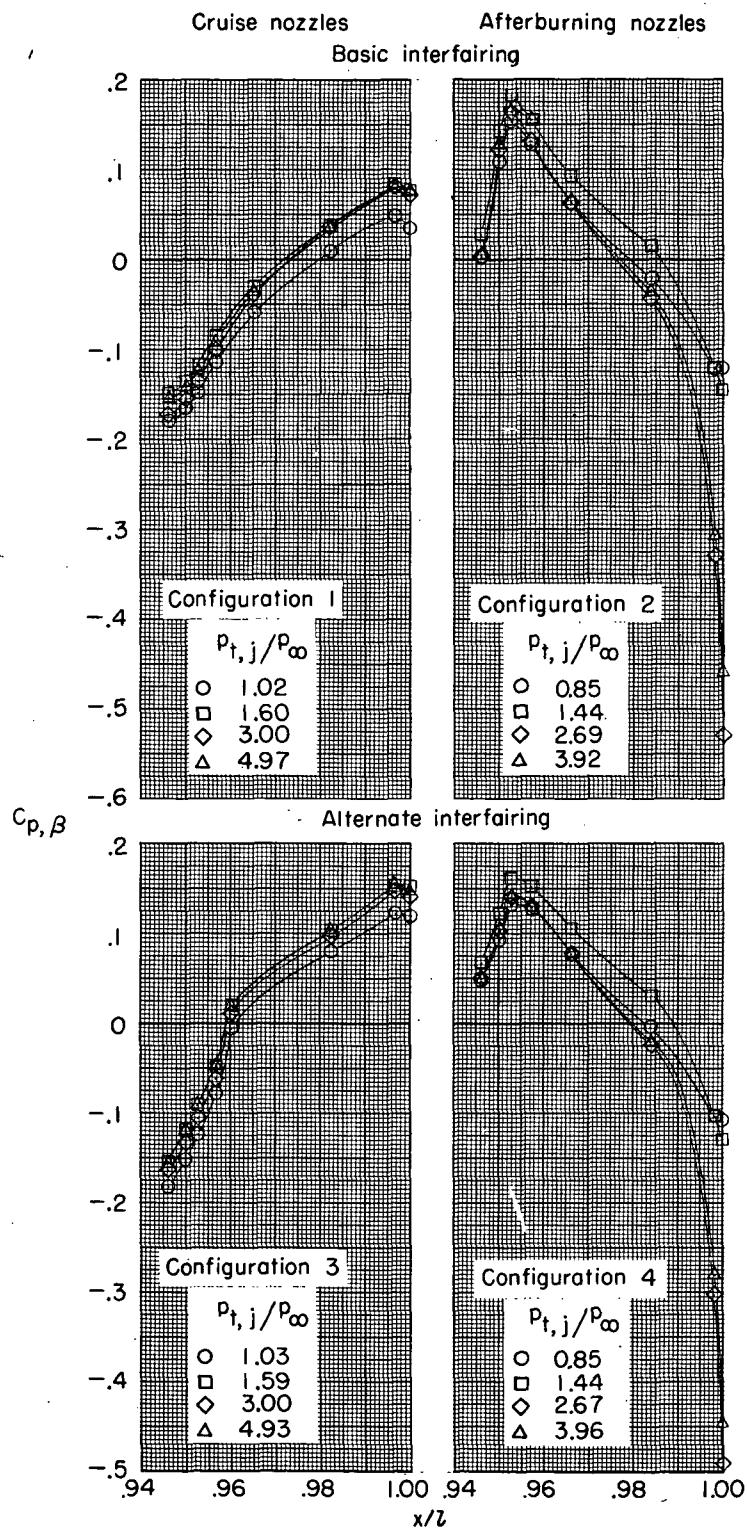
(a) Close-spaced afterbodies; M = 0.60.

Figure 18.- Effects of jet operation on nozzle-pressure-coefficient
distributions for the $\theta = 0^{O}$ row.

Cruise nozzles   Afterburning nozzles

Basic interfairing

$C_{p,\beta}$

Configuration 1

$p_{t,j}/p_\infty$

○ 1.00
□ 1.60
◇ 3.03
△ 5.95

Configuration 2

$p_{t,j}/p_\infty$

○ 0.83
□ 1.45
◇ 2.67
△ 4.68

Alternate interfairing

Configuration 3

$p_{t,j}/p_\infty$

○ 1.05
□ 1.59
◇ 2.98
△ 5.93

Configuration 4

$p_{t,j}/p_\infty$

○ 0.83
□ 1.43
◇ 2.67
△ 4.70

x/l

(b) Close-spaced afterbodies;   M = 0.80.

Figure 18.- Continued.

75

Cruise nozzles   Afterburning nozzles

Basic interfairing

Configuration 1

$P_{t,j}/P_\infty$

O	0.98
□	1.56
◇	3.02
△	5.97

Configuration 2

$P_{t,j}/P_\infty$

O	0.82
□	1.36
◇	2.69
△	5.27

Alternate interfairing

Configuration 3

$P_{t,j}/P_\infty$

O	1.03
□	1.48
◇	3.00
△	5.92

Configuration 4

$P_{t,j}/P_\infty$

O	0.82
□	1.32
◇	2.70
△	5.26

$C_{p,\beta}$

x/l

(c) Close-spaced afterbodies; M = 0.90.

Figure 18.- Continued.

Basic interfairing

Alternate interfairing

Configuration 1

$$p_{t,j}/p_\infty$$

○	0.86
□	1.50
◇	2.94
△	7.89

Configuration 2

$$p_{t,j}/p_\infty$$

○	0.69
□	1.32
◇	2.68
△	7.06

Configuration 3

$$p_{t,j}/p_\infty$$

○	0.87
□	1.52
◇	2.96
△	7.91

Configuration 4

$$p_{t,j}/p_\infty$$

○	0.69
□	1.36
◇	2.71
△	7.04

$C_{p,\beta}$

x/l

(d) Close-spaced afterbodies; $M = 1.30$.

Figure 18.- Continued.

77

(e) Wide-spaced afterbodies; M = 0.60.

Figure 18.- Continued.
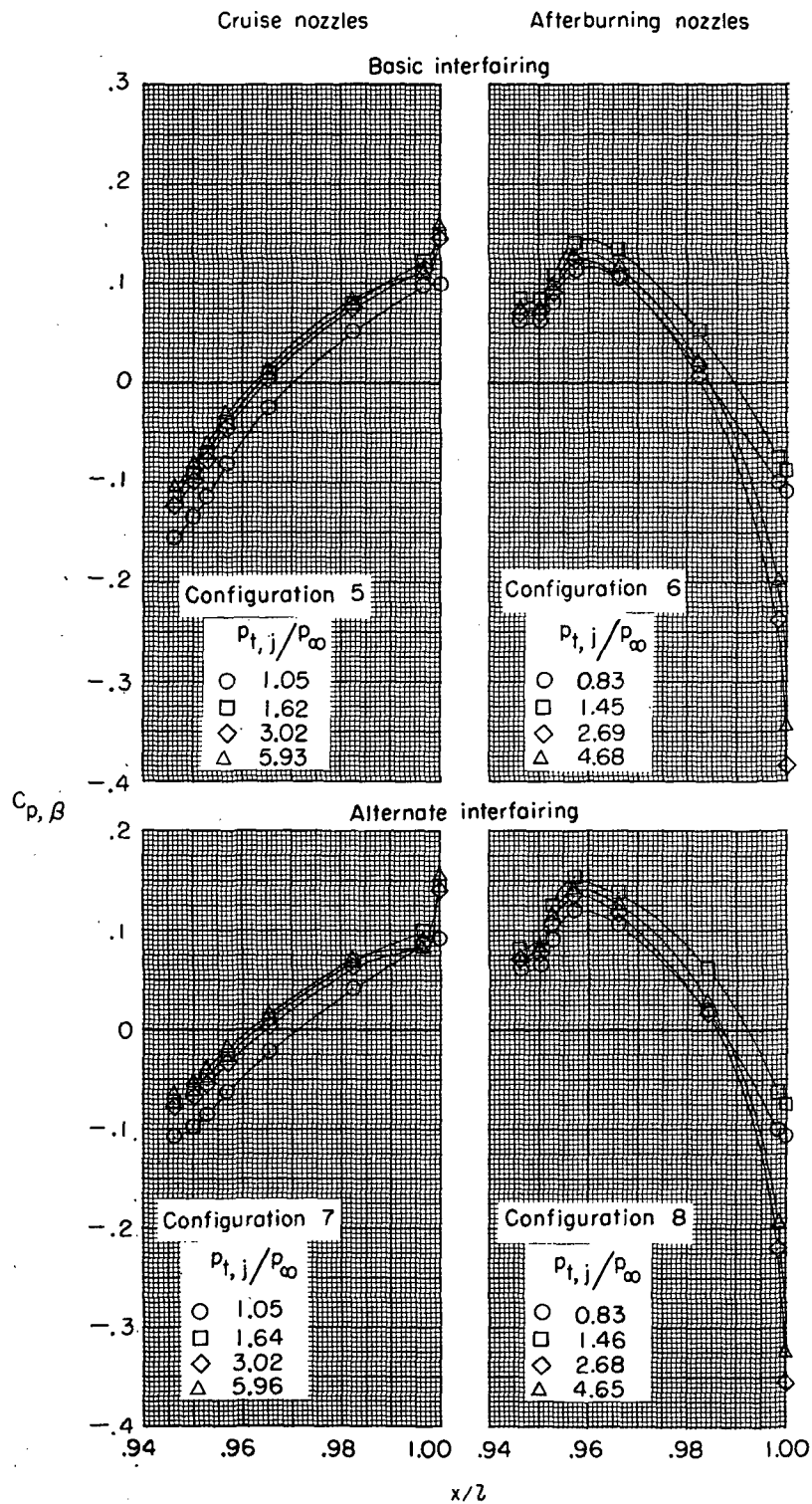
(f) Wide-spaced afterbodies; M = 0.80.

Figure 18.- Continued.
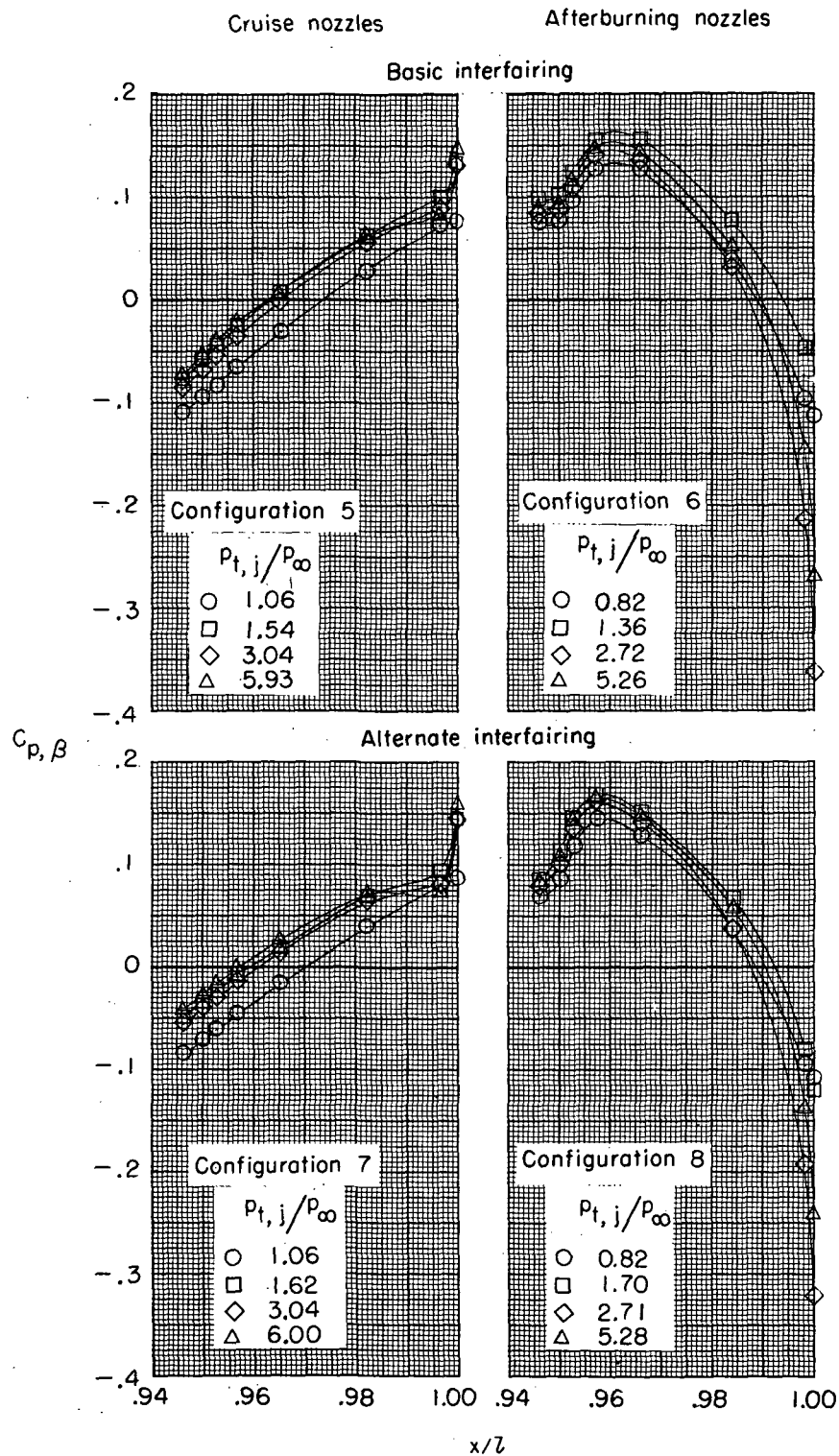
(g) Wide-spaced afterbodies; M = 0.90.

Figure 18.- Continued.
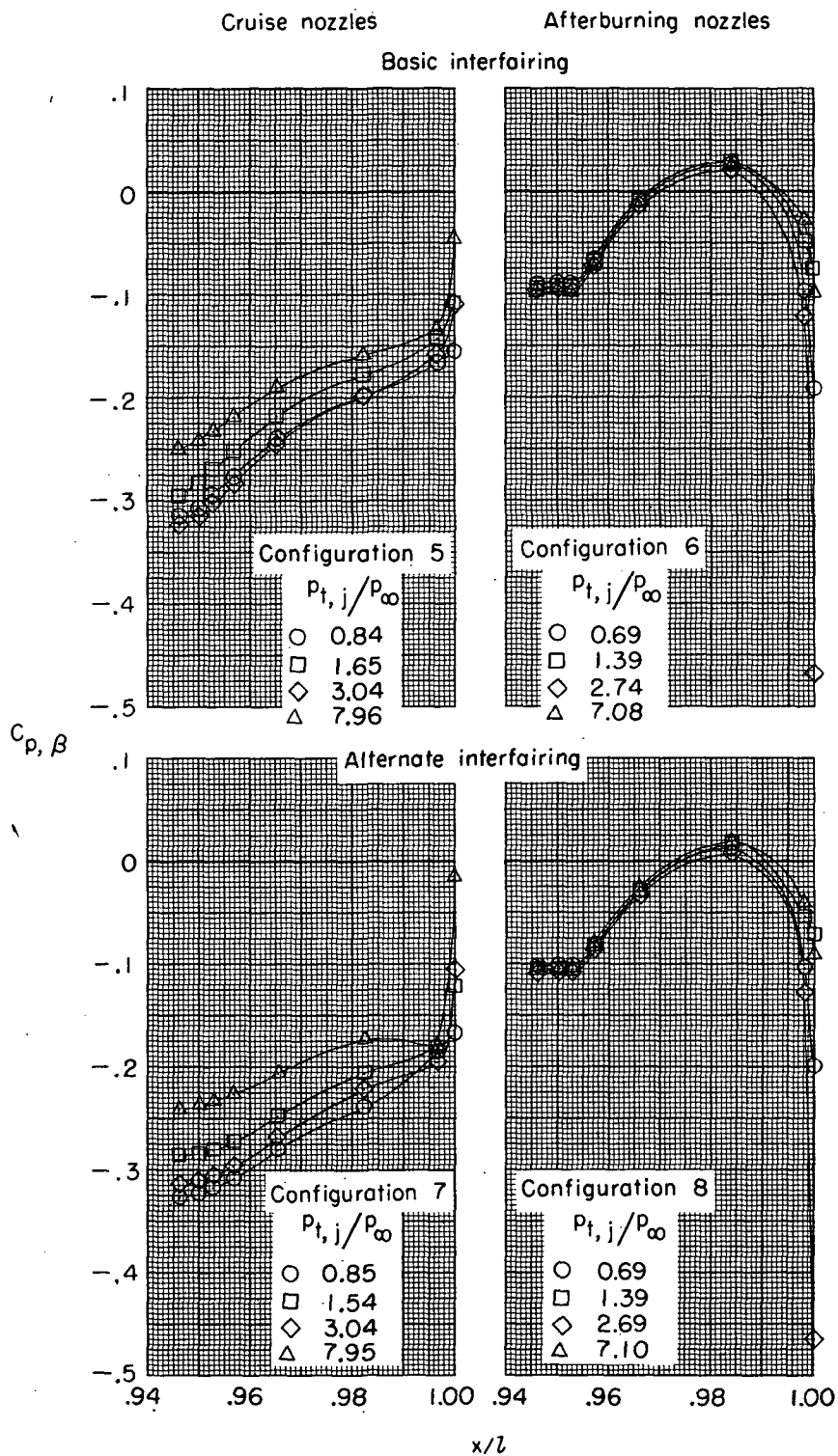
(h) Wide-spaced afterbodies; M = 1.30.

Figure 18.- Concluded.
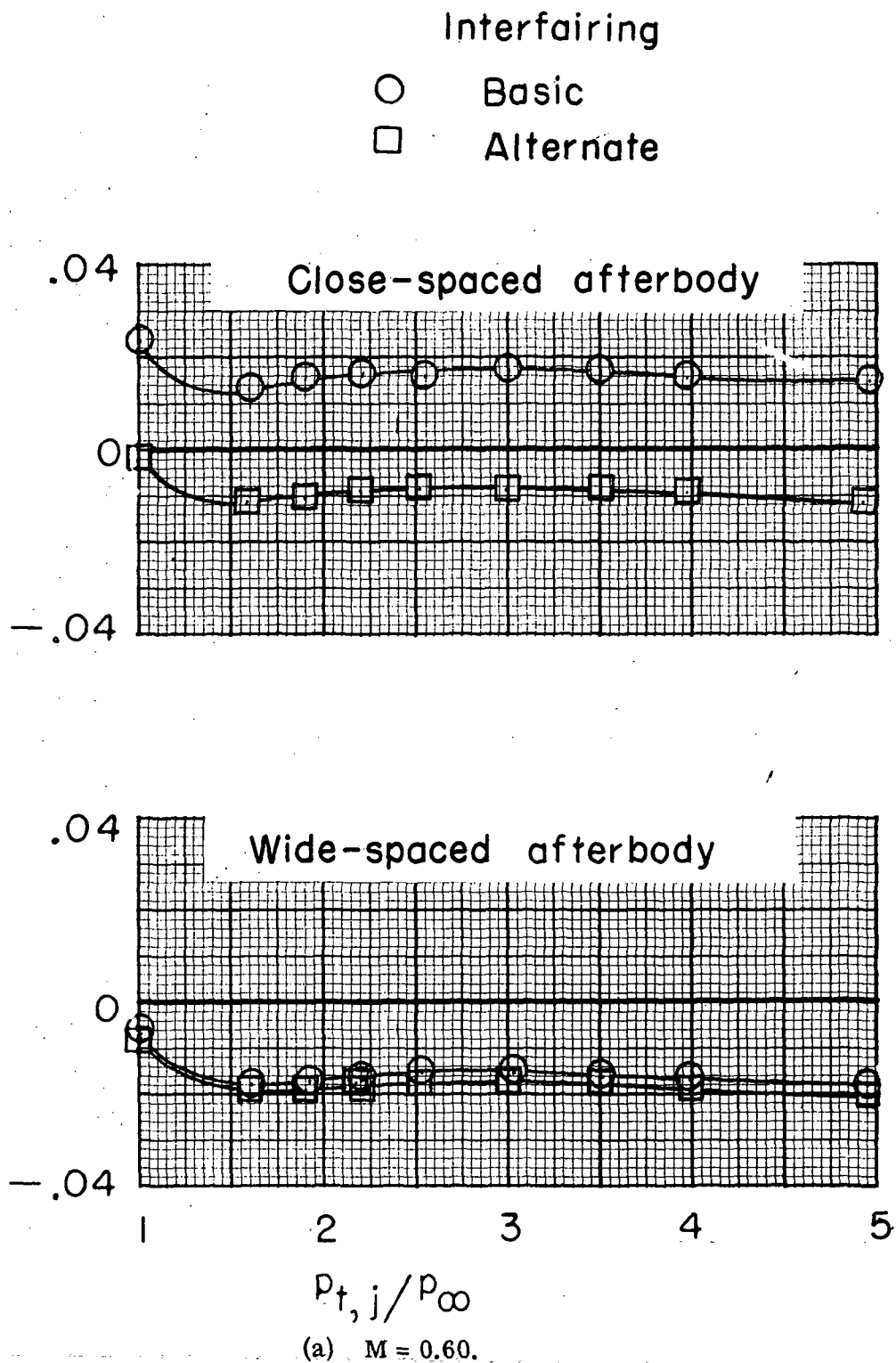
Figure 19.- Variation of nozzle-boattail axial-force
coefficient with jet-total-pressure ratio for the
cruise-nozzle configurations.

Interfairing

○ Basic

□ Alternate

Close-spaced afterbody

Wide-spaced afterbody

$C_{A,\beta}$
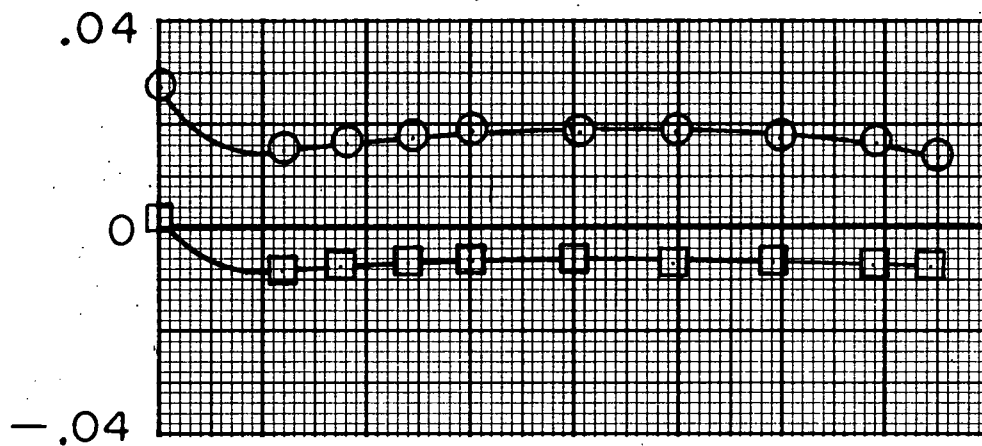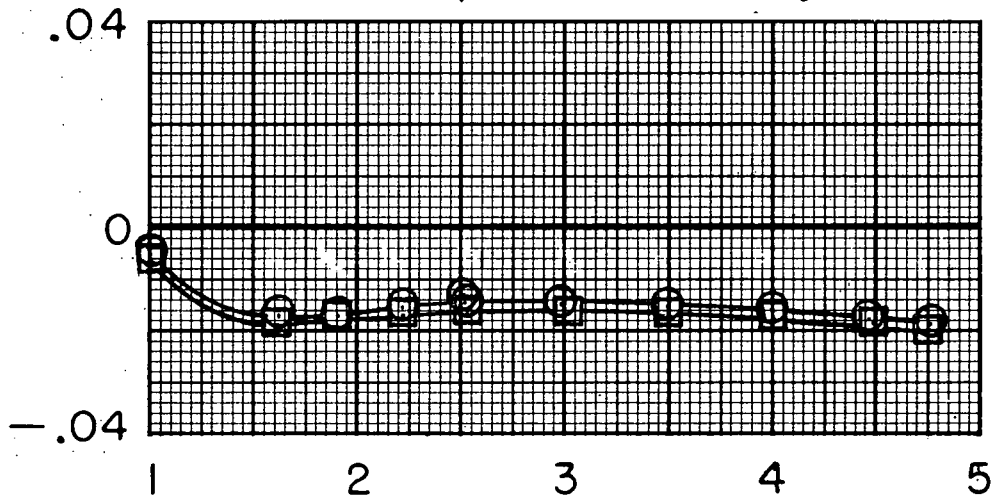
$p_{t,j}/p_\infty$

(b)   M = 0.70.

Figure 19.- Continued.

Interfairing

○ Basic
□ Alternate

Close-spaced afterbody

Wide-spaced afterbody

$C_{A,\beta}$

$p_{t,j}/p_\infty$
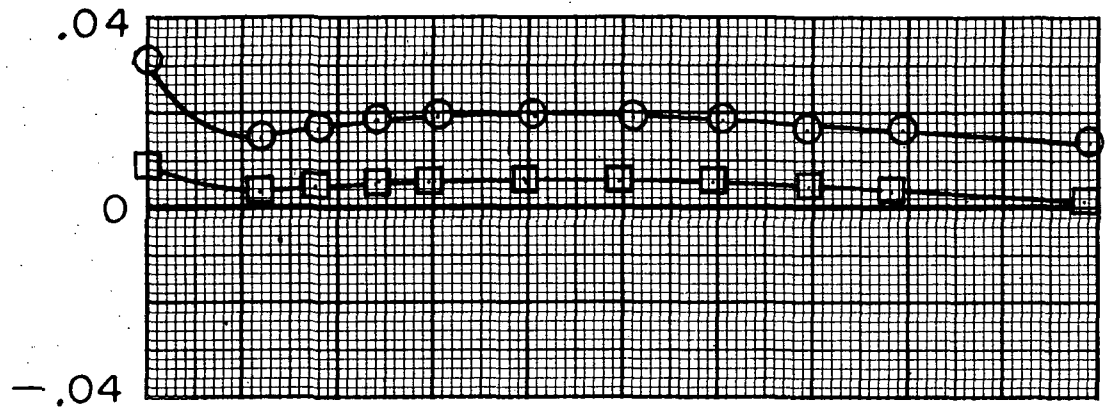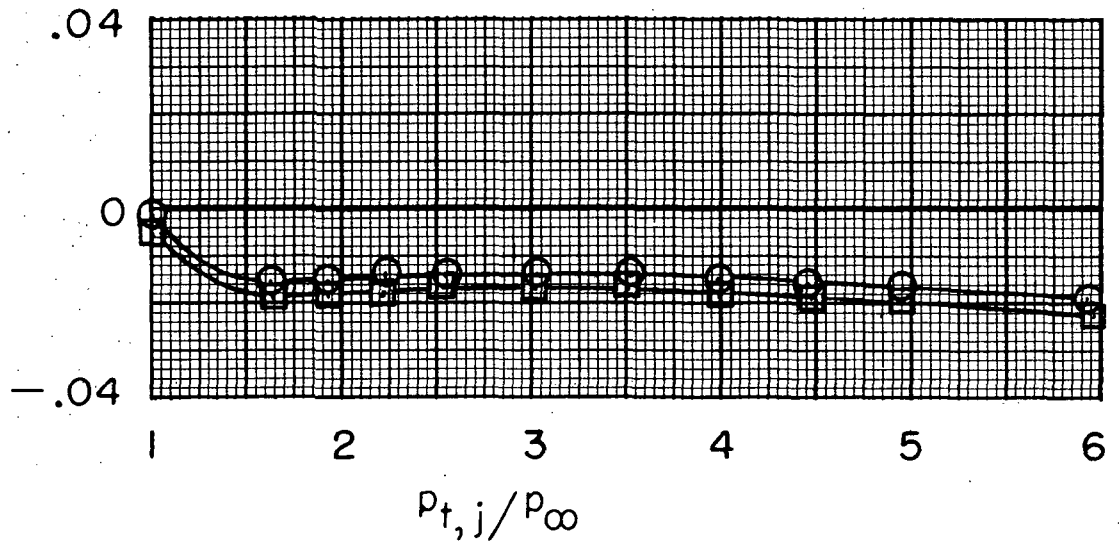
(c) M = 0.80.

Figure 19.- Continued.

84

Interfairing

○ Basic

□ Alternate

Close-spaced afterbodies

Wide-spaced afterbodies

$p_{t,j}/p_\infty$
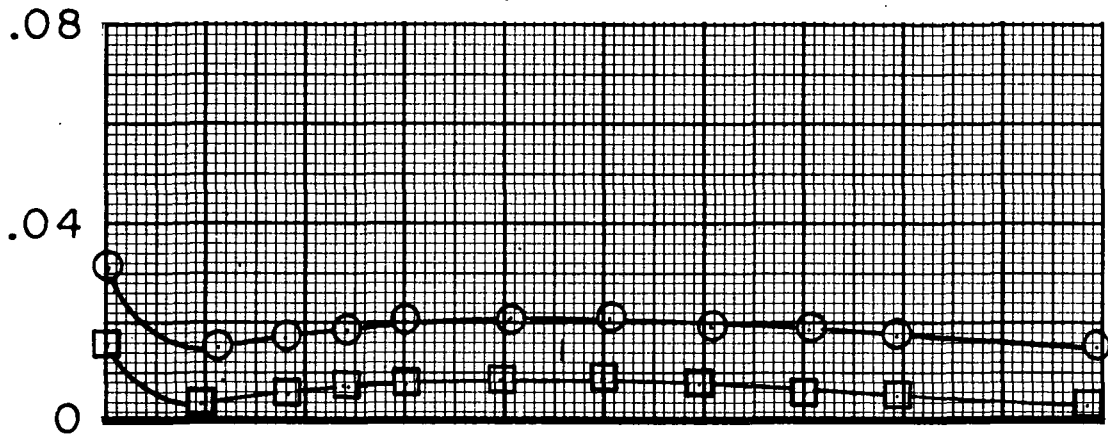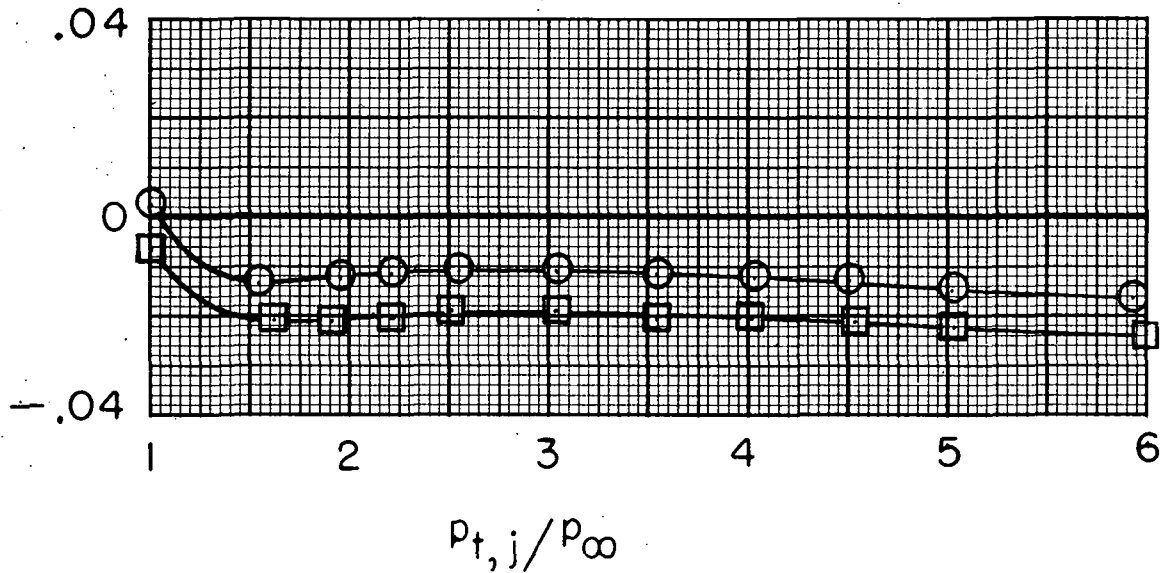
(d) M = 0.90.

Figure 19.- Continued.
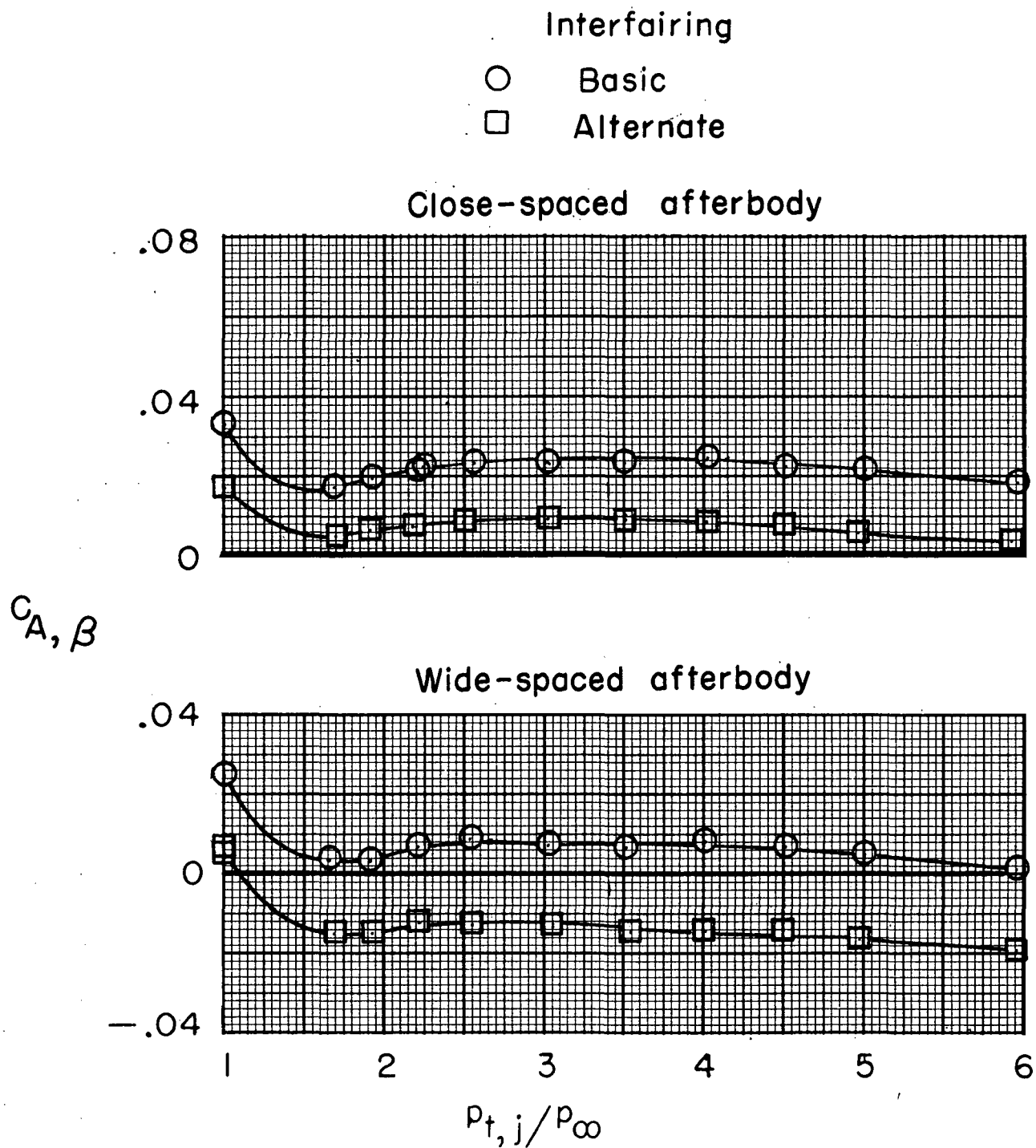
(e) M = 0.95.

Figure 19.- Continued.

Interfairing

○ Basic
□ Alternate

Close-spaced afterbody
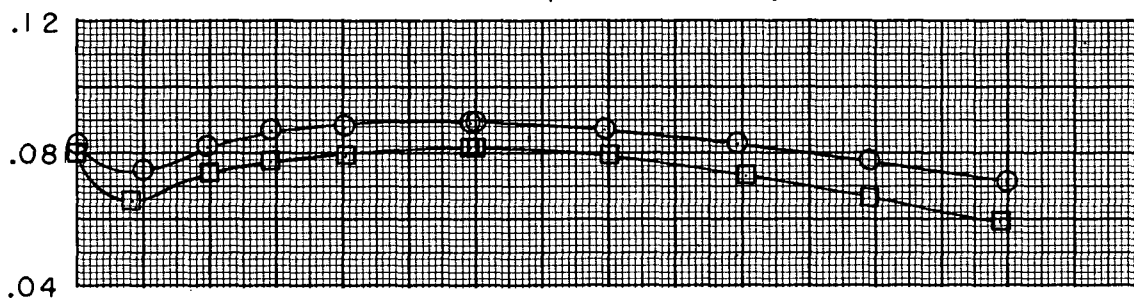
Wide-spaced afterbody

(f) M = 1.20.

Figure 19.- Continued.

Interfairing
○　　Basic
□　　Alternate

Close-spaced afterbody

Wide-spaced afterbody

$C_{A,\beta}$

$p_{t,j}/p_\infty$
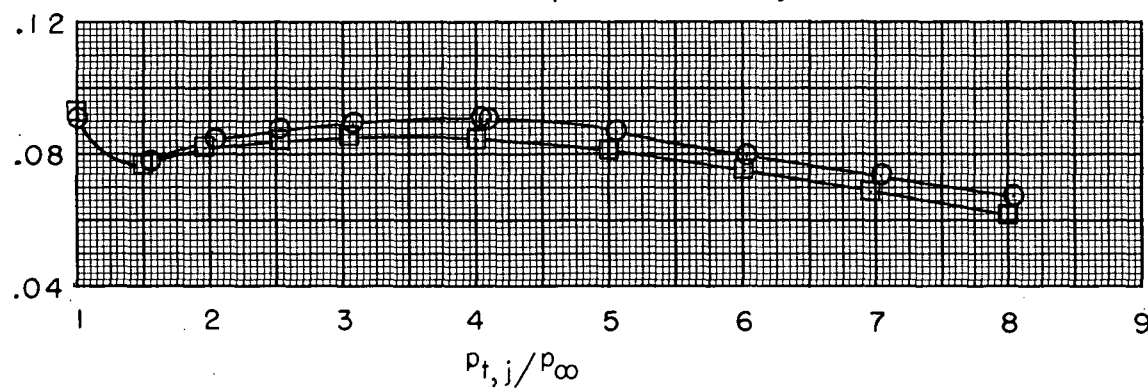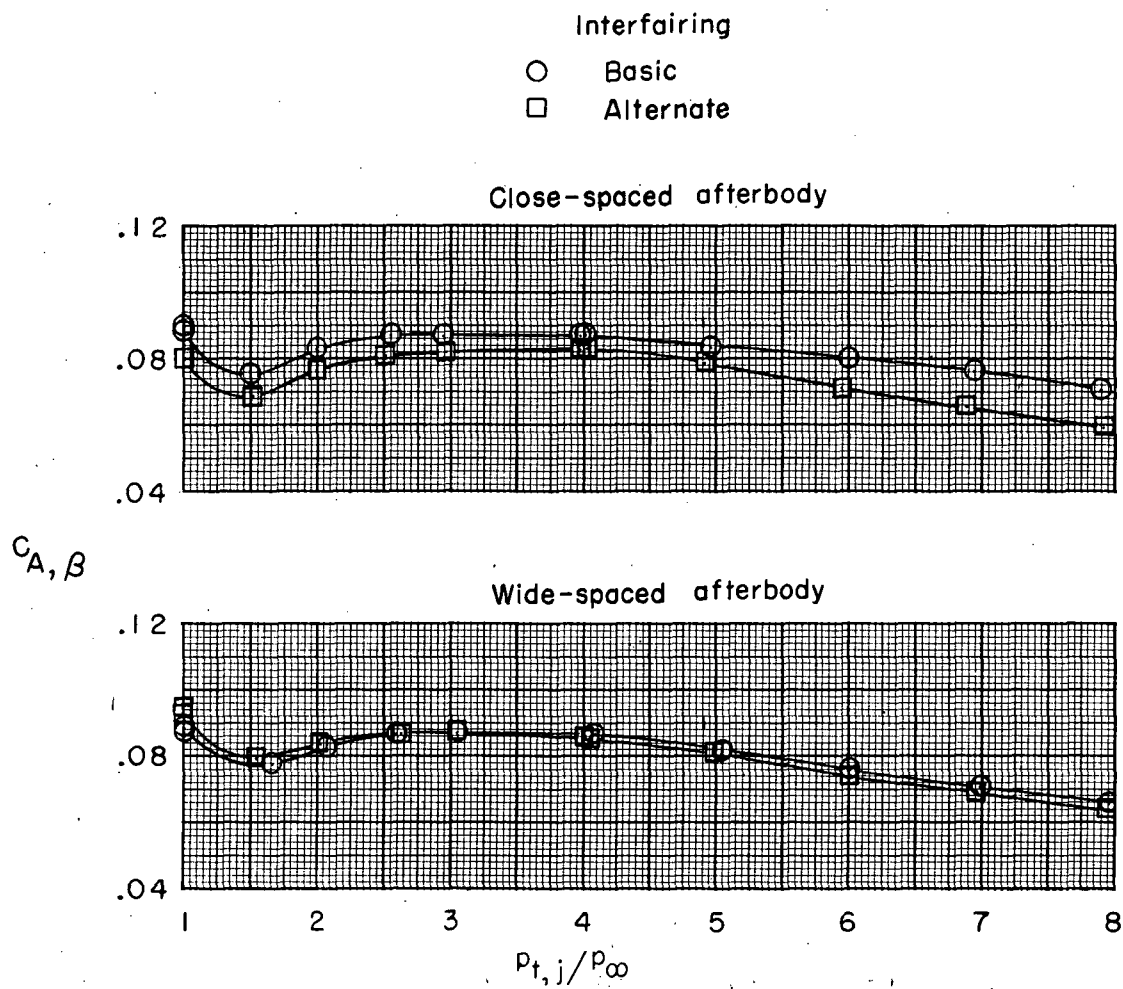
(g)　M = 1.30.

Figure 19.- Concluded.

Basic interfairing

Alternate interfairing

$C_{A, \beta}$

M
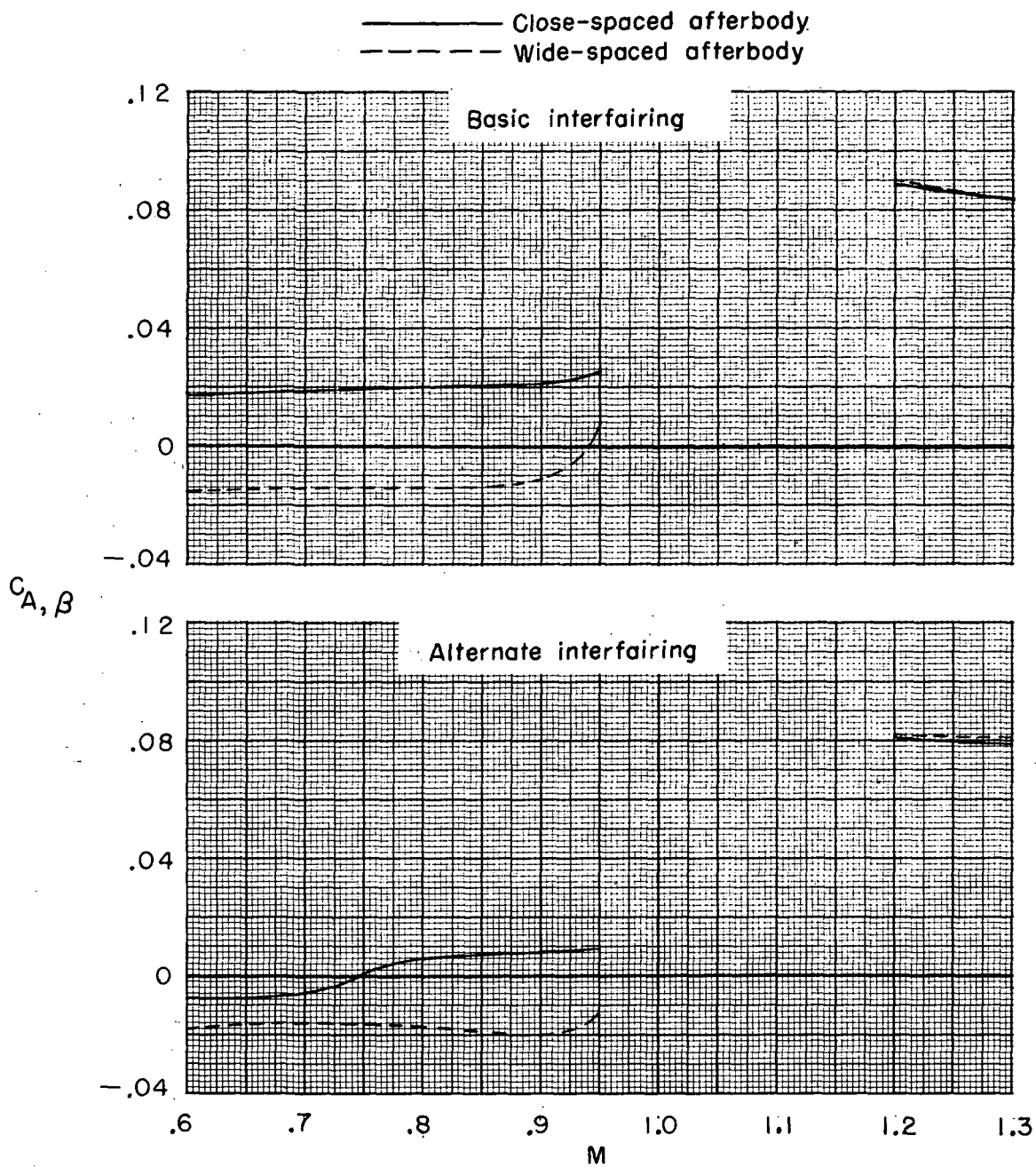
Figure 20.- Variation of nozzle-boattail axial-force coefficient at scheduled jet-total-
pressure ratios for the cruise-nozzle configurations.
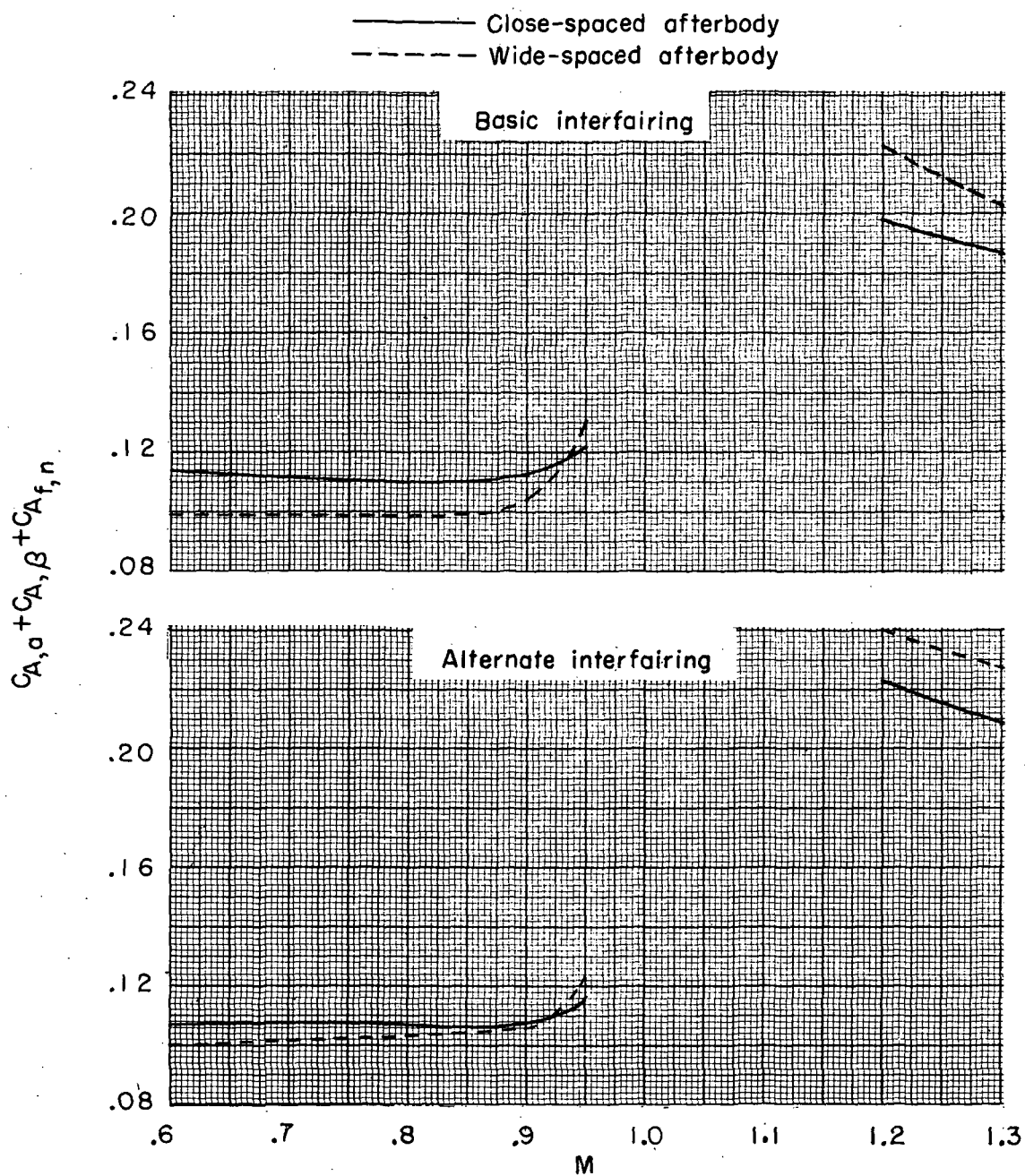
Figure 21.- Variation of total-axial-force coefficient at scheduled jet-total-pressure ratio for the cruise-nozzle configurations.
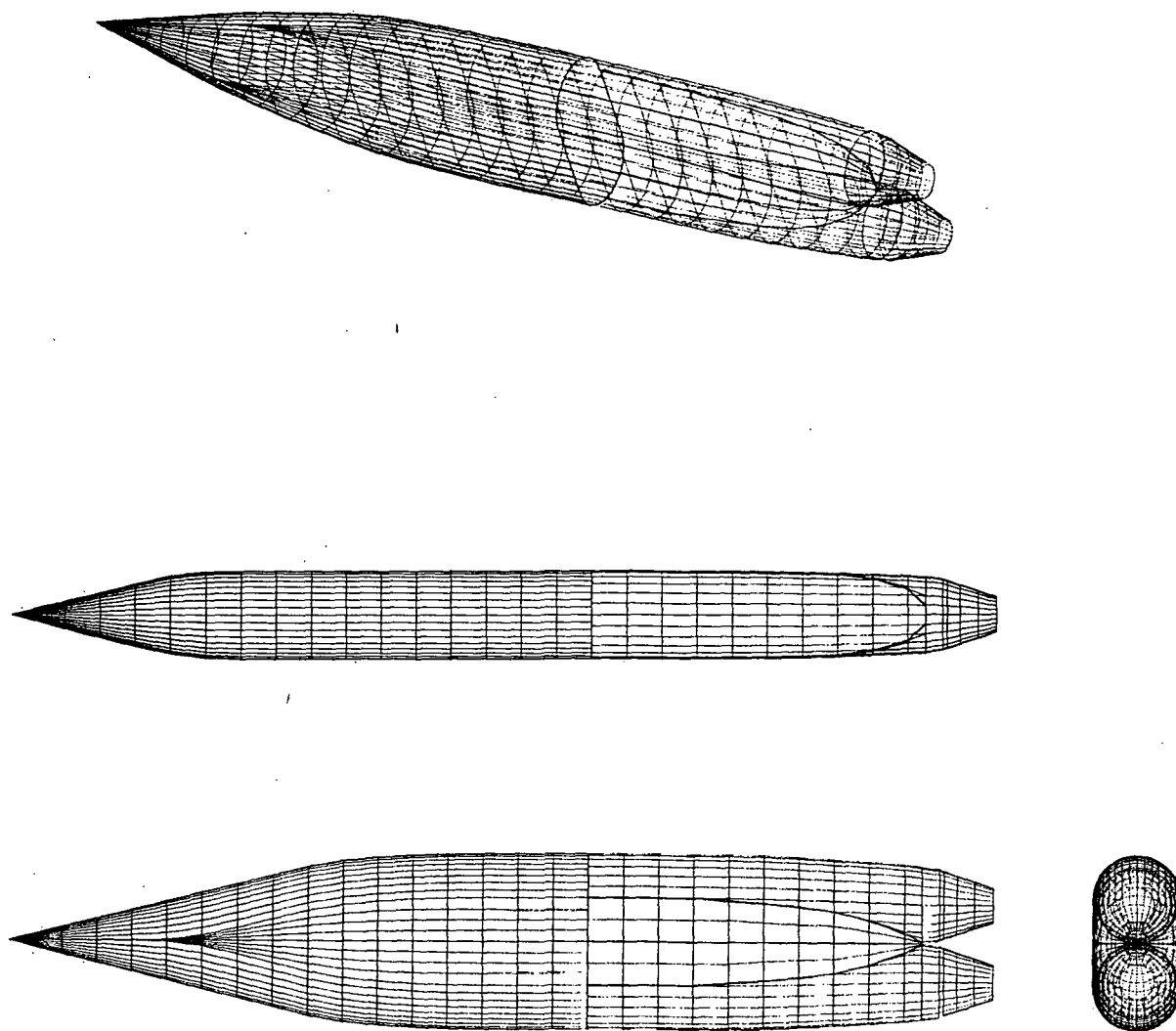
(a) Configuration 3.

Figure 22.- Typical machine-plotted illustrations of mathematical models
used in skin-friction and wave-drag calculations.
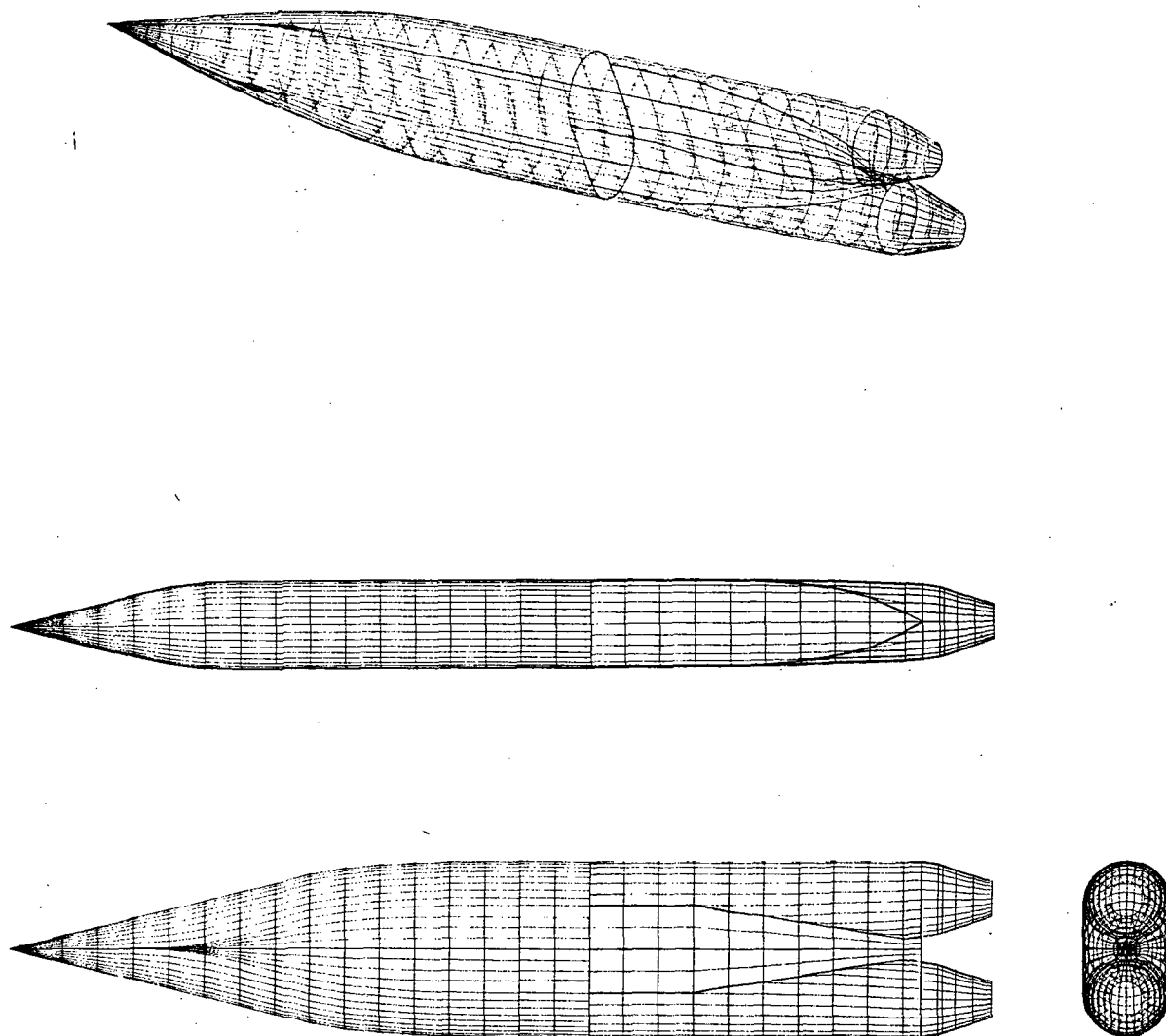
(b) Configuration 7.

Figure 22.- Concluded.
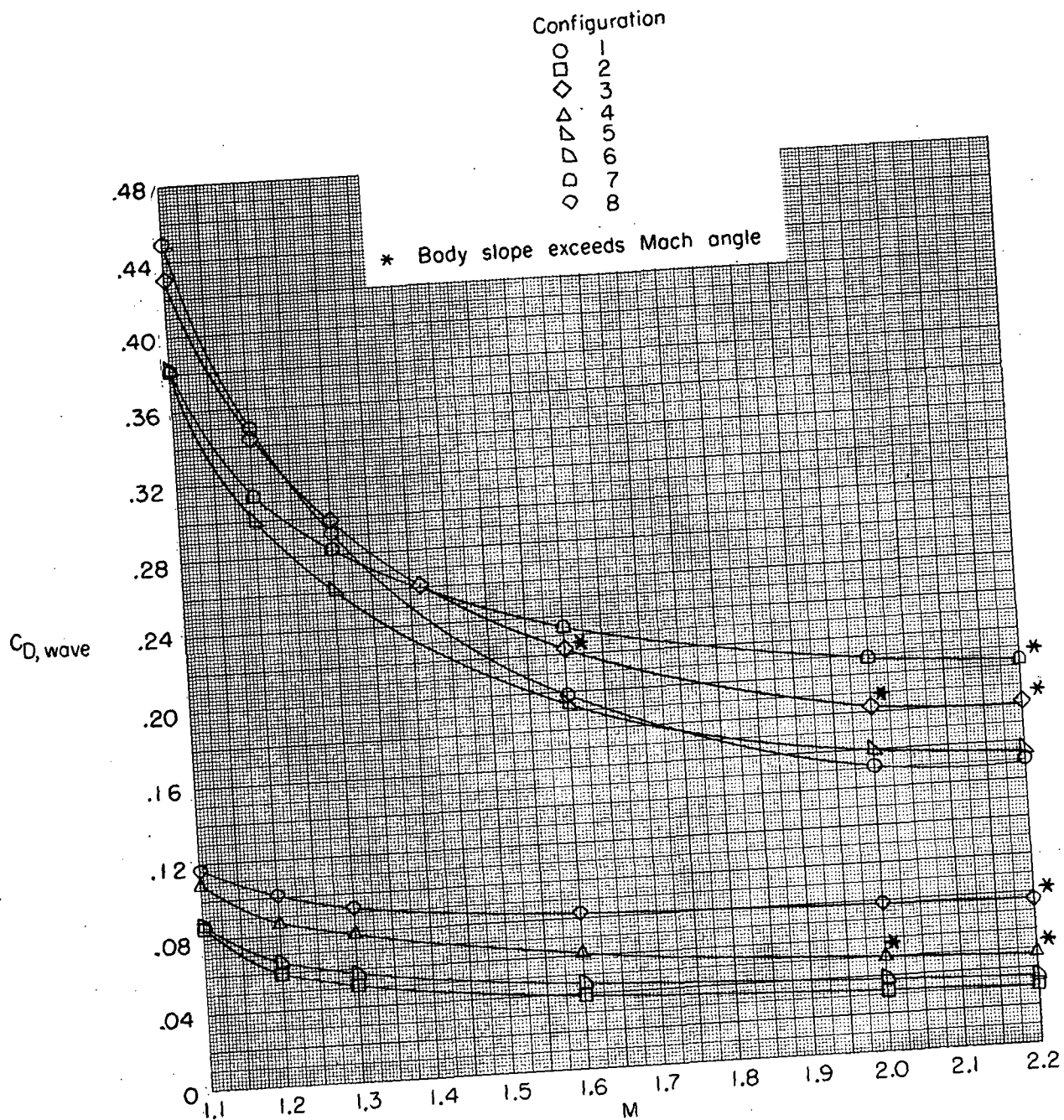
Figure 23.- Variation of calculated afterbody-plus-nozzle wave-drag coefficient with Mach number for the various configurations.

○ Close-spaced, basic interfairing
□ Close-spaced, alternate interfairing
◇ Wide-spaced, basic interfairing
△ Wide-spaced, alternate interfairing
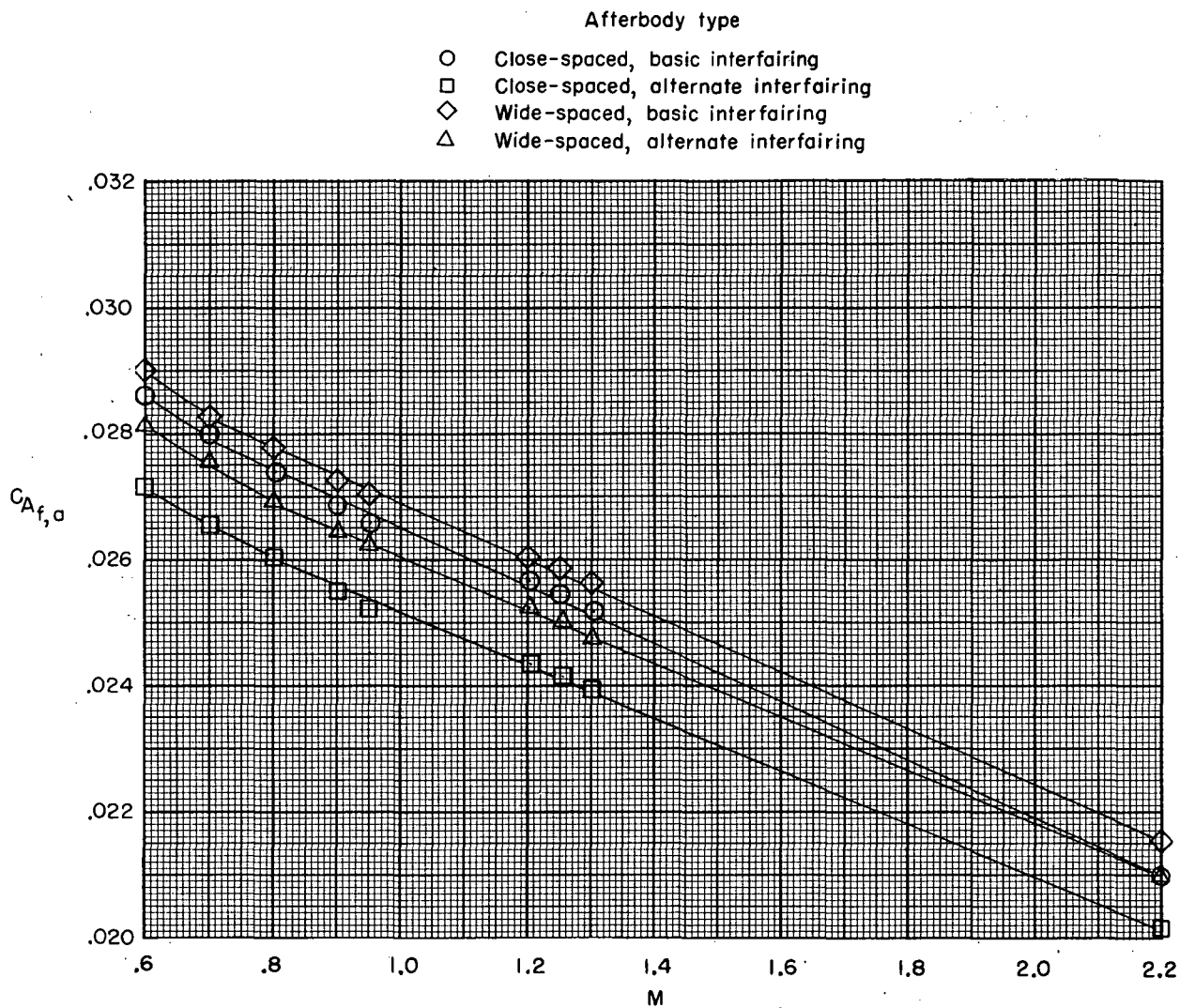
(a) Skin-friction axial-force coefficient of the afterbodies.

Figure 24.- Variation of calculated skin-friction axial-force coefficient with Mach number for the various afterbody components.

94
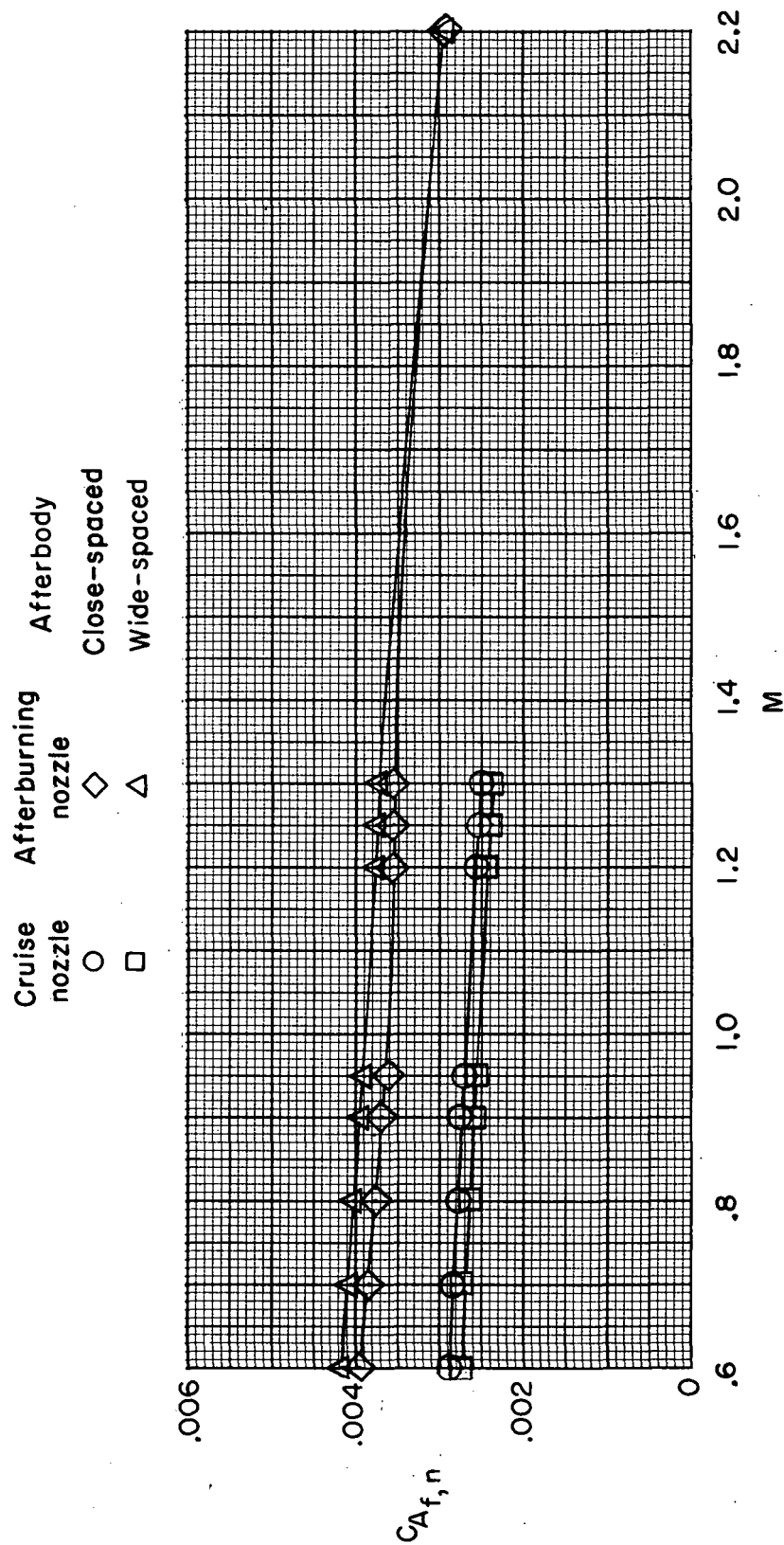
(b) Skin-friction axial-force coefficient of the nozzles.

Figure 24.- Concluded.
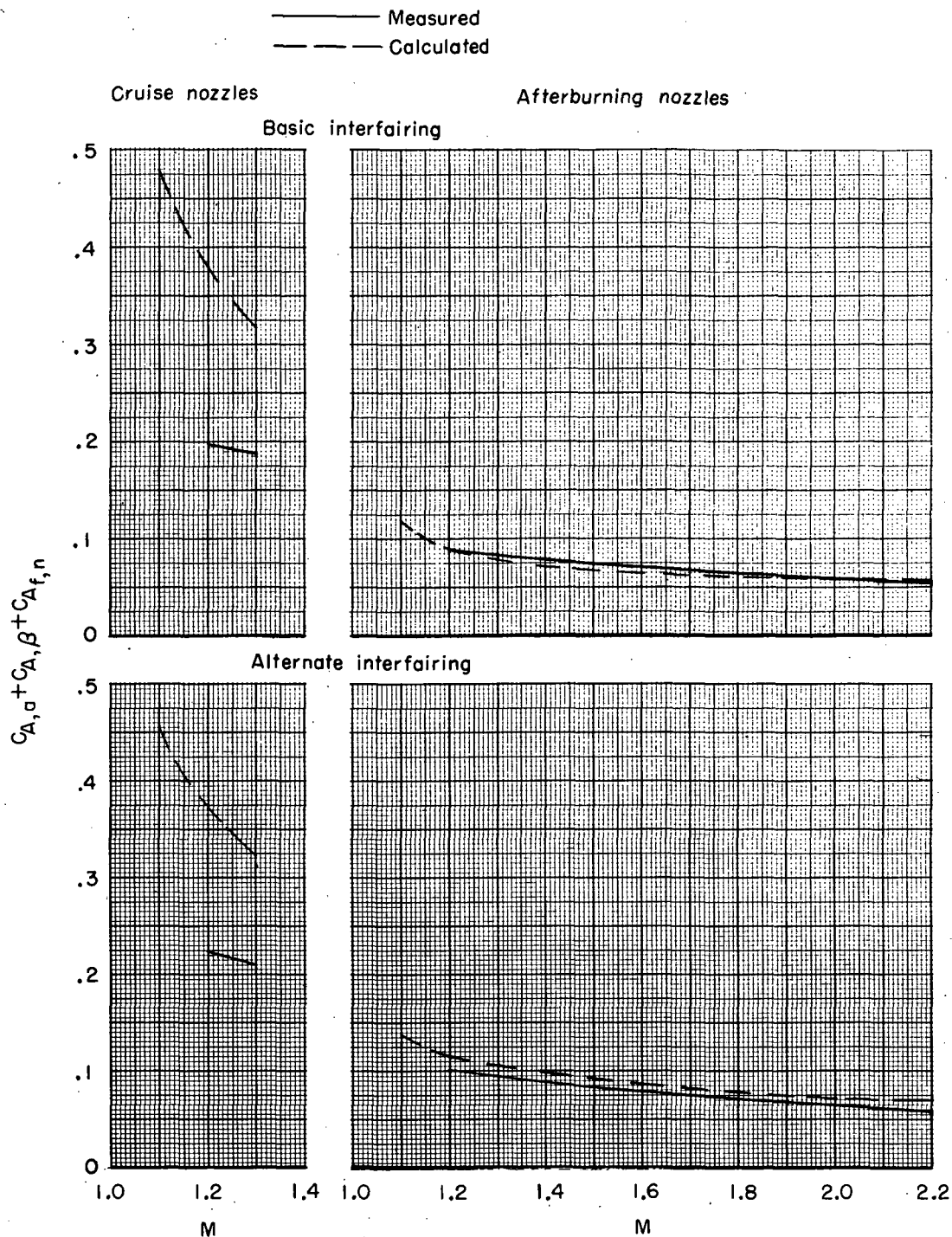
(a) Close-spaced afterbodies.

Figure 25.- Comparison of measured total-axial-force coefficient with the sum of the computed values of wave-drag coefficient and skin-friction-drag coefficient.
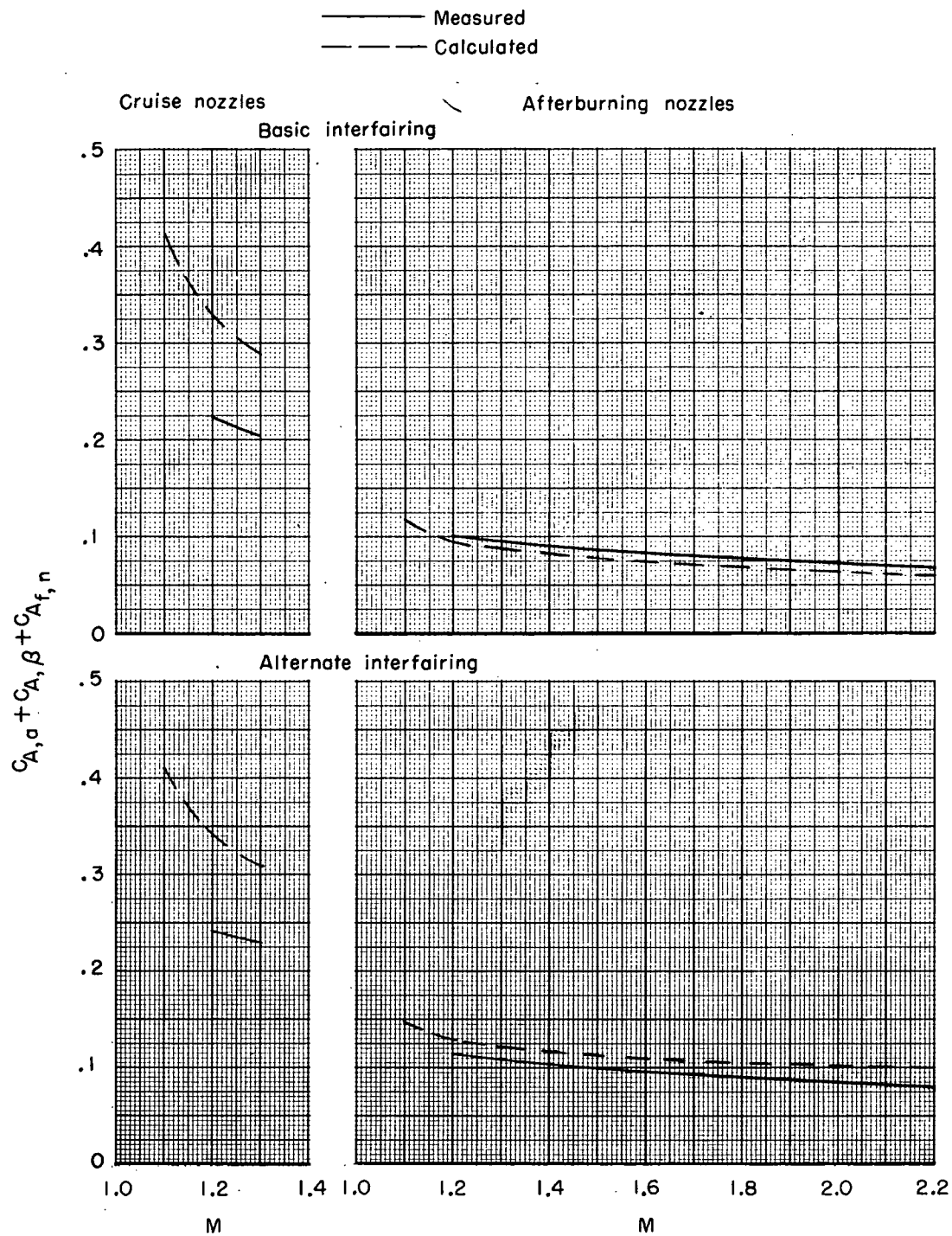
(b) Wide-spaced afterbodies.

Figure 25.- Concluded.
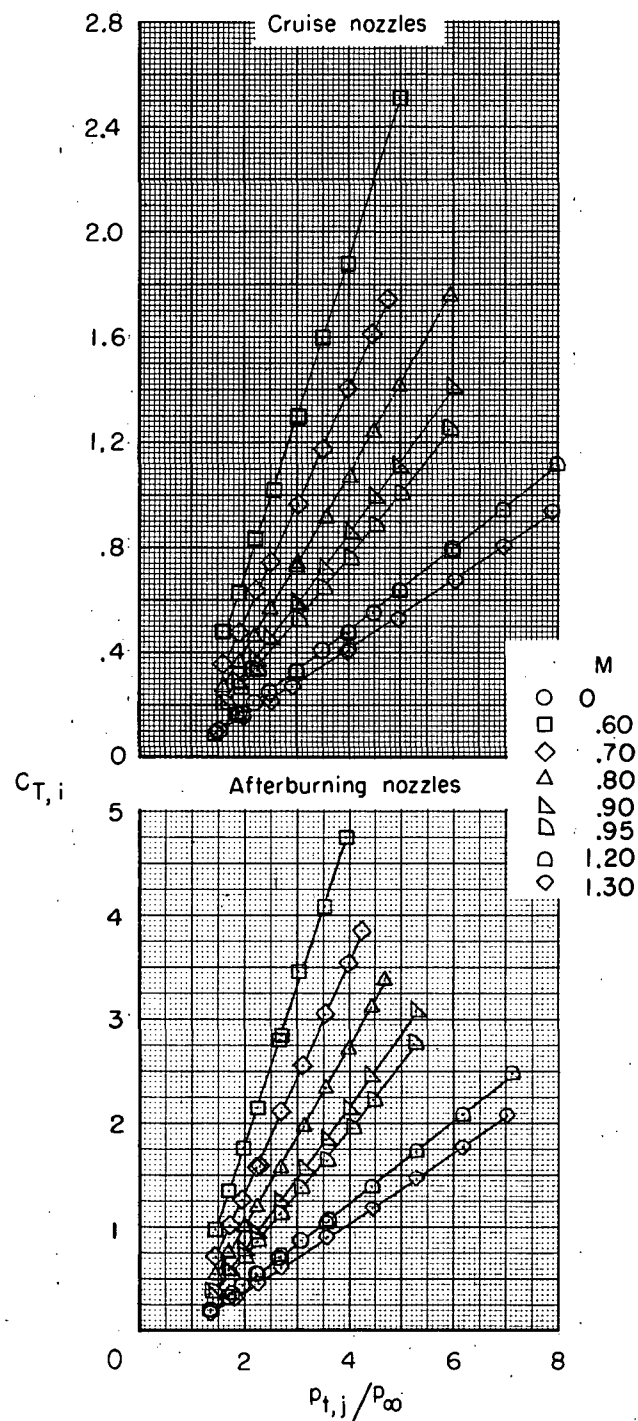
(a) M = 0 to 1.30.

Figure 26.- Variation of ideal isentropic thrust coefficient with jet-total-pressure ratio.
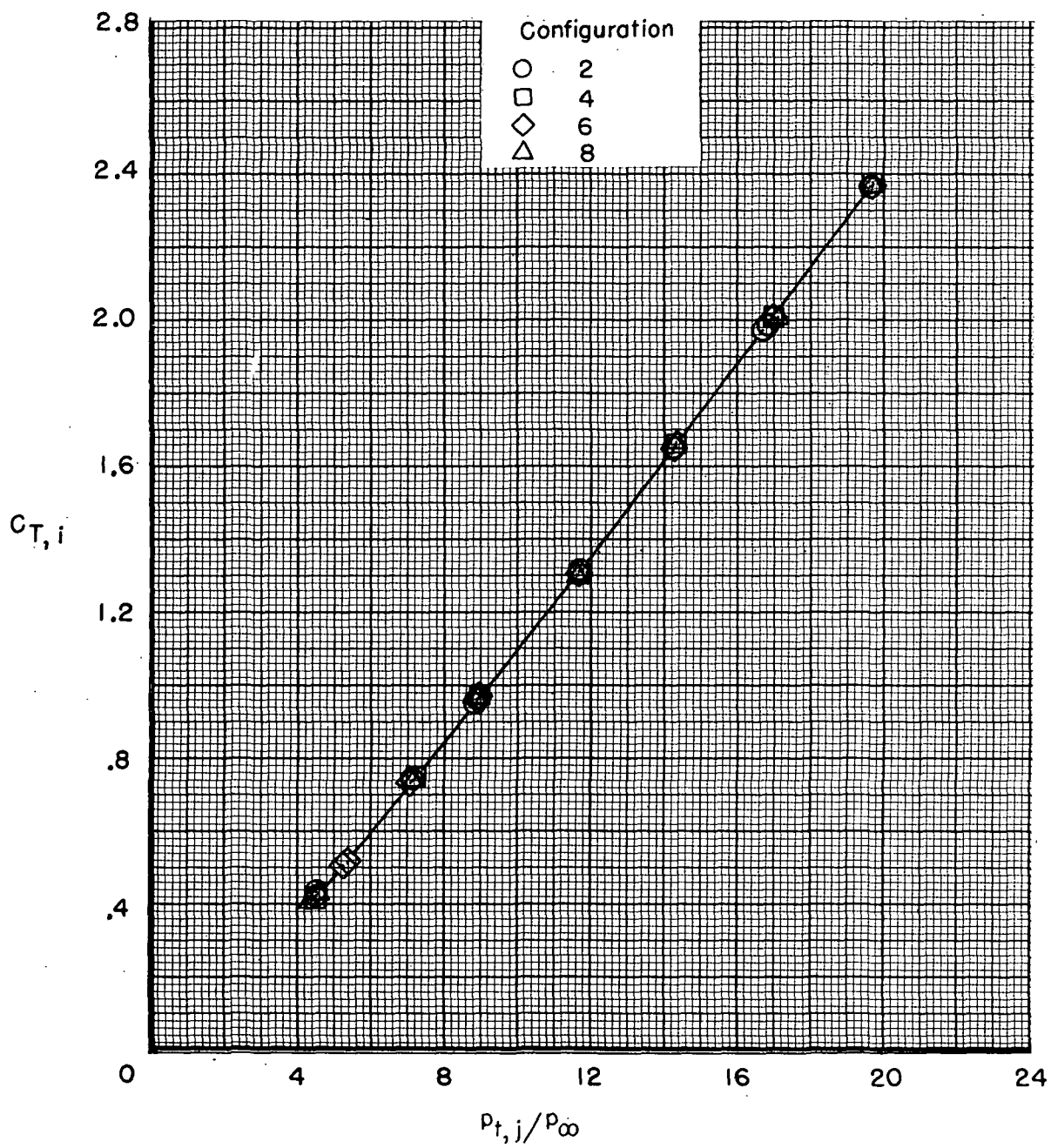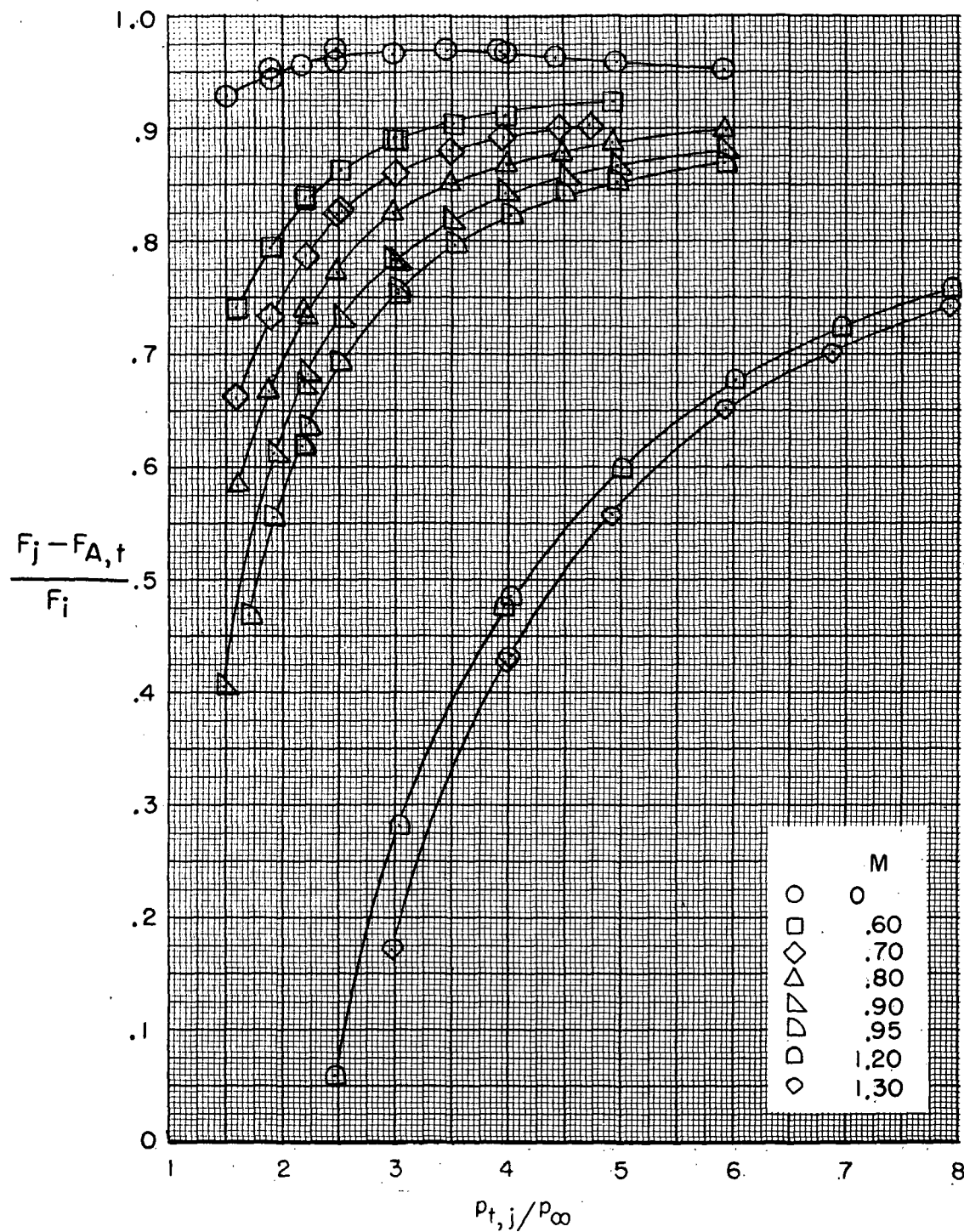
(b)   M = 2.20.

Figure 26.- Concluded.
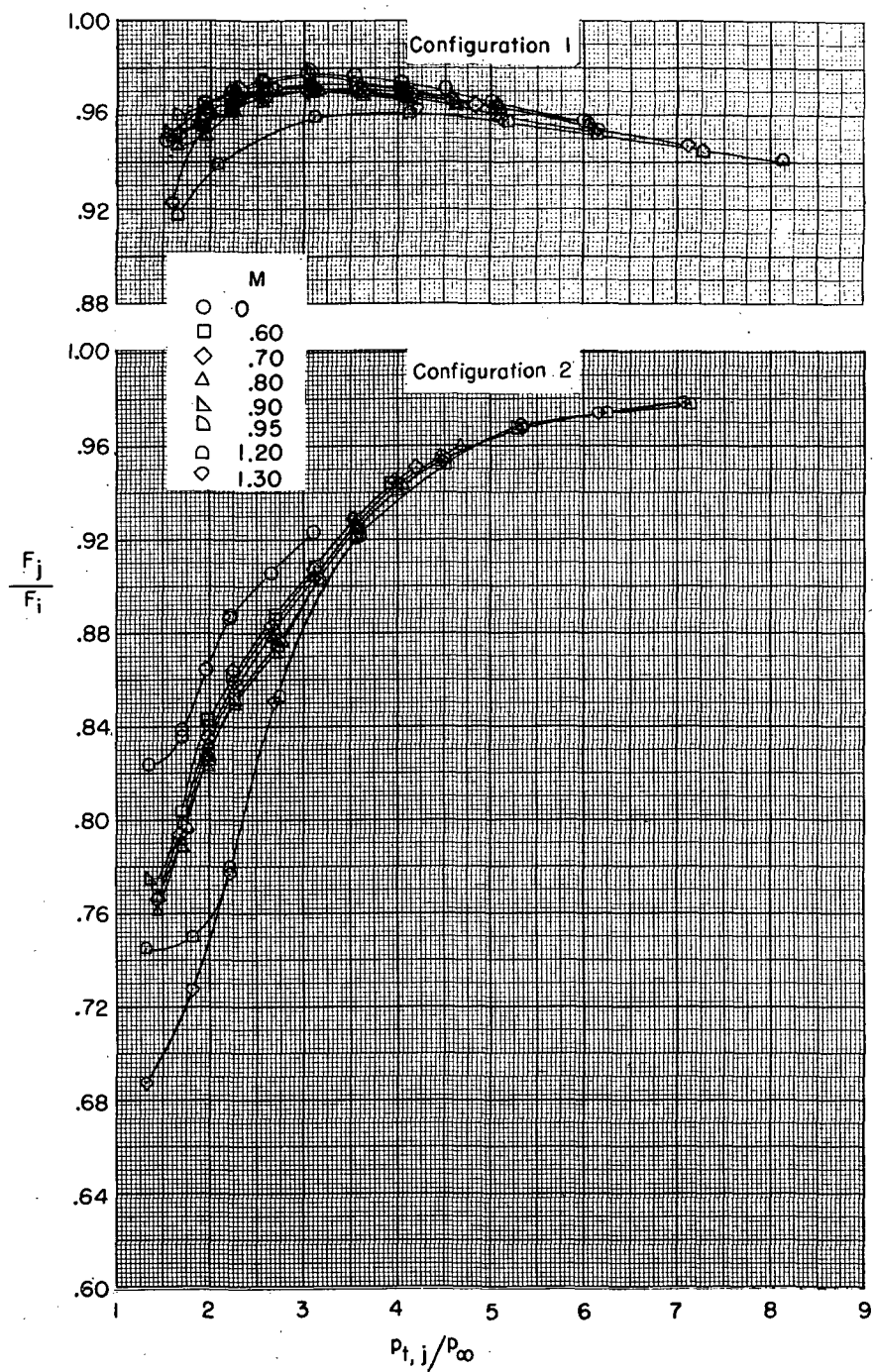
(a) Configurations 1 and 2.

Figure 27.- Variation of gross-thrust ratio with jet-total-pressure
ratio for the various configurations.

Configuration 3

Configuration 4

M	
○	0
□	.60
◇	.70
△	.80
◭	.90
◰	.95
◻	1.20
◇	1.30

$\frac{F_j}{F_i}$

$P_{t,j}/P_\infty$
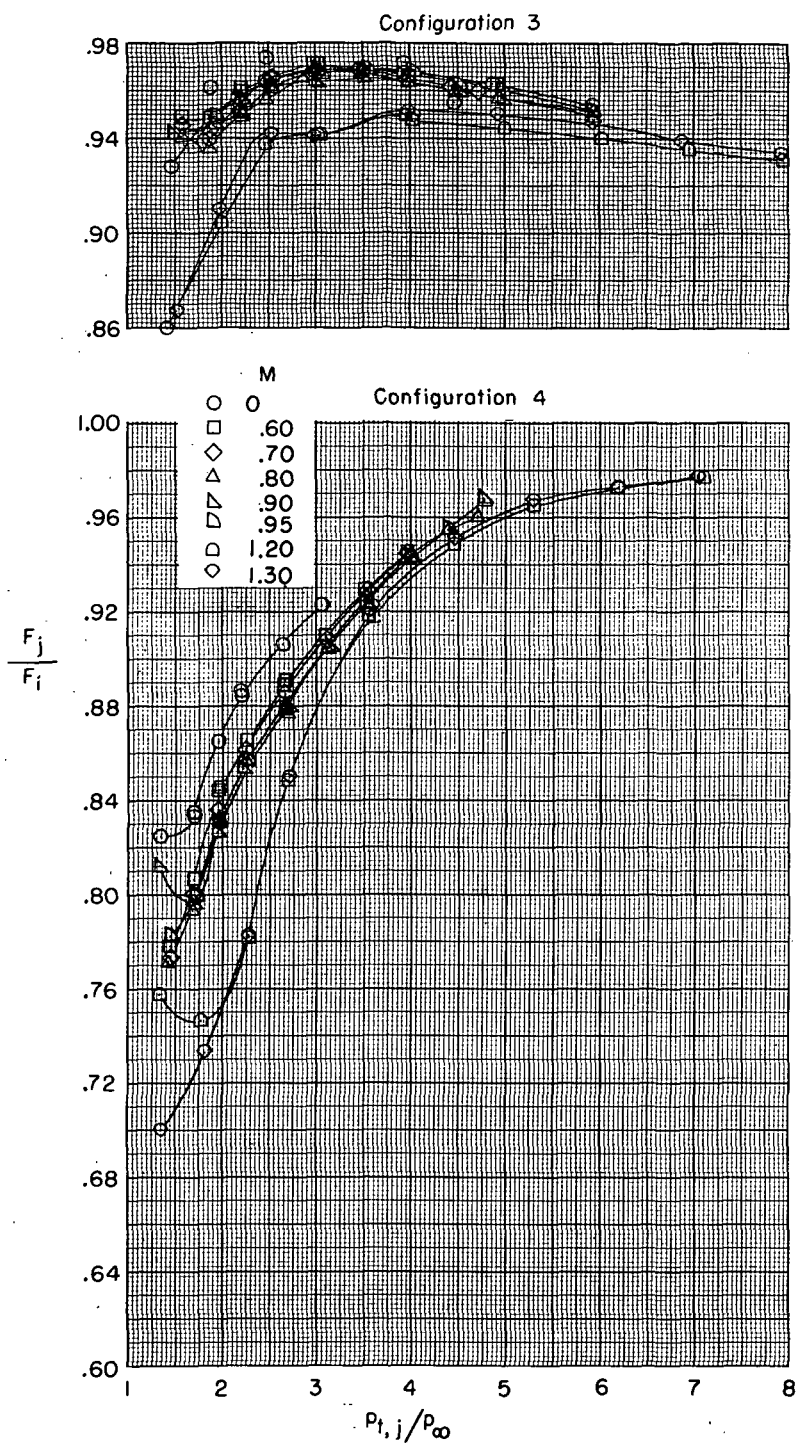
(b) Configurations 3 and 4.

Figure 27.- Continued.
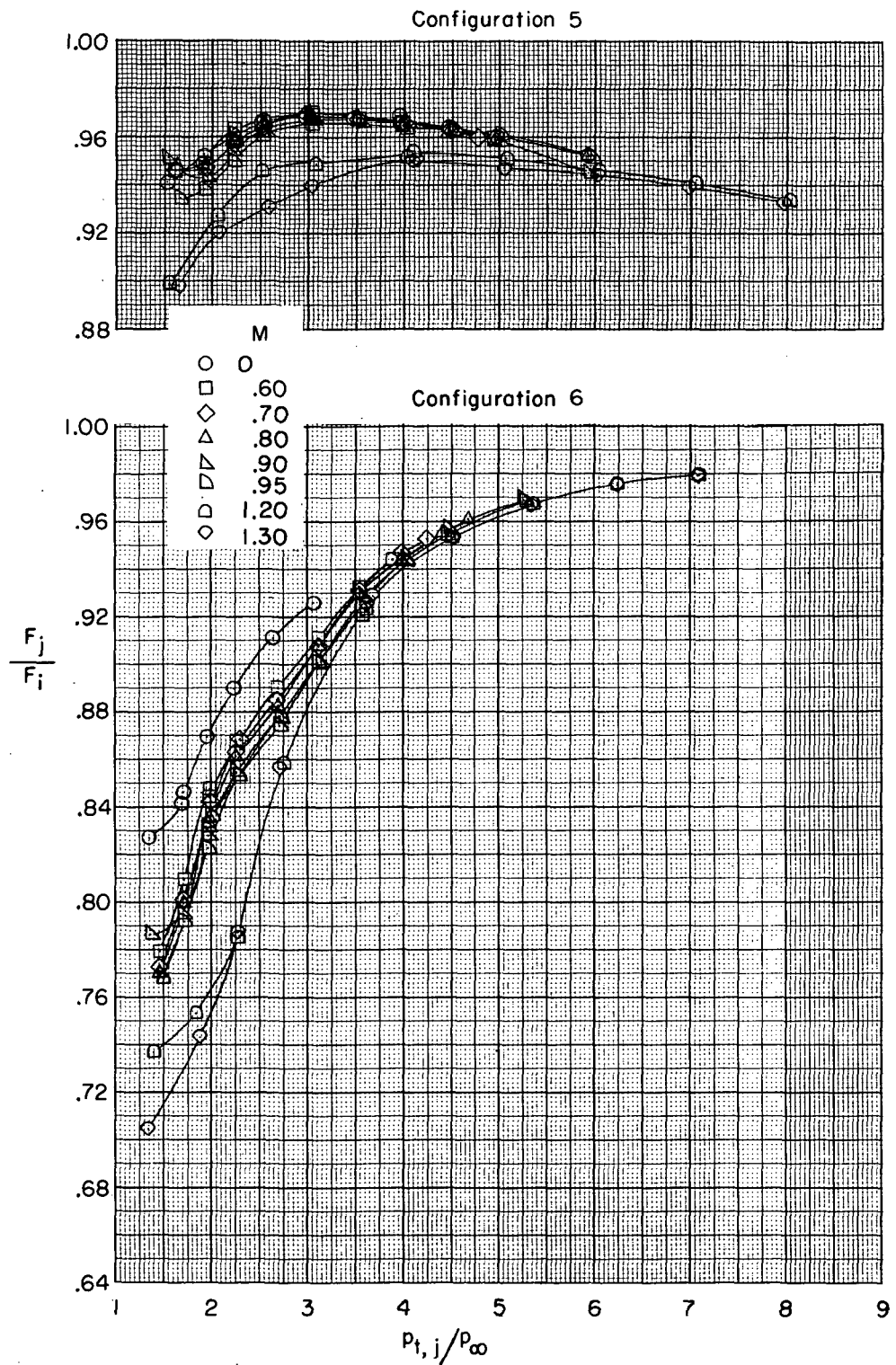
(c) Configurations 5 and 6.

Figure 27.- Continued.

Configuration 7
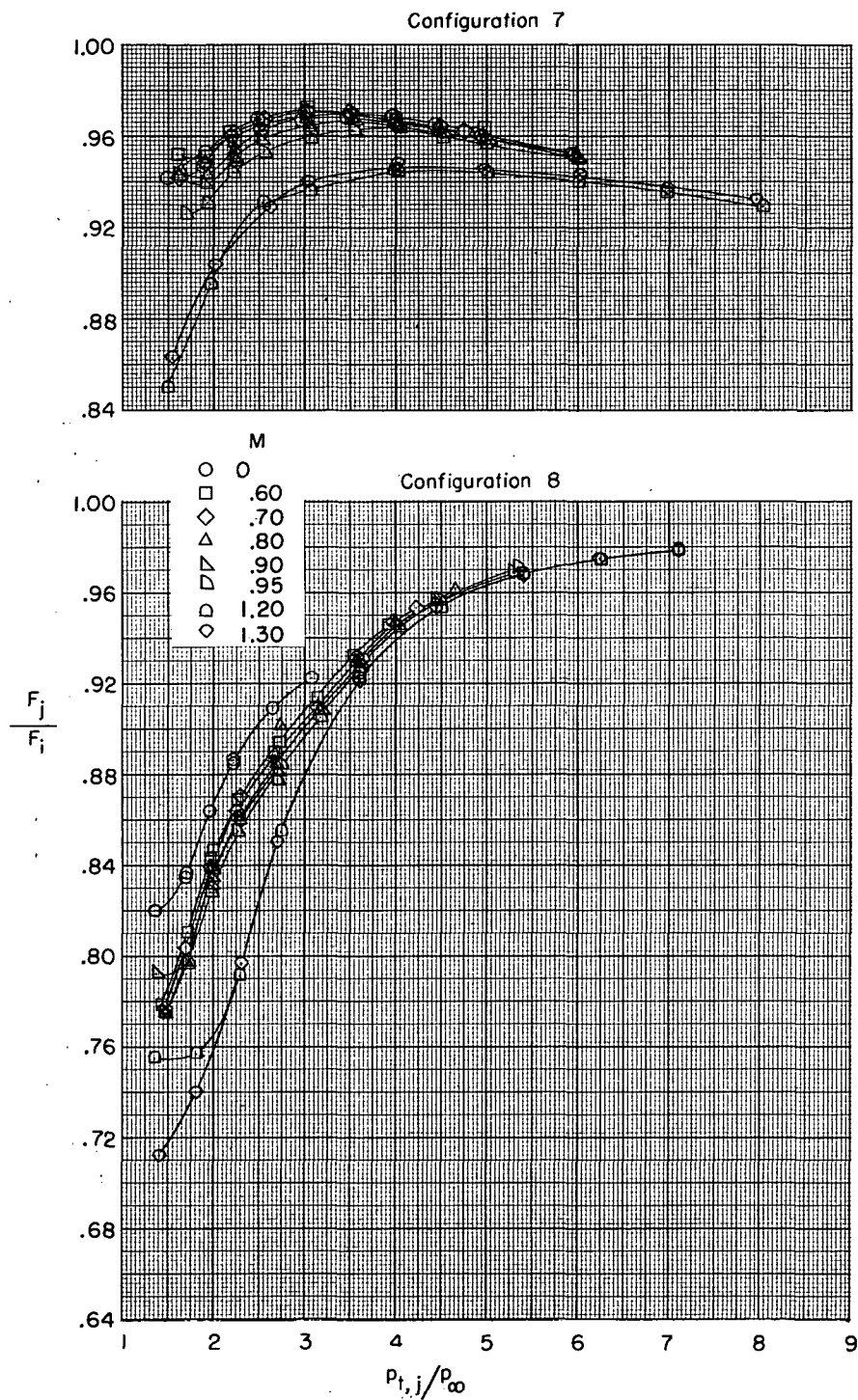
Configuration 8

(d) Configurations 7 and 8.

Figure 27.- Concluded.
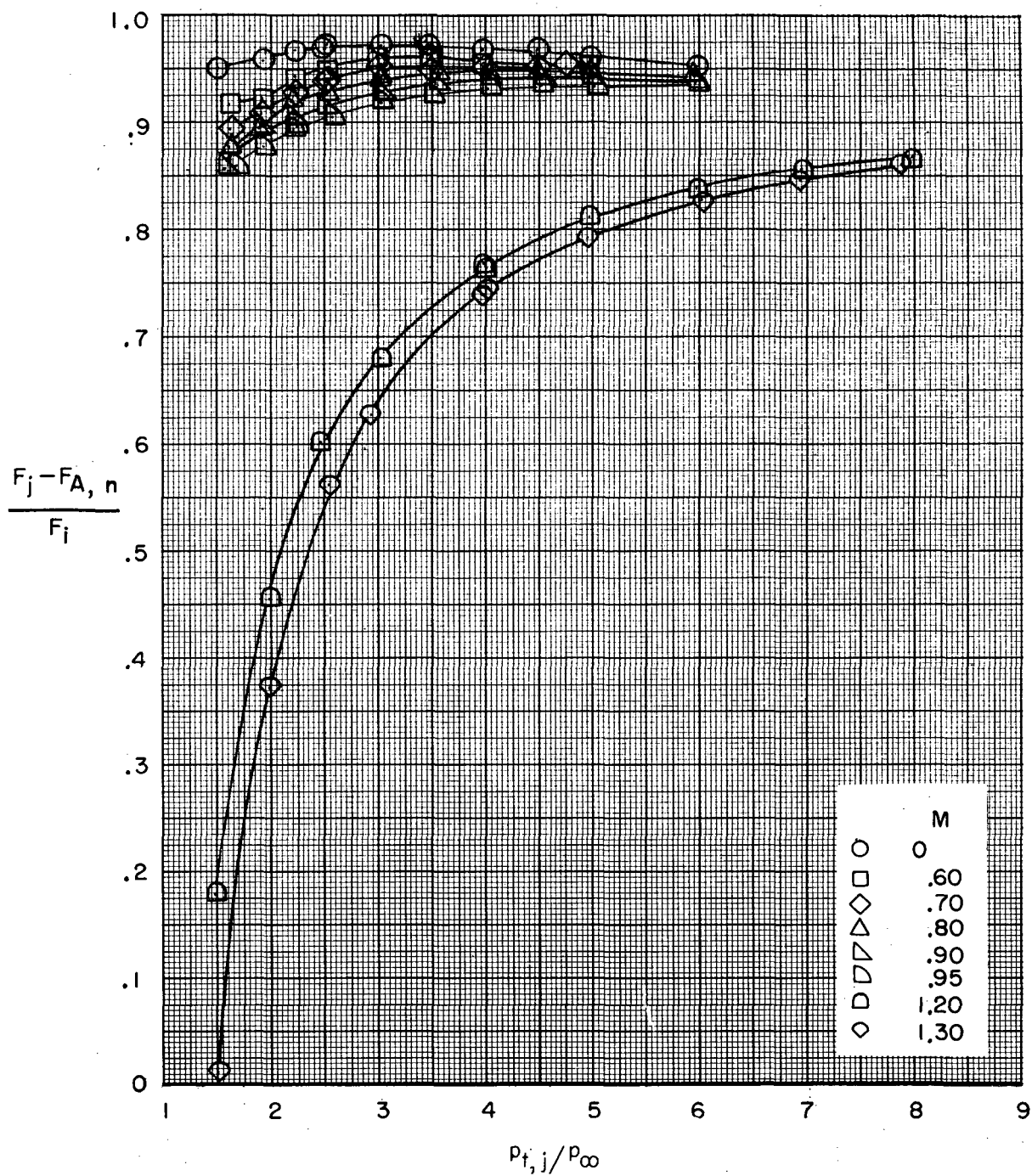
(a) Configuration 1.

Figure 28.- Variation of gross-thrust minus nozzle-drag ratio with jet-total-pressure ratio for the various configurations.
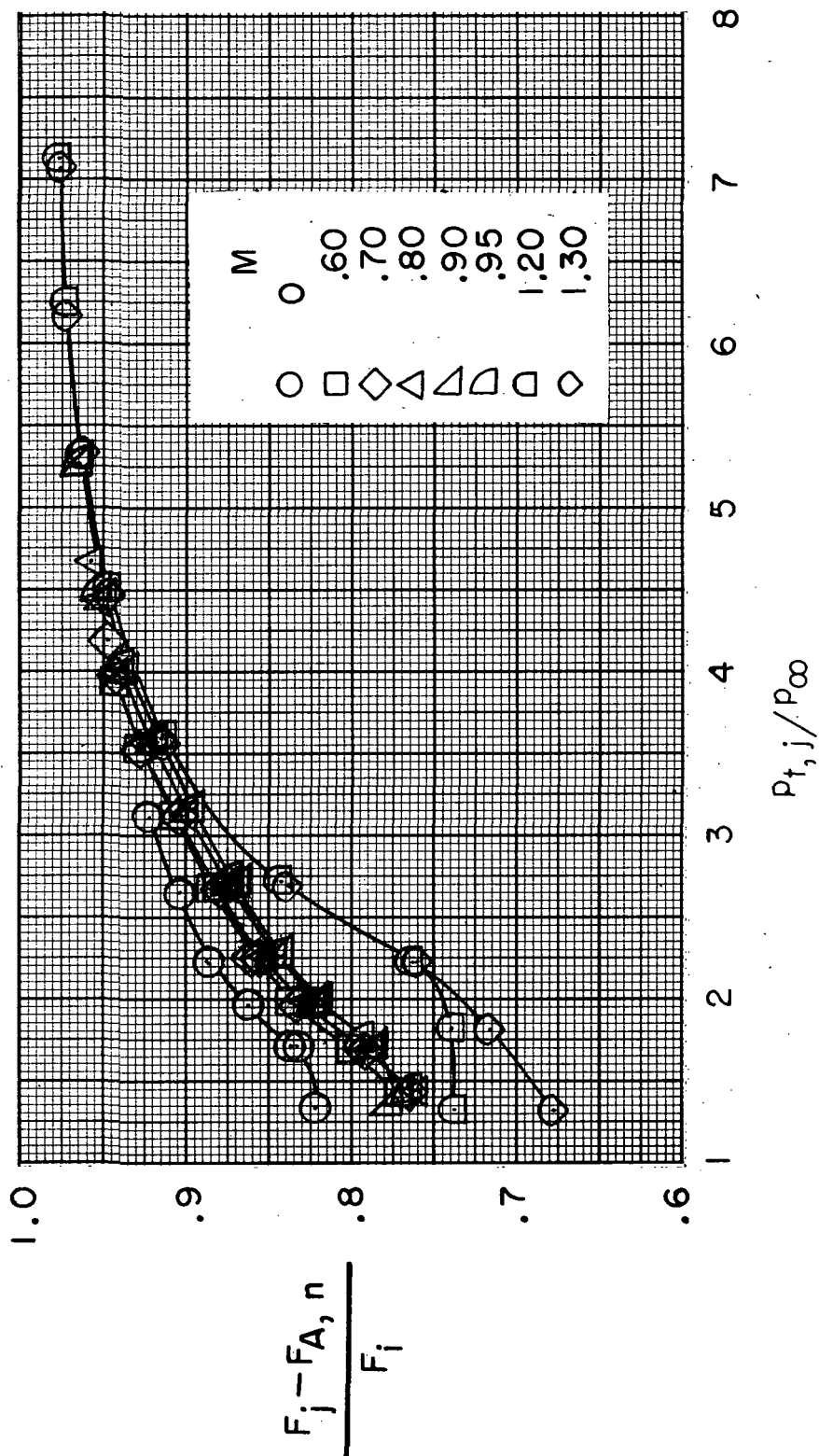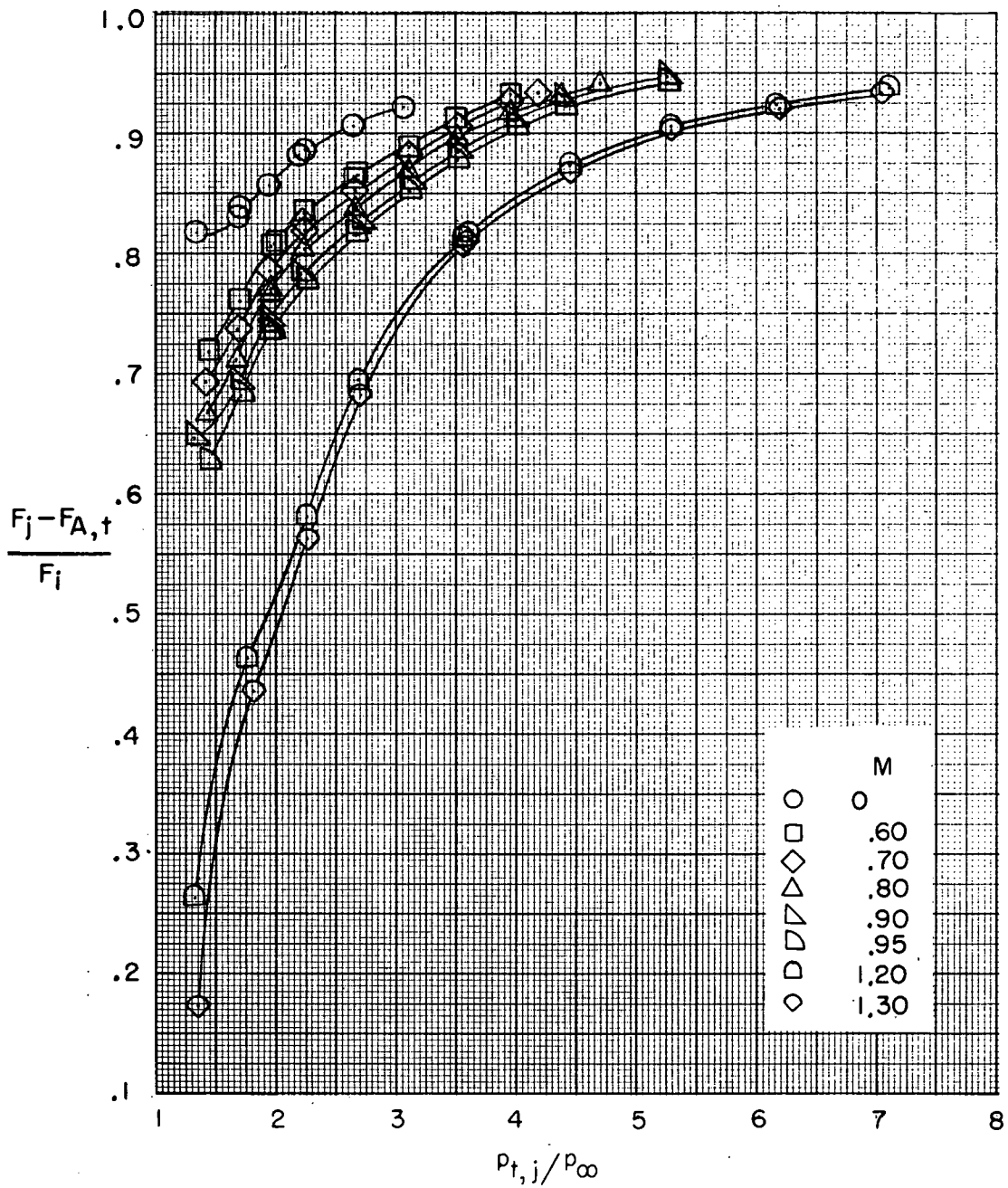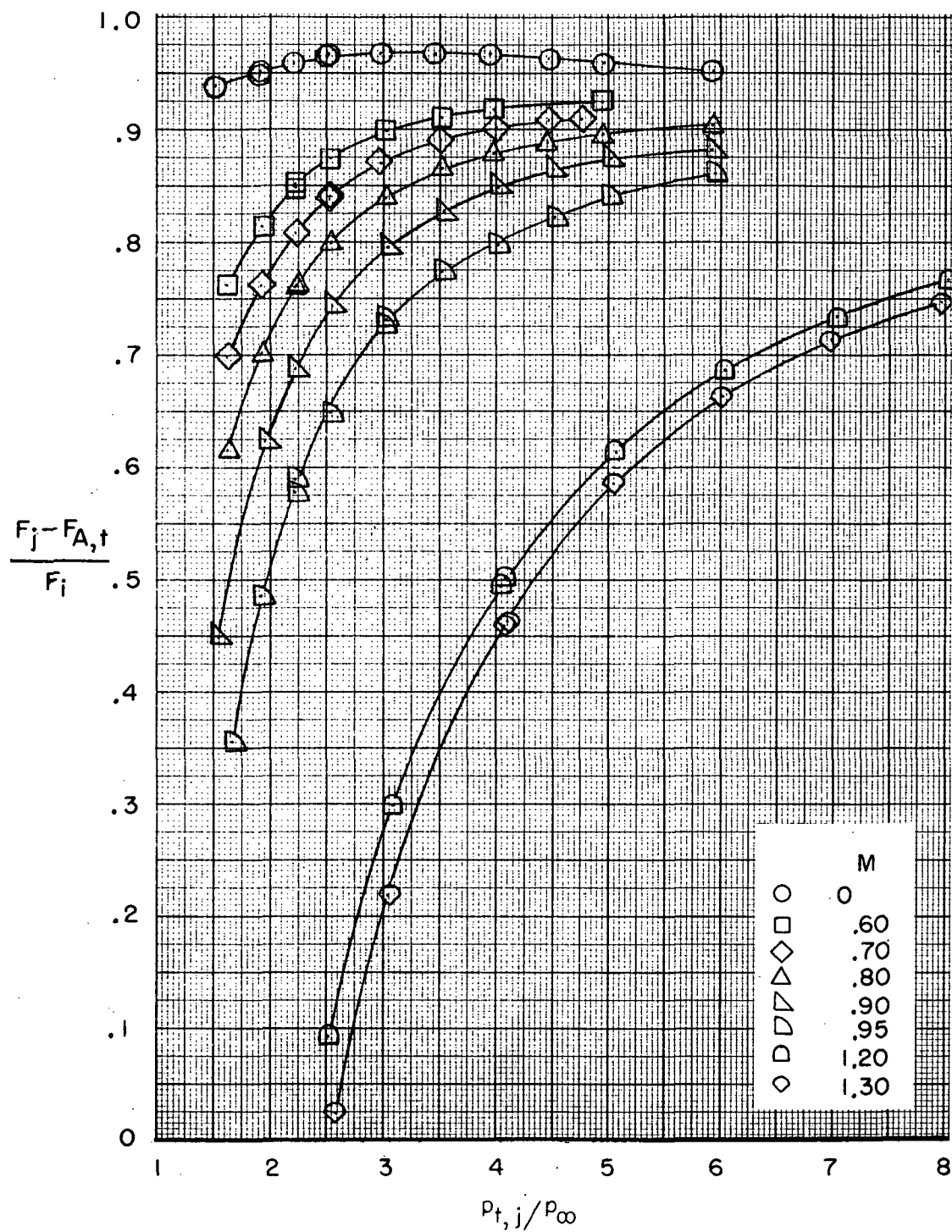
(b) Configuration 2.

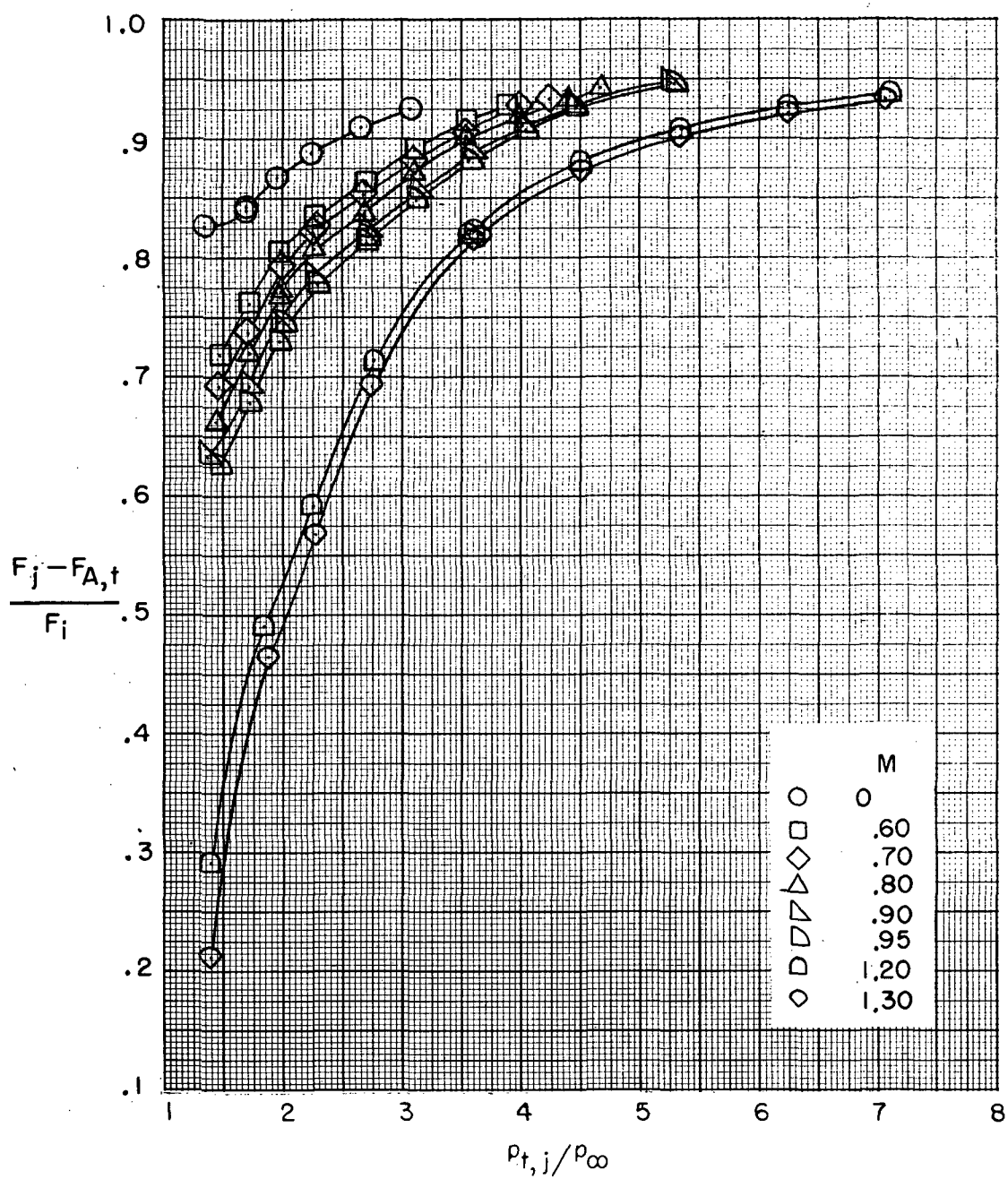Figure 28. – Continued.
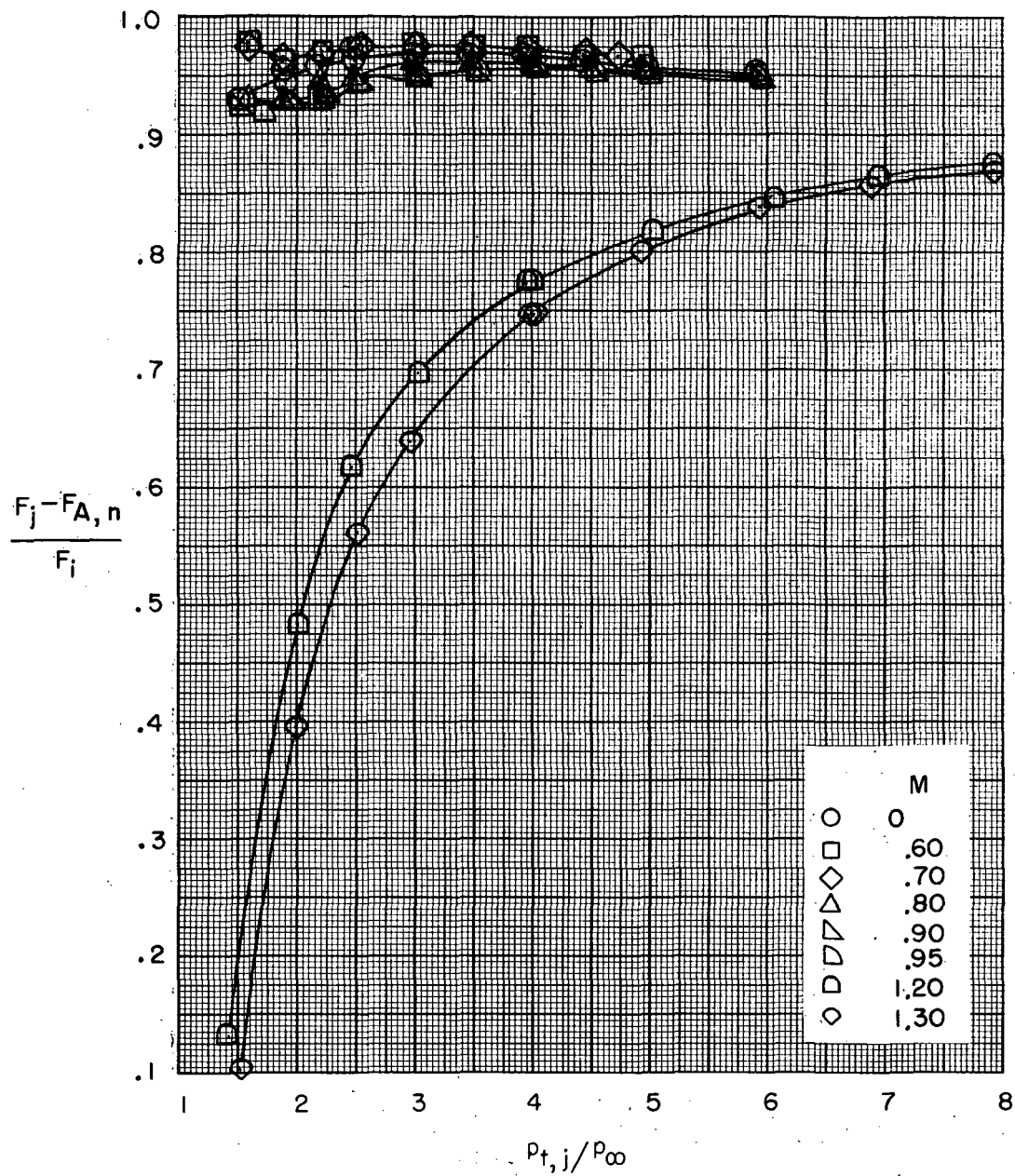
(c) Configuration 3.

Figure 28.- Continued.
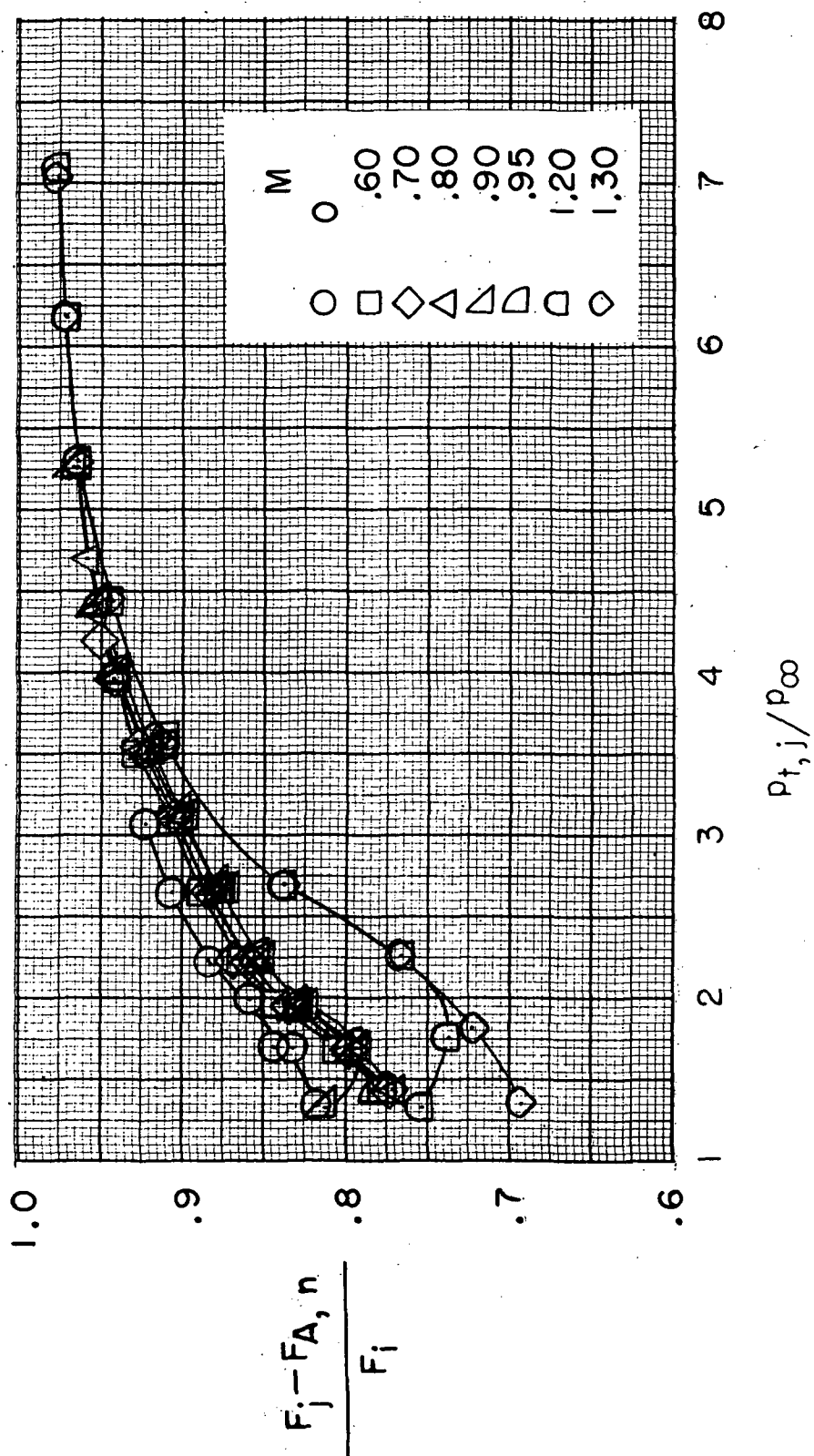
(d) Configuration 4.
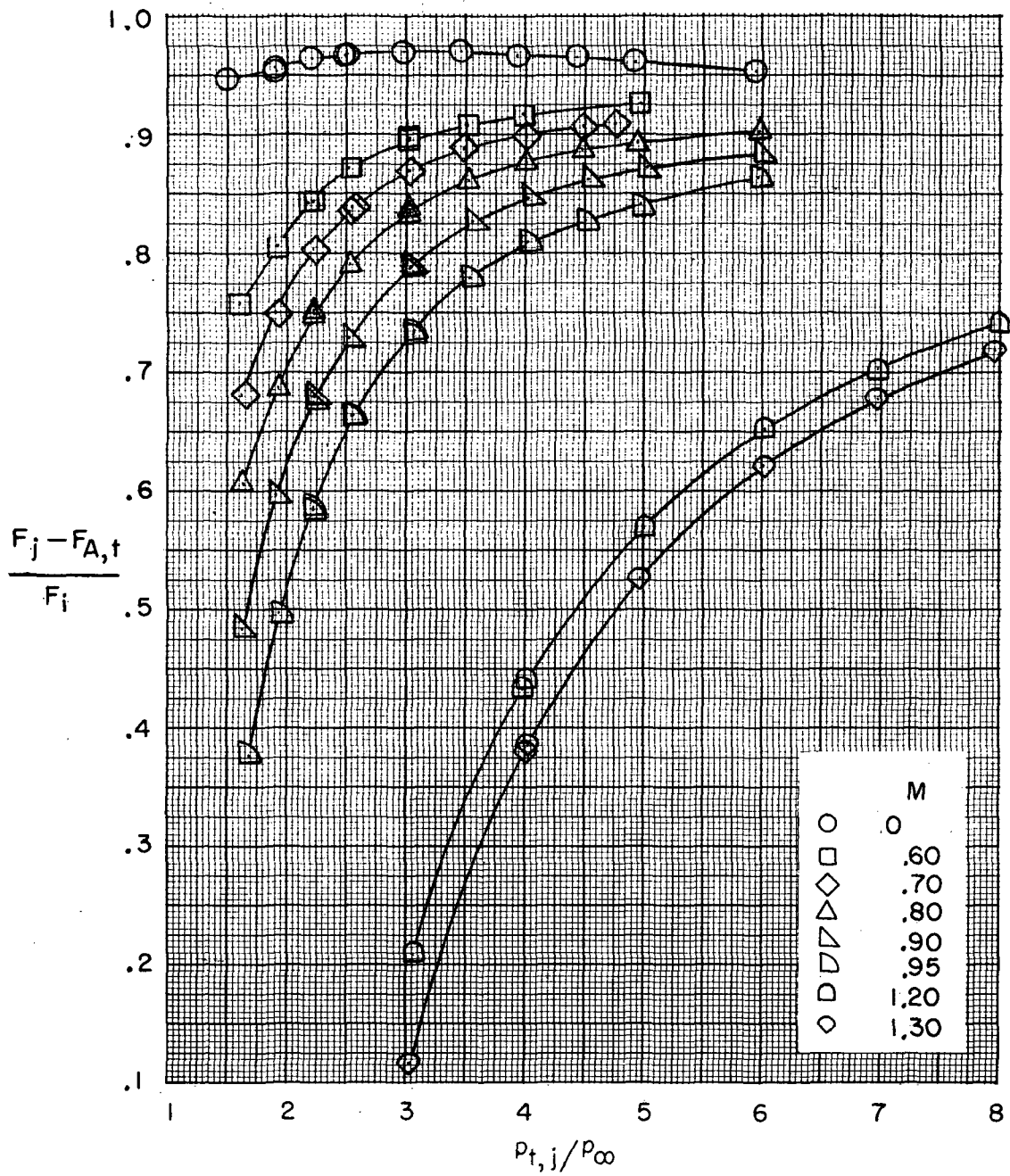
Figure 28. - Continued.
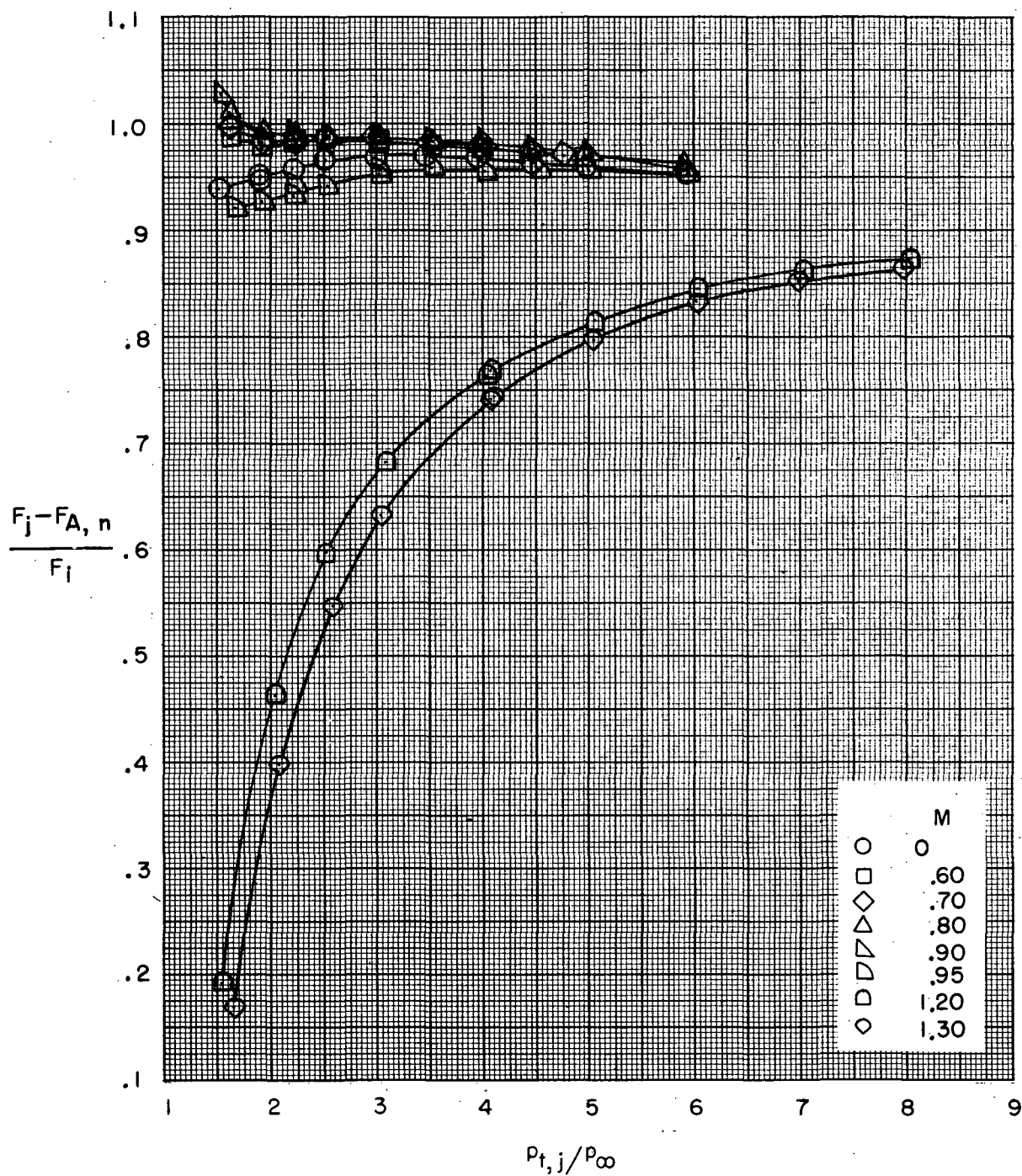
(e) Configuration 5.

Figure 28.- Continued.
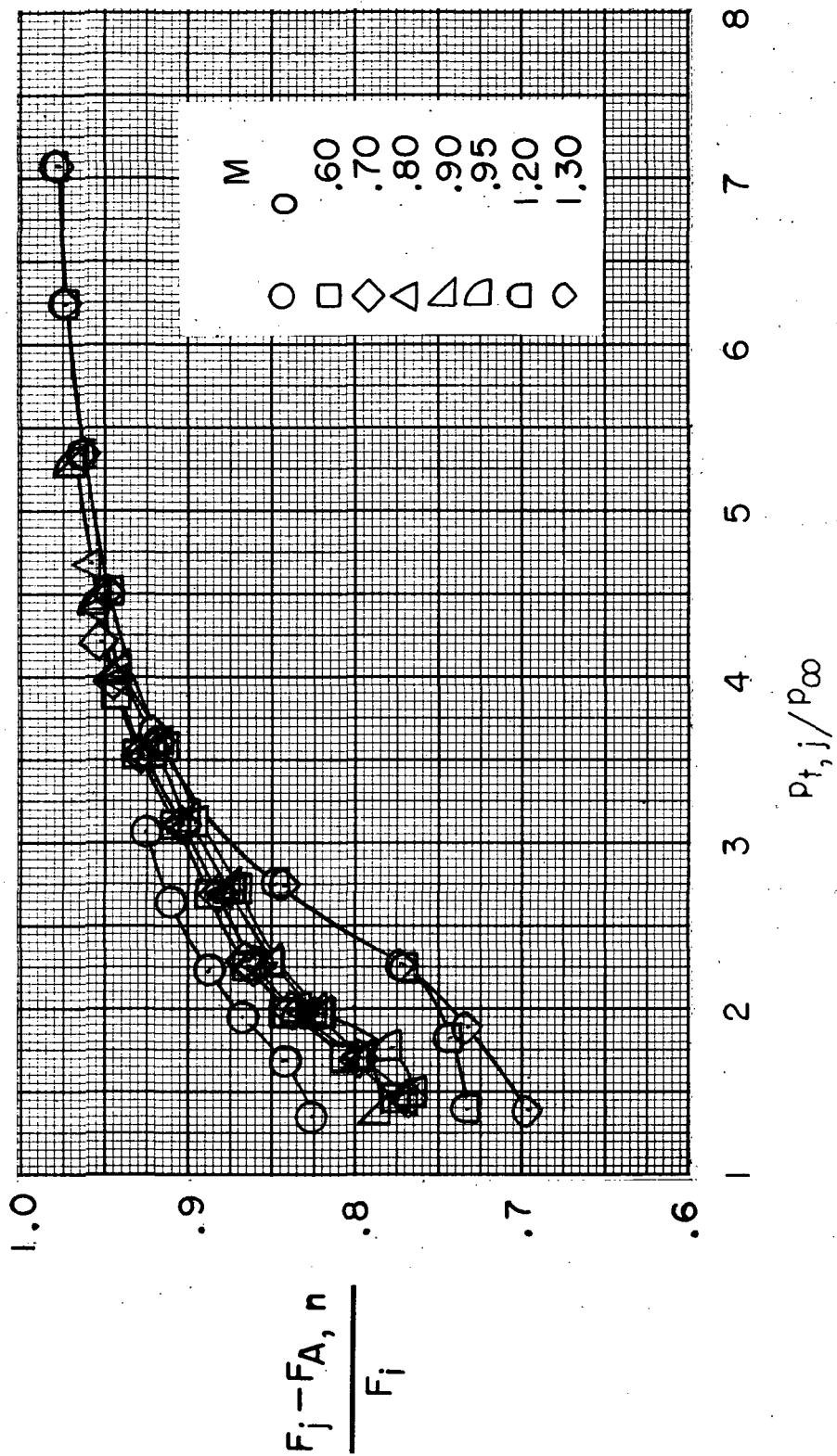
(f) Configuration 6.

Figure 28. – Continued.
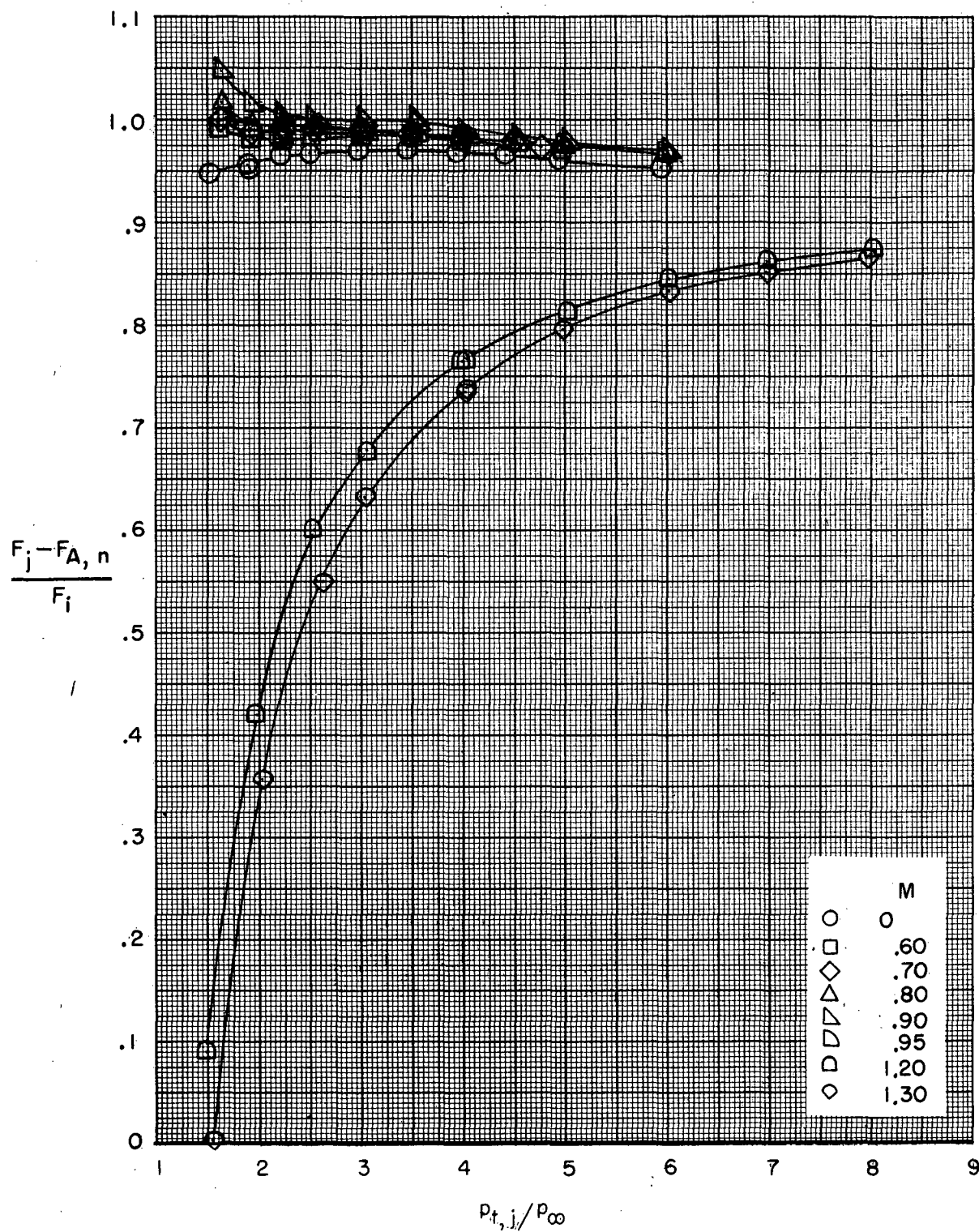
(g) Configuration 7.

Figure 28. - Continued.
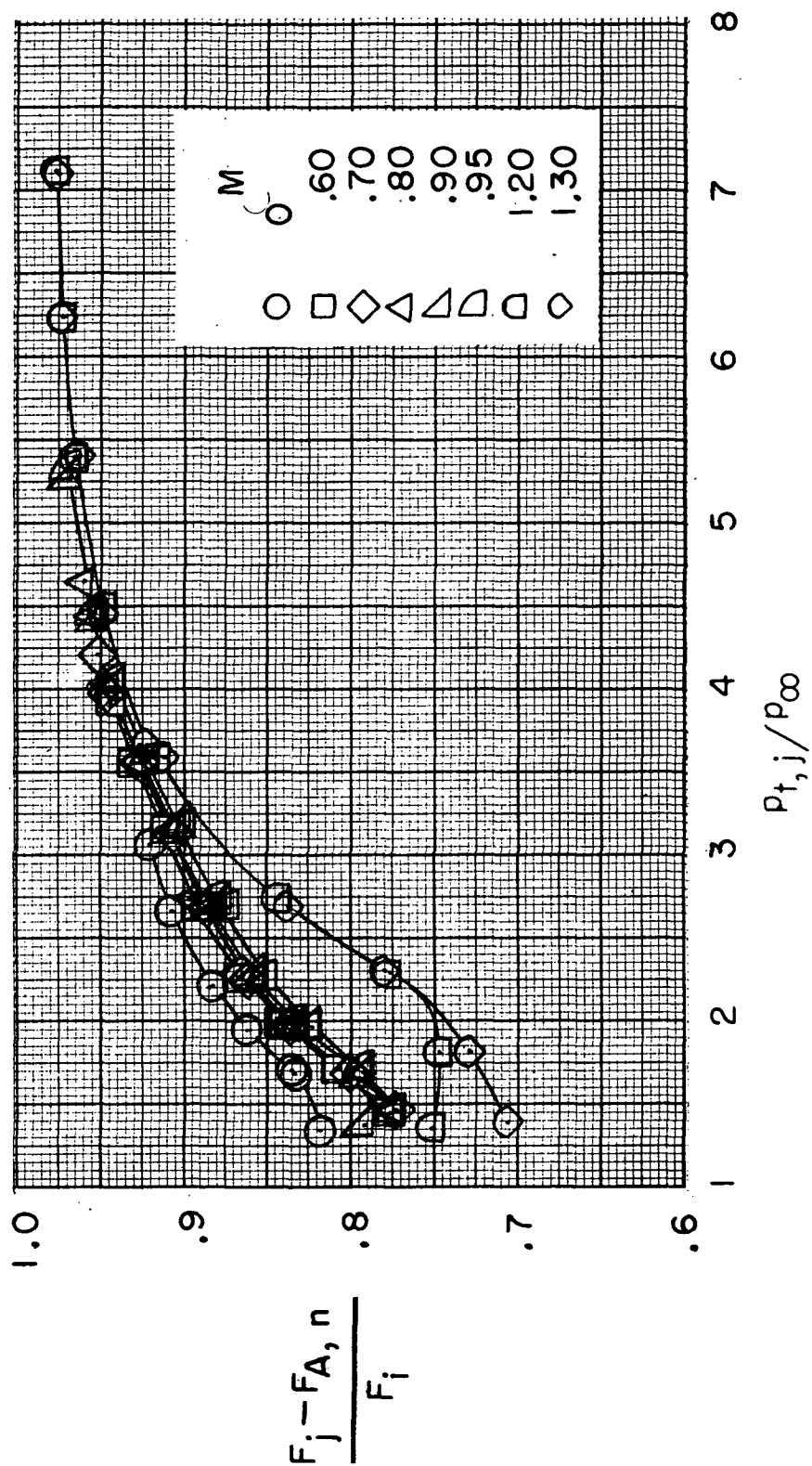
(h) Configuration 8.

Figure 28. - Concluded.
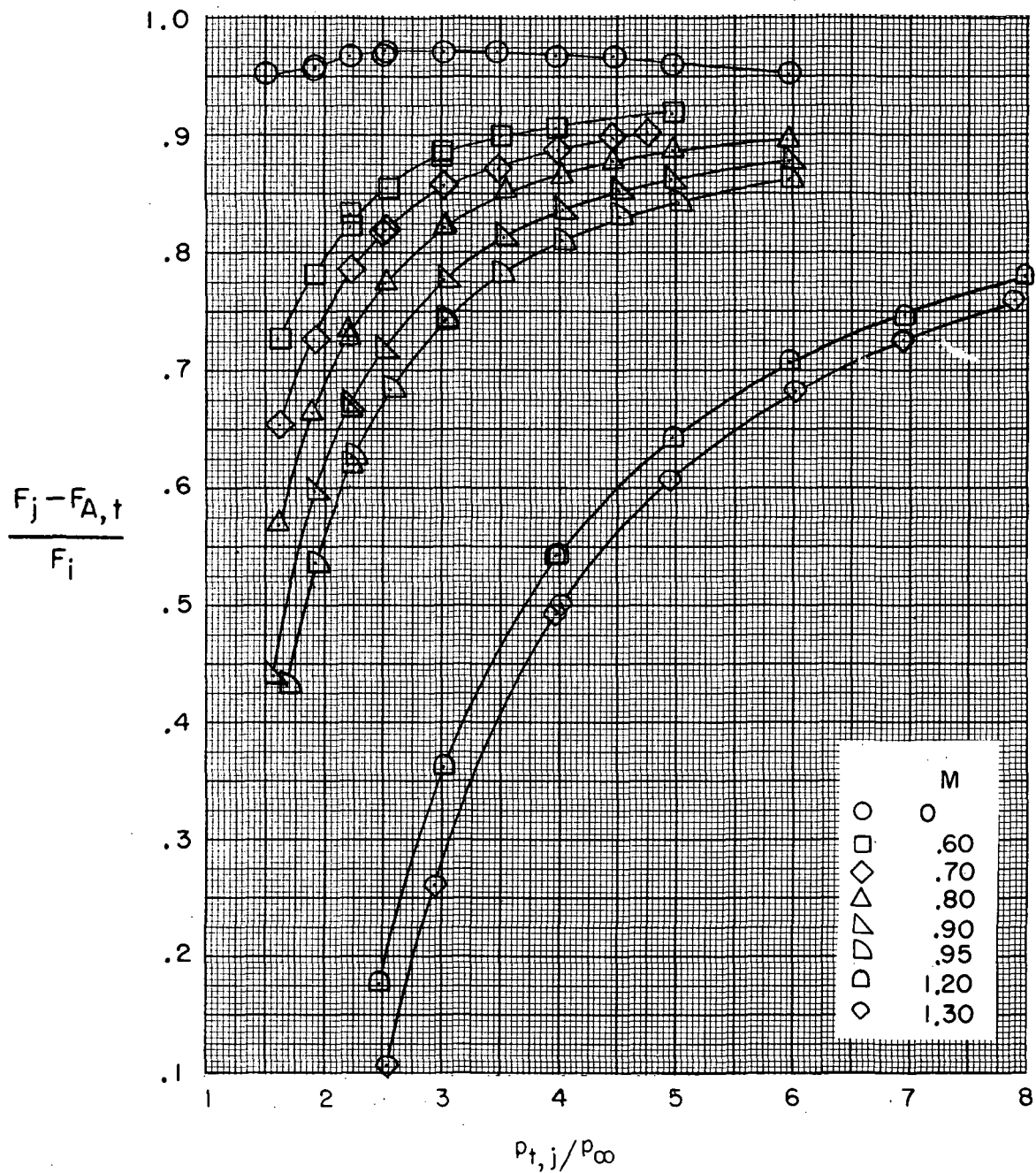
(a) Configuration 1.

Figure 29.- Variation of gross-thrust minus total-drag ratio with jet-total-pressure ratio for the various configurations.
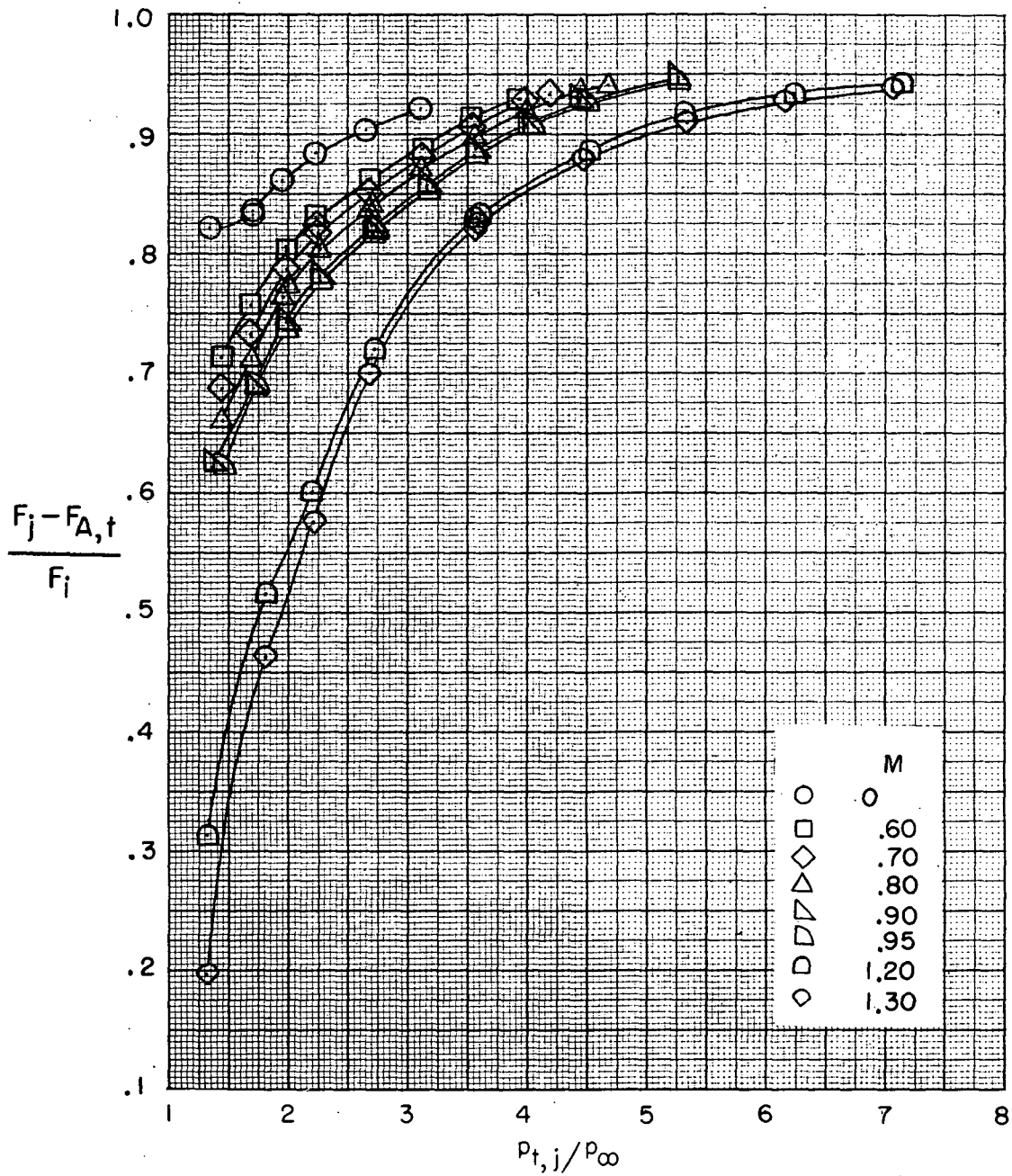
(b) Configuration 2.

Figure 29.- Continued.

(c) Configuration 3.

Figure 29. - Continued.

(d) Configuration 4.

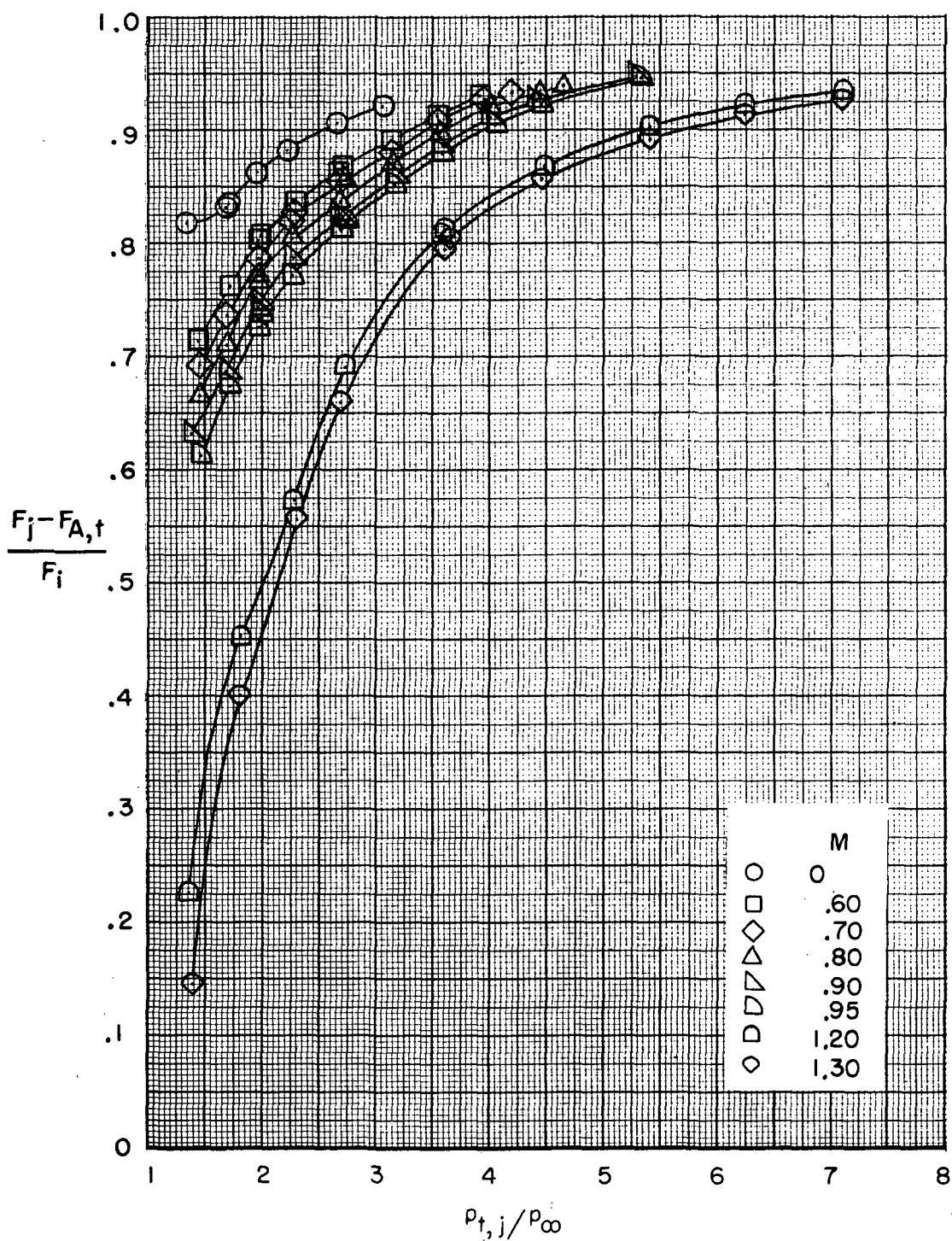Figure 29.- Continued.

(e) Configuration 5.

Figure 29.- Continued.

(f) Configuration 6.

Figure 29.- Continued.

(g) Configuration 7.

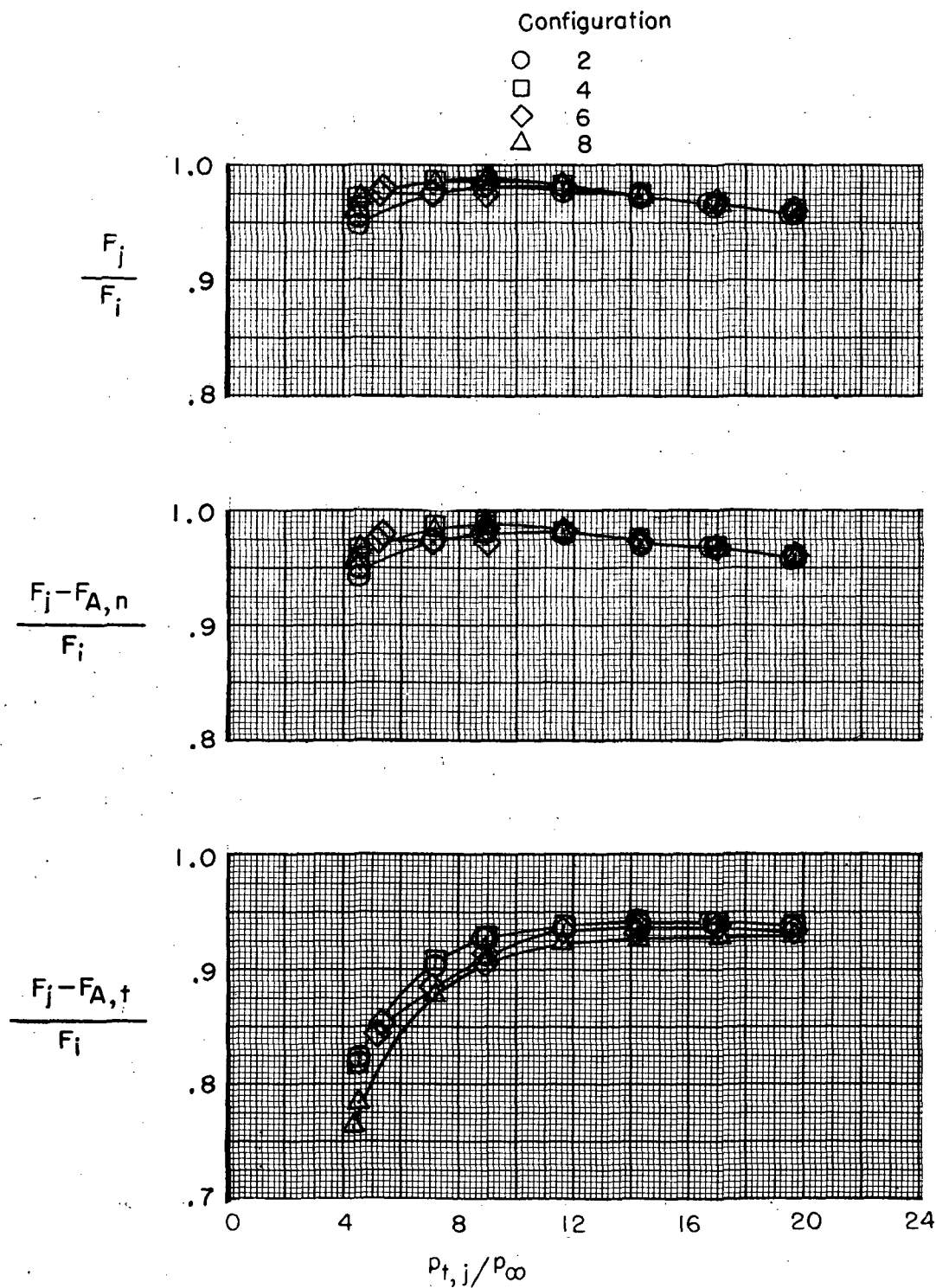Figure 29.- Continued.

(h) Configuration 8.

Figure 29. - Concluded.

Figure 30.- Variation of performance of the afterburning-nozzle configurations with jet-total-pressure ratio at M = 2.20.
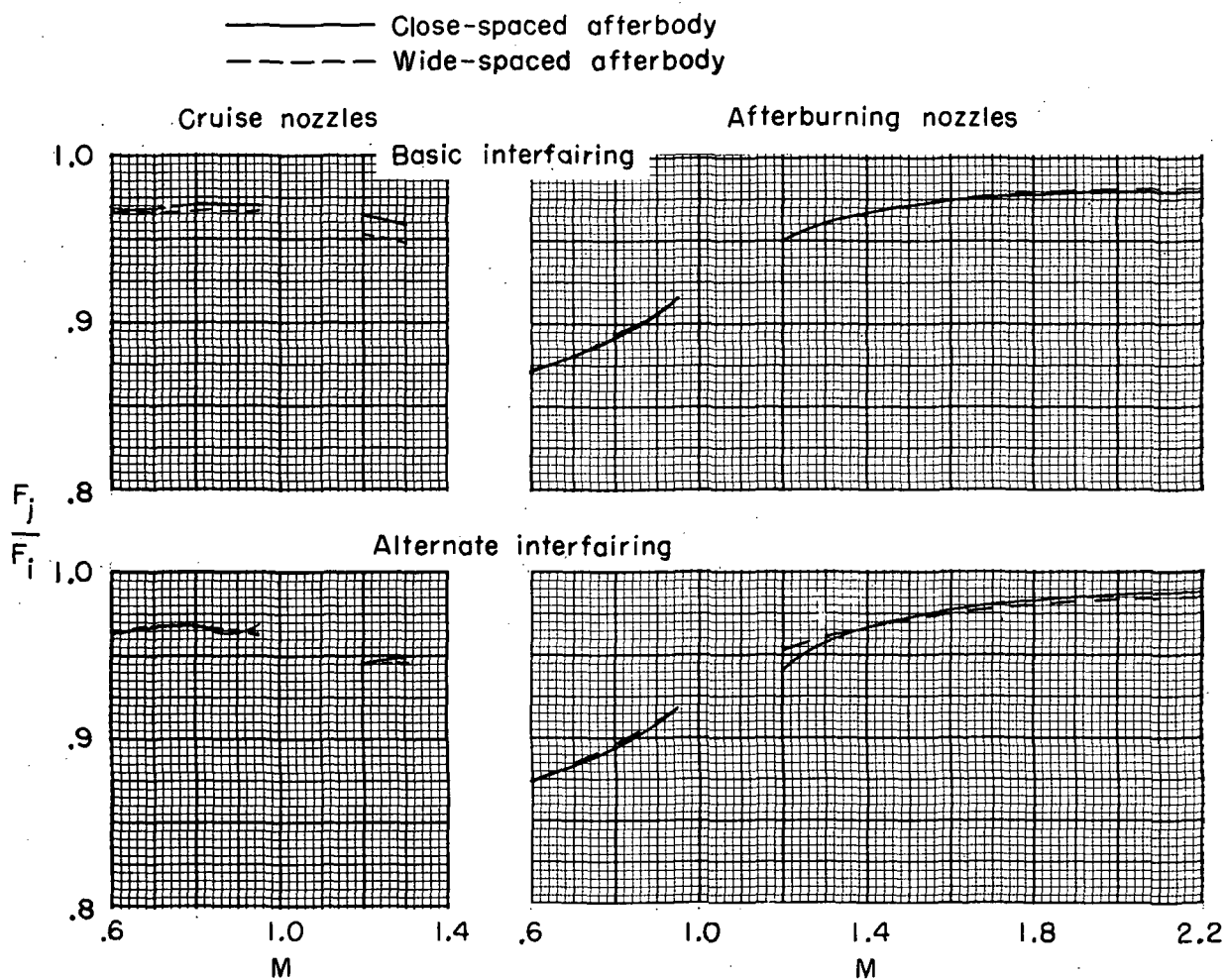
Figure 31.- Variation of gross-thrust ratio with Mach number for the various
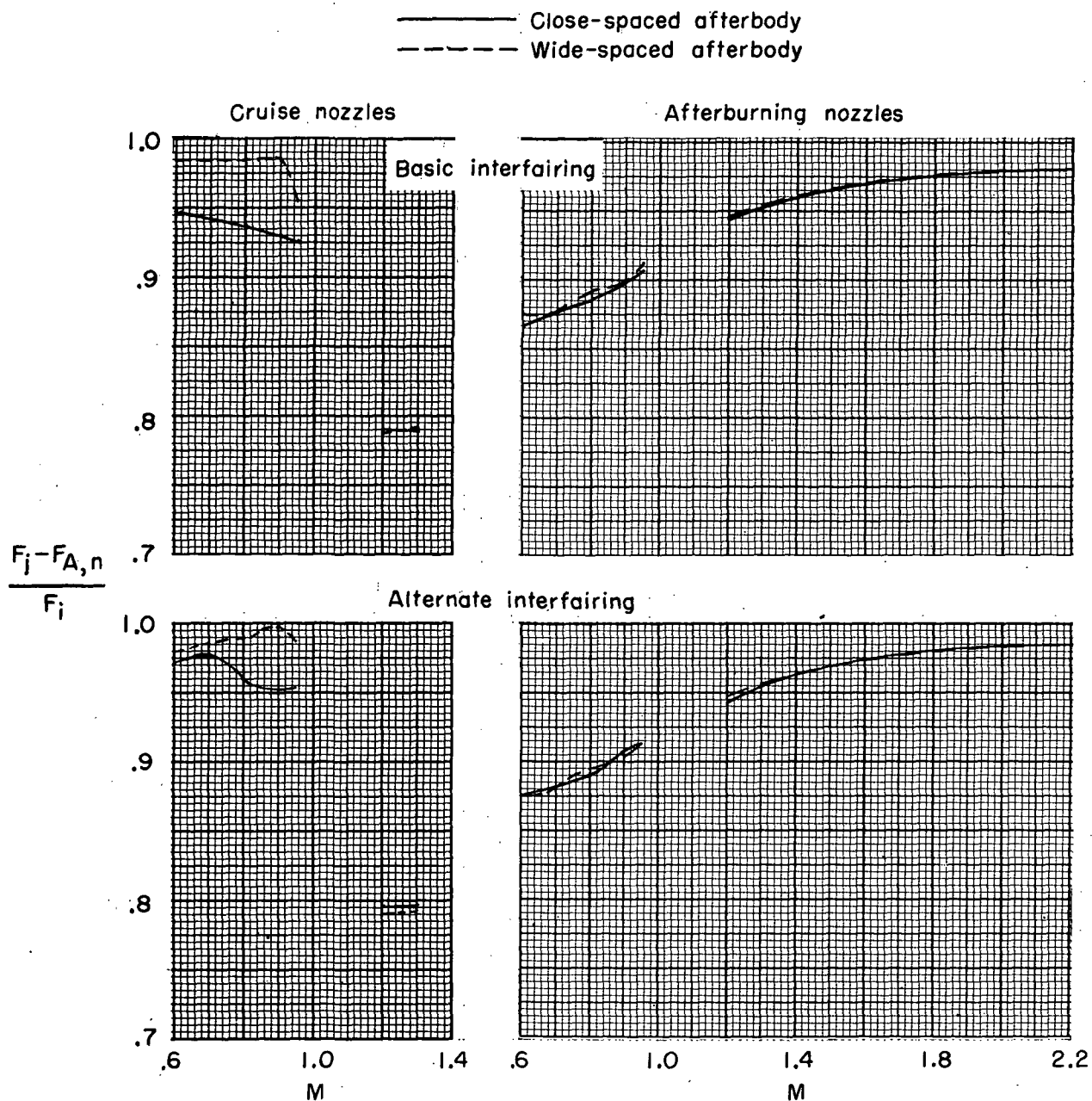configurations at scheduled jet-total-pressure ratios.

Figure 32.- Variation of gross-thrust minus nozzle-drag ratio with Mach number for the various configurations at scheduled jet-total-pressure ratios.
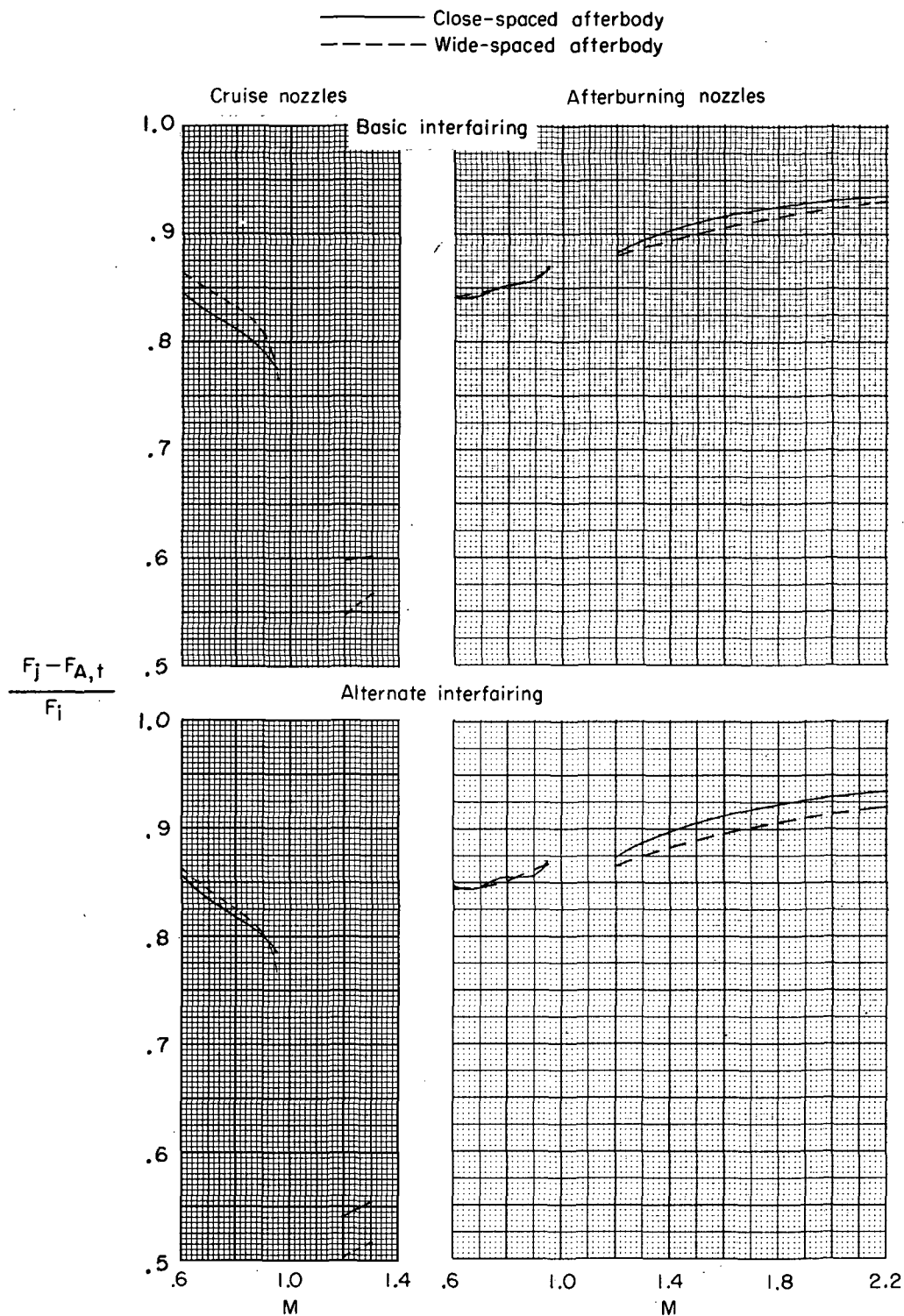
Figure 33.- Variation of gross-thrust minus total-drag ratio with Mach number for the various configurations at scheduled jet-total-pressure ratios.

*"The aeronautical and space activities of the United States shall be
conducted so as to contribute . . . to the expansion of human knowl-
edge of phenomena in the atmosphere and space. The Administration
shall provide for the widest practicable and appropriate dissemination
of information concerning its activities and the results thereof."*
—NATIONAL AERONAUTICS AND SPACE ACT OF 1958

NASA SCIENTIFIC AND TECHNICAL PUBLICATIONS

TECHNICAL REPORTS: Scientific and
technical information considered important,
complete, and a lasting contribution to existing
knowledge.

TECHNICAL NOTES: Information less broad
in scope but nevertheless of importance as a
contribution to existing knowledge.

TECHNICAL MEMORANDUMS:
Information receiving limited distribution
because of preliminary data, security classifica-
tion, or other reasons. Also includes conference
proceedings with either limited or unlimited
distribution.

CONTRACTOR REPORTS: Scientific and
technical information generated under a NASA
contract or grant and considered an important
contribution to existing knowledge.

TECHNICAL TRANSLATIONS: Information
published in a foreign language considered
to merit NASA distribution in English.

SPECIAL PUBLICATIONS: Information
derived from or of value to NASA activities.
Publications include final reports of major
projects, monographs, data compilations,
handbooks, sourcebooks, and special
bibliographies.

TECHNOLOGY UTILIZATION
PUBLICATIONS: Information on technology
used by NASA that may be of particular
interest in commercial and other non-aerospace
applications. Publications include Tech Briefs,
Technology Utilization Reports and
Technology Surveys.

Details on the availability of these publications may be obtained from:

SCIENTIFIC AND TECHNICAL INFORMATION OFFICE

NATIONAL AERONAUTICS AND SPACE ADMINISTRATION
Washington, D.C. 20546